



UPPSALA
UNIVERSITET

*Digital Comprehensive Summaries of Uppsala Dissertations
from the Faculty of Science and Technology 1461*

Theoretical methods for the electronic structure and magnetism of strongly correlated materials

INKA L. M. LOCHT



ACTA
UNIVERSITATIS
UPSALIENSIS
UPPSALA
2017

ISSN 1651-6214
ISBN 978-91-554-9770-5
urn:nbn:se:uu:diva-308699

Dissertation presented at Uppsala University to be publicly examined in Ång/10132, Högssalen, Ångströmlaboratoriet, Lägerhyddsvägen 1, Uppsala, Friday, 3 February 2017 at 09:15 for the degree of Doctor of Philosophy. The examination will be conducted in English. Faculty examiner: Prof. Dr. Silke Biermann (CPHT, Ecole Polytechnique).

Abstract

Locht, I. L. M. 2017. Theoretical methods for the electronic structure and magnetism of strongly correlated materials. *Digital Comprehensive Summaries of Uppsala Dissertations from the Faculty of Science and Technology* 1461. 109 pp. Uppsala: Acta Universitatis Upsaliensis. ISBN 978-91-554-9770-5.

In this work we study the interesting physics of the rare earths, and the microscopic state after ultrafast magnetization dynamics in iron. Moreover, this work covers the development, examination and application of several methods used in solid state physics. The first and the last part are related to strongly correlated electrons. The second part is related to the field of ultrafast magnetization dynamics.

In the first part we apply density functional theory plus dynamical mean field theory within the Hubbard I approximation to describe the interesting physics of the rare-earth metals. These elements are characterized by the localized nature of the *4f* electrons and the itinerant character of the other valence electrons. We calculate a wide range of properties of the rare-earth metals and find a good correspondence with experimental data. We argue that this theory can be the basis of future investigations addressing rare-earth based materials in general.

In the second part of this thesis we develop a model, based on statistical arguments, to predict the microscopic state after ultrafast magnetization dynamics in iron. We predict that the microscopic state after ultrafast demagnetization is qualitatively different from the state after ultrafast increase of magnetization. This prediction is supported by previously published spectra obtained in magneto-optical experiments. Our model makes it possible to compare the measured data to results that are calculated from microscopic properties. We also investigate the relation between the magnetic asymmetry and the magnetization.

In the last part of this work we examine several methods of analytic continuation that are used in many-body physics to obtain physical quantities on real energies from either imaginary time or Matsubara frequency data. In particular, we improve the Padé approximant method of analytic continuation. We compare the reliability and performance of this and other methods for both one and two-particle Green's functions. We also investigate the advantages of implementing a method of analytic continuation based on stochastic sampling on a graphics processing unit (GPU).

Keywords: dynamical mean field theory (DMFT), Hubbard I approximation, strongly correlated systems, rare earths, lanthanides, photoemission spectra, ultrafast magnetization dynamics, analytic continuation, Padé approximant method, two-particle Green's functions, linear muffin tin orbitals (LMTO), density functional theory (DFT), cerium, stacking fault energy.

Inka L. M. Loch, Department of Physics and Astronomy, Materials Theory, Box 516, Uppsala University, SE-751 20 Uppsala, Sweden.

© Inka L. M. Loch 2017

ISSN 1651-6214

ISBN 978-91-554-9770-5

urn:nbn:se:uu:diva-308699 (<http://urn.kb.se/resolve?urn=urn:nbn:se:uu:diva-308699>)

List of papers

This thesis is based on the following papers, which are referred to in the text by their Roman numerals.

- I **Standard model of the rare-earths, analyzed from the Hubbard I approximation.**
I. L. M. Locht, Y. O. Kvashnin, D. C. M. Rodrigues, M. Pereiro, A. Bergman, L. Bergqvist, A. I. Lichtenstein, M. I. Katsnelson, A. Delin, A. B. Klautau, B. Johansson, I. Di Marco and O. Eriksson,
PHYSICAL REVIEW B **94**, 085137 (2016)

- II **Stacking fault energetics of α - and γ -cerium investigated with ab initio calculations.**
A. Östlin, I. Di Marco, I. L. M. Locht, J. C. Lashley and L. Vitos,
PHYSICAL REVIEW B **93**, 094103 (2016)

- III **Ultrafast magnetization dynamics: Microscopic electronic configurations and ultrafast spectroscopy.**
I. L. M. Locht, I. Di Marco, S. Garnerone, A. Delin and M. Battiato,
PHYSICAL REVIEW B **92**, 064403 (2015)

- IV **Draft of: Magnetic asymmetry around the $3p$ absorption edge in Fe and Ni**
I. L. M. Locht, S. Jana, Y. O. Kvashnin, R. Knut, I. Di Marco, R. Chimata, R. S. Malik, M. Ahlberg, M. Battiato, J. Ruzs, R. Stefanuik, J. Söderström, T. J. Silva, J. Åkerman, H. T. Nembach, J. M. Shaw, O. Karis, O. Eriksson,
In preparation

- V **Analytic continuation by averaging Padé approximants.**
J. Schött, I. L. M. Locht, E. Lundin, O. Grånäs, O. Eriksson and I. Di Marco,
PHYSICAL REVIEW B **93**, 075104 (2016)

- VI **A comparison between methods of analytical continuation for bosonic functions.**
J. Schött, E. G. C. P. van Loon, I. L. M. Locht, M. I. Katsnelson and I. Di Marco,
accepted in PRB

VII A GPU code for analytic continuation through a sampling method.
J. Nordström, J. Schött, I. L. M. Loch, and I. Di Marco, accepted in
SoftwareX

Reprints were made with permission from the publishers.

Publications not included in this thesis:

Reproducibility in density functional theory calculations of solids.
K. Lejaeghere *et al.*, Science **351**, 6280 (2016)

Comments on my participation

The main project during my PhD was to apply the Hubbard I approximation to describe the electronic structure of the rare earths. I did all calculations on the cohesive properties, structural stabilities, ground-state magnetic moments and the valence-band spectra. The exchange parameters were calculated by Yaroslav Kvashnin and the resulting ordering temperatures and magnon spectra were calculated by Debora Rodrigues and Manuel Pereiro. I analyzed most data and contributed to obtain a consistent physical picture. The research was planned by Igor Di Marco and Olle Eriksson and also by myself in a later stage. Paper I is mainly written by me. For Paper II, I performed all Hubbard I calculations, and participated in discussions.

The development of the model presented in Paper III to predict the microscopic state directly after ultrafast magnetization dynamics was a joint effort by me, Igor Di Marco and Marco Battiato, with help of Silvano Garnerone and Anna Delin. For both Paper III and IV I participated in planning the research, developing the theory, discussing the results and writing the paper. All DFT calculations in Papers III and IV are done by me.

The improvement of the Padé approximant method was mainly planned by Igor Di Marco and Johan Schött, who developed the routines and performed the calculations. Elin Lundin and I started this work as part of her bachelor student project. When Johan Schött joined the group he took over the project. I participated in analyzing the results, planning the next steps and also in writing the paper. For Paper VI, I initiated the collaboration with Erik van Loon and Mikhail Katsnelson. I participated in planning the research, discussing, analyzing the results, and writing the article. The calculations were done by Johan Schött. The GPU implementation for the analytic continuation was done by Johan Nordström as part of an independent bachelor work for technical physics. I got involved in this as project mentor of Johan Nordström. I participated in analyzing the results, writing the paper and preparing the code for publication.

Finally, in all works, I contributed to discuss the criticism raised by the referees and to write appropriate replies.

Contents

1	Introduction	7
2	Methods	10
2.1	Solid state Hamiltonian	11
2.2	Density Functional Theory	12
2.2.1	Hohenberg-Kohn theorems	12
2.2.2	Kohn-Sham <i>ansatz</i>	13
2.2.3	Approximations to the energy functional	16
2.2.4	LMTO and LAPW bases	17
2.3	Hubbard I approximation	19
2.3.1	Effective Hubbard model	21
2.3.2	Effective Single impurity Anderson model	22
2.3.3	Computational scheme	26
2.3.4	Hubbard U and Hund's J	28
2.3.5	Double counting	31
3	Lanthanides	33
3.1	Outer electronic configuration	34
3.2	Bonding properties	34
3.3	Structural stabilities	36
3.4	Magnetism	37
3.4.1	Coupling of spin and orbital moments	37
3.4.2	Moments arising from the spin, orbital and total angular momenta	38
3.4.3	Magnetic moments in a magnetic field	40
3.5	Spectral properties	43
3.5.1	Spectroscopy	43
3.5.2	Experiment and theory	44
3.5.3	Multiplet structure	46
3.6	Summary of Papers I and II	46
3.7	Outlook	49
4	Microscopic configuration after ultrafast magnetization dynamics	51
4.1	Summary of Paper III: Microscopic configuration after ultrafast magnetization dynamics	53
4.2	Magneto-optics	56
4.2.1	Experiments	57

4.2.2	Dielectric tensor	58
4.2.3	Relation asymmetry and dielectric tensor	59
4.3	Is the magnetic asymmetry proportional to the sample magnetization?	60
4.3.1	Before the laser pulse: equilibrium situation	60
4.3.2	After the laser pulse: recovering the equilibrium magnetization	62
4.4	Outlook	66
5	Analytic continuation	68
5.1	Spectral functions	68
5.2	Methods of analytic continuation	70
5.2.1	Padé approximant method	72
5.2.2	Stochastic Sampling	76
5.2.3	Least square solutions and regularizations	78
5.3	Remarks on performance	82
5.4	Summary of Papers V, VI and VII	82
5.5	Outlook	86
	Popular scientific summary	88
	Populärvetenskaplig sammanfattning	91
	Populair wetenschappelijke samenvatting	94
	Acknowledgements	97
	Appendices	99
A	Finding the multiplets in Nd	100
	References	103

1. Introduction

ABOUT one year ago, my cousin asked me: “What do you actually do?” An innocent question of a kid. I faced myself the challenge of explaining to a 9 year old about computational material theory, about the ins and outs of the Hubbard I approximation and about the concept of analytic continuation. The discussion following this question involved lego bricks representing the different atoms in the periodic table and how one can build, with only “carbon lego bricks”, shiny diamonds as well as the soft black graphite stick in your pencil. It involved dancing couples representing the spin up and spin down pairs in the same orbital and how one could predict their behavior and their influence on the other dancers. In this thesis I aim to explain my work on a more fundamental level. I wish you great fun reading it and I hope you will enjoy it as much as I did doing the research which underlies this thesis.

Materials have always been important for mankind. Also nowadays the development of many applications is restricted by the properties, the scarcity and the costs of the materials involved. Imagine a feature-full smartphone with a battery that needs to be charged only once a month, although you use its full capabilities. Imagine a panel of highly efficient, payable solar-cells on your roof. Or imagine much faster and more energy efficient data storage and sensing devices. These are only a few examples for which we need new materials with more and more desired properties. To find these materials the joint effort of experimentalists, theoreticians and engineers in the field of material science is required. My modest contribution to the field is of theoretical nature. I think that the theoretical research in material science can be decomposed in two categories. On the one hand, the more applied category, in which the research focusses on the direct search for materials with a set of desired properties. On the other hand, the more fundamental category of model and method development. My thesis falls in the second category: we examine a method to describe the electronic structure of the rare earths, we improve and extensively test different methods of analytic continuation, and we also develop a model to predict the microscopic state after ultrafast magnetization dynamics. With this we hope to contribute to the improvement of the state-of-the-art methods used in material science.

After this introduction, Chapter 2 is a method chapter, that briefly introduces density functional theory and its combination with dynamical mean field theory. The remaining of the thesis is divided in three themed chapters.

Chapter 3: The first theme comprises the rare-earth elements. These atoms are found in a wide range of functional materials and it is very important to have a practical theoretical tool to describe them. Several attempts have been made to determine the electronic structure of the rare earths with *ab initio* methods. These elements are characterized by the localized nature of the $4f$ electrons and the itinerant character of the other valence electrons. Since density functional theory with the common parametrizations of the exchange-correlation functional cannot capture the correlated f electrons, more sophisticated theories have been tried [4, 81, 30, 88]. Although some of these methods turned out to be very accurate for selected properties, none of them can give a unified picture of the physics of the rare earths. In Paper I we intend to do precisely this. We propose density functional theory plus dynamical mean field theory within the Hubbard I approximation to describe the interesting physics of the rare-earth metals and rare earth containing materials. In Chapter 3 we introduce the reader to several defining properties of the rare earths and we try to make insightful why the Hubbard I approximation is expected to perform well. In Paper I we examine a wide range of properties of the rare-earth metals and we argue that our theory can be a firm basis for the future investigation of generic rare-earth based materials. In Paper II we use the excellent performance of the Hubbard I approximation to calculate the stacking fault energies in γ -Cerium.

Chapter 4: The second theme is related to the field of ultrafast magnetization dynamics. The possibility of manipulating the magnetization within a few hundreds of femtoseconds [12] has induced great excitement in the scientific community. This field is characterized by femtosecond dynamics resulting in corresponding strongly-out-of-equilibrium physics. Needless to say, this out-of-equilibrium physics is very complicated to address theoretically. In Chapter 4 and Paper III we intend to connect theory to experiments performed in the field of ultrafast magnetization dynamics. Or, in other words, we want to connect the microscopic physics of the system to the properties that are probed in the experiments. We propose a model that is based on statistical arguments for a system in a partial thermal equilibrium. We identify the microscopic configuration of the system directly after the ultrafast magnetization dynamics have finished. This model makes it possible to connect theoretical calculations originating at the microscopic level to averages of macroscopic quantities. With our predictions we can calculate the dielectric response around the $3p$ absorption edge of Fe at the end of the ultrafast magnetization dynamics, but before the full equilibrium is recovered. This dielectric response is compared to the experimentally measured T-MOKE asymmetry [86, 93].

Chapter 5: The third theme has a more methodological nature. Strongly correlated materials are currently of great interest and exhibit many exotic effects which may be important for technological applications. However, it is very difficult to determine their electronic structure. The increase of computational power has lead to several computational methods, such as dynamical

mean field theory or the *GW* approach. Most implementations of these methods, perform parts of the calculations in the imaginary-time or imaginary-frequency domain for technical reasons. Since real physical quantities depend on real time or real energies instead, a reliable tool is required to obtain those quantities from the functions in the imaginary-time or imaginary-frequency domain. These tools are commonly referred to as methods of analytic continuation. In Chapter 5 we briefly introduce several methods of analytic continuations. Paper V, VI and VII are closely connected to this chapter. In Paper V we propose a remedy to the well-known problems of the Padé approximant method by performing an average of several continuations, obtained by varying the number of fitted input points and Padé coefficients independently. We subject this method to extensive performance and reliability tests for one-particle Green's functions. In Paper VI we focus on dynamical two-particle quantities, instead, and evaluate the strengths and weaknesses of several different methods of analytic continuation. In Paper VII we switch our attention to computational performance. We investigate the advantages of implementing a method of analytic continuation based on stochastic sampling [70] on a graphics processing unit (GPU). This implementation allows to save computational time on supercomputer clusters by allowing extensive calculations to be performed on a common laptop.

Having outlined the structure of this thesis, I wish you an enjoyable reading of it!

2. Methods

IN this chapter we will provide a background to the methods to calculate the electronic structure of materials used in this thesis. In Sec. 2.1 we describe the general *problem-to-solve* in solid state physics and in Sec. 2.2 we arrive at density functional theory (DFT) as one of the possible (approximate) ways to calculate the electronic structure.

Despite the approximations that have to be made to the exchange-correlation functional, standard DFT works very well for a large class of materials. However, for some materials, strong correlations have to be taken into account. One way to do this is to combine DFT with the dynamical mean field theory (DMFT), which is explained in Sec. 2.3. The chapter closes with the Hubbard I approximation (HIA), which is an approximation to DFT+DMFT.

This method chapter is related to the other chapters in quite different ways. In Paper I we show that the DFT+DMFT(HIA) method is very suitable to describe several properties of the REs. In Chapter 3 we introduce these properties and also try to make insightful why the HIA is advisable for this class of elements. In Paper III and Chapter 4 we develop a model to predict the microscopic state directly after ultrafast magnetization dynamics. In this project, DFT calculations are only a small part of a larger whole. Chapter 5 is actually a method chapter, dedicated to a special problem encountered in DMFT, *i.e.* the analytic continuation. In most DMFT implementations, quantities are calculated as a function of imaginary time or imaginary frequency. However, real world quantities are measured as a function of real time or real frequency. To compare theory and experiment, one has to obtain these quantities from the calculated ones. In Paper V, VI and VII, we investigate several methods how to do this. In this sense, Chapter 5, in which these papers are prefaced, is an other method chapter, specifically tailored to methods of analytical continuation.

In the current chapter we only briefly mention technicalities related to our implementation of DFT+DMFT. In Sec. 2.2.4 we outline the difference between the basis sets employed by the codes used in Paper I, II and III. However, we refer the interested reader to these papers or to Ref. [62] for more precise details on the basis. The latter is my licentiate thesis, where I explain the code and the basis used in Paper I, and the corresponding choices and optimizations of the basis for the lanthanides. This method chapter is largely based on Chapter 3 of my licentiate thesis [62].

2.1 Solid state Hamiltonian

A collection of atoms consists of nuclei and electrons which all interact. This results in a Hamiltonian with 5 different terms. Two kinetic terms, one for the electrons and one for the nuclei and three Coulomb terms. The latter describe the attraction between the positively charged nuclei and the negatively charged electrons and the repulsion between electrons and nuclei themselves. For simplicity we will ignore the relativistic effects, but the Schrödinger equation can be generalized to the Dirac equation. The above described Hamiltonian looks quite simple. However, already for a few atoms, the computational effort needed for a full quantum mechanical solution runs out of control and we are left with an unsolvable Hamiltonian. The first simplifying approximation is given by the Born-Oppenheimer approximation [16] which separates the electronic and ionic degrees of freedom. Given that the kinetic term is inversely proportional to the mass, the kinetic term of the nuclei is much smaller than the kinetic term of the electrons. To describe the electronic degrees of freedom, the positions of the nuclei can be approximated as fixed, constituting a static external potential for the electrons. The Hamiltonian for the electronic degrees of freedom reduces then to

$$\hat{H} = \frac{-\hbar^2}{2m_e} \sum_i \nabla_i^2 + \sum_i V_{\text{ext}}(\mathbf{r}_i) + \frac{1}{2} \sum_{i \neq j} \frac{e^2}{|\mathbf{r}_i - \mathbf{r}_j|}, \quad (2.1)$$

where the indices i and j run over the different electrons. The kinetic energy of the electrons is given in the first term, where \hbar is the Planck constant, m_e the electron mass and $-i\hbar\nabla$ the momentum operator. The external potential due to the ions is given in the second term and the last term is the Coulomb repulsion between the electrons. Although this Hamiltonian can be diagonalized for a few electrons, it quickly becomes impossible to do so when approaching macroscopic solids. However, that is precisely what one would like to do, since the eigenvalues of this Hamiltonian give the energy of the system and the eigenfunctions give the electron many-body wave functions.

Before discussing how to tackle this problem, let us present the second simplification one can make. This is based on the translational invariance of a crystal. For translational invariant systems, the Bloch theorem [15] states that the (one-electron) wave function ψ can be written as a periodic function $u(\mathbf{r})$, with the same periodicity as the crystal lattice under consideration, times a plane wave:

$$\psi_{\mathbf{k}}(\mathbf{r}) = u_{\mathbf{k}}(\mathbf{r})e^{i\mathbf{k}\cdot\mathbf{r}}, \quad (2.2)$$

where \mathbf{k} is the reciprocal lattice vector.

Although the Born-Oppenheimer approximation and the use of the Bloch theorem greatly simplify the task of diagonalizing the Hamiltonian described in the beginning of this section, a solution is still unreachable for more than

a few atoms and electrons. However, thanks to Pierre C. Hohenberg, Walter Kohn, Lu Jeu Sham and many others, we nowadays have a very successful way to tackle this problem: Density Functional Theory (DFT).

2.2 Density Functional Theory

The brilliant ideas that initiated the development of DFT were given by Pierre C. Hohenberg, Walter Kohn and Lu Jeu Sham. Roughly speaking, Pierre C. Hohenberg and Walter Kohn stated that if you have the ground-state density of the particles in space and the interaction between the particles, you have, in principle access to any property of the system. They formulated this statement more precisely in two theorems known as the Hohenberg-Kohn theorems [45]. Later Walter Kohn and Lu Jeu Sham came with the Kohn-Sham *ansatz* [54] that opened the route to modern DFT. The book *Electronic Structure* by Martin [64] is a very good reference, both for the fundamentals of DFT as well as for practical electronic structure calculations. The current section is mainly based on chapters 6 and 7 of this book.

2.2.1 Hohenberg-Kohn theorems

The Hohenberg-Kohn theorems lead to a simplification of the many-electron problem by shifting the attention from the wave function, that depends on the position vectors of all electrons simultaneously, to the density, that depends on one position vector only. Precisely formulated, the Hohenberg-Kohn theorems [64] read:

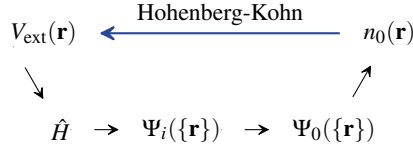
Theorem 1 *For any system of interacting particles in an external potential $V_{\text{ext}}(\mathbf{r})$, the potential $V_{\text{ext}}(\mathbf{r})$ is determined uniquely, except for a constant, by the ground-state particle density $n_0(\mathbf{r})$.*

Corollary 1 *Since the Hamiltonian is thus fully determined, except for a constant shift of the energy, it follows that the many-body wave functions for all states (ground and excited) are determined. Therefore all properties of the system are completely determined given only the ground-state density $n_0(\mathbf{r})$.*

Theorem 2 *A universal functional of the energy $E[n]$ in terms of the density $n(\mathbf{r})$ can be defined, valid for any external potential $V_{\text{ext}}(\mathbf{r})$. For any particular $V_{\text{ext}}(\mathbf{r})$, the exact ground-state energy of the system is the global minimum value of this functional, and the density $n(\mathbf{r})$ that minimizes the functional is the exact ground-state density $n_0(\mathbf{r})$.*

Corollary 2 *The functional $E[n]$ alone is sufficient to determine the exact ground-state energy and density. In general, excited states of the electrons must be determined by other means.*

For the actually surprisingly simple proofs of these theorems I would like to refer the reader to the nice explanation in chapter 6 of *Electronic Structure* by Martin [64]. In the scheme below, I summarize the first Hohenberg-Kohn theorem, which will be related to the Kohn-Sham *ansatz* later in this text.



With capital Ψ_i we denote the many-body wave functions and the subscript zero denotes the ground state. Starting from the external potential $V_{\text{ext}}(\mathbf{r})$ and going counter clock wise, one recognizes the scheme from quantum mechanics. With the potential the Hamiltonian \hat{H} can be constructed, that enters the Schrödinger equation. Solving the Schrödinger equation gives the wave functions $\Psi_i(\mathbf{r})$, including the ground state $\Psi_0(\mathbf{r})$. From the ground-state wave function, the ground-state density can be obtained. The blue arrow, that closes the circle, is the first Hohenberg-Kohn theorem: from the ground-state density the external potential is uniquely defined (except for a constant shift).

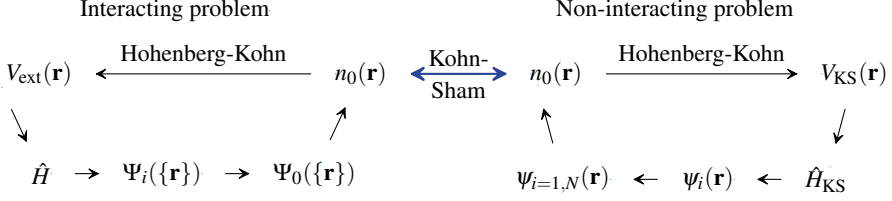
The second Hohenberg-Kohn theorem affirms the existence of a universal energy functional $E[n]$. Later it will turn out to be useful to write this functional in four different terms belonging to the different terms in the Hamiltonian in Eq. 2.1:

$$E_{\text{HK}}[n] = T[n] + E_{\text{int}}[n] + \int d^3r V_{\text{ext}}(\mathbf{r})n(\mathbf{r}) + E_{\text{II}}. \quad (2.3)$$

T denotes the kinetic energy of the electrons and E_{int} is the electron-electron interaction energy. The third term is the energy associated to the external potential that the electrons experience due to the positions of the nuclei. The last term is the energy of the nuclei, which is however, not written in Eq. 2.1.

2.2.2 Kohn-Sham *ansatz*

The second groundbreaking idea that opened the route to large scale application of DFT was the *ansatz* of Walter Kohn and Lu Jeu Sham [54]. Their idea was to replace the original (interacting) many-body problem with an auxiliary independent-particle problem, where the auxiliary system is chosen such that the ground-state density is the same as the ground-state density of the interacting problem. This Kohn-Sham *ansatz* has two main advantages. First, it makes it possible to use non-interacting methods to calculate, in principle exactly, the properties of a fully interacting many-body system. Second, the combination of the Hohenberg-Kohn theorems and the Kohn-Sham *ansatz* leads to good approximations of the universal energy functional in Eq. 2.3. The marriage of the Hohenberg-Kohn theorems and the Kohn-Sham *ansatz* is presented below



The right part of the scheme is the auxiliary problem and the left part is the original interacting problem. Note that the capitalized Ψ denotes a many-body wave function, where the ground state is denoted by Ψ_0 and the excited states by Ψ_i . On the right hand side, the normal ψ_i is the i -th wave function in the non-interacting problem. For a system with N electrons, the first N single-particle wave functions are occupied in the ground state. Instead of solving the interacting (left) problem, one focusses on the auxiliary (right) problem. This is done by constructing the auxiliary potential $V_{\text{KS}}(\mathbf{r})$, solving the Schrödinger equation for the non-interacting Hamiltonian \hat{H}_{KS} and obtaining the single-particle wave functions $\psi_i(\mathbf{r})$. These first N wave functions provide the ground-state density, which is linked to the interacting problem. This leads to the Kohn-Sham equations (in Hartree units):

$$(\hat{H}_{\text{KS}} - \varepsilon_i)\psi_i(\mathbf{r}) = 0 \quad (2.4a)$$

$$\hat{H}_{\text{KS}}(\mathbf{r}) = -\frac{1}{2}\nabla^2 + V_{\text{KS}}(\mathbf{r}) \quad (2.4b)$$

$$V_{\text{KS}}(\mathbf{r}) = V_{\text{ext}}(\mathbf{r}) + V_{\text{Hartree}}(\mathbf{r}) + V_{\text{XC}}(\mathbf{r}) \quad (2.4c)$$

$$E_{\text{KS}}[n] = T_s[n] + \int d^3r V_{\text{ext}}(\mathbf{r})n(\mathbf{r}) + E_{\text{Hartree}}[n] + E_{\text{II}} + E_{\text{XC}} \quad (2.4d)$$

$$n(\mathbf{r}) = \sum_{i=1}^N |\psi_i(\mathbf{r})|^2. \quad (2.4e)$$

The Kohn-Sham Hamiltonian \hat{H}_{KS} (Eq. 2.4b) is non-interacting and therefore Eq. 2.4a is numerically solvable in a finite Hilbert space. The many-body effects are hidden in the exchange-correlation part V_{XC} of the potential V_{KS} . The *universal functional* $E[n]$ from the Hohenberg-Kohn theorems is, however, not known and thus $E_{\text{KS}}[n]$ is an approximation instead. For this approximation, the kinetic energy is split into the non-interacting part $T_s[n]$ and the remaining part is included in V_{XC} . Moreover, the complicated electron-electron interaction term is split into two parts. The main part is captured by the Hartree potential

$$V_{\text{Hartree}}(\mathbf{r}) = \frac{\delta E_{\text{Hartree}}[n]}{\delta n(\mathbf{r})}, \quad (2.5)$$

where the Hartree energy is

$$E_{\text{Hartree}}[n] = \frac{1}{2} \int d^3r d^3r' \frac{n(\mathbf{r})n(\mathbf{r}')}{|\mathbf{r} - \mathbf{r}'|}, \quad (2.6)$$

which is the electron density interacting with itself. The remaining part of the electron-electron interaction is again included in the exchange correlation potential. Hence, the exchange correlation potential includes the difference between the real (interacting) kinetic energy and the non-interacting kinetic energy $T_s[n]$, and the difference between the electron-electron interaction and the Hartree potential. The exchange correlation energy (E_{XC} in Eq. 2.4d) is formally given by comparing the Kohn-Sham energy (Eq. 2.4d) with the Hohenberg-Kohn energy (Eq. 2.3). This is however a formal definition that is not extremely useful since we do not know the Hohenberg-Kohn energy functional. However it is insightful to see where the approximations are made as we will see in the next section.

The Kohn-Sham equations built an effective potential from a density, an external potential and the approximated exchange-correlation potential. This effective potential results into a new density, which constitutes a new exchange-correlation potential and a new effective potential. Therefore, the Kohn-Sham equations must be solved self-consistently in the effective potential and the density. This is schematically shown in Fig. 2.1. As a self-consistent method, the Kohn-Sham approach uses independent-particle techniques, but describes interacting densities.

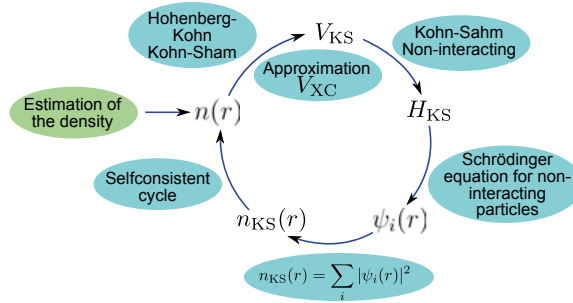


Figure 2.1. Schematic view of the DFT cycle: solving the Kohn-Sham equations self-consistently.

The Hohenberg-Kohn energy functional is unknown, but the Kohn-Sham *ansatz* enables one to do very good approximations. The division of the kinetic energy and the Coulomb interaction into a known part and an unknown part results in a total unknown part (the exchange-correlation energy) of two (hopefully) small terms. 1. The difference between the interacting and non-interacting kinetic energies. 2. The difference between the Hartree energy and the full electron-electron interaction energy. The exchange-correlation energy can be reasonably well approximated by a local, or nearly local, quantity, as the Hartree term includes the long-range Coulomb interaction. This short-range character of V_{XC} is the main cause of the huge success of DFT. Due to

this main progress in approximating the unknown exact universal energy functional, density functional theory is so widely applied in physics and chemistry.

2.2.3 Approximations to the energy functional

As said, the exact functional for going from the density $n(\mathbf{r})$ to the Kohn-Sham potential $V_{\text{KS}}[n]$, e.g. in the scheme in Fig. 2.1, is not known. We also mentioned briefly why DFT became so successful nonetheless. Firstly, the Kohn-Sham approach allows one to use independent-particle theories to solve a fully interacting many-body problem. Secondly, the fact that the long-range Coulomb interaction (Hartree term) and the independent particle kinetic energy are separated out allows one to approximate the exchange-correlation functional by a quantity that is approximately local. Utilizing the nearly local nature of the exchange-correlation potential has resulted in very good approximations. Examples of these are the Local (Spin) Density Approximation (L(S)DA) and the Generalized Gradient Approximation (GGA). This paragraph will shortly describe these two functionals. A more elaborate overview of these and other functionals can be found in, for example, chapter 8 of the book *Electronic Structure* by Martin [64].

In many materials the electrons behave as itinerant and this nearly-free electron behavior was exploited to construct the first approximation of the exchange-correlation function. In the local density approximation (LDA), the exchange-correlation functional is directly derived from the uniform electron gas, where it is a local quantity. In this case the exchange energy can be calculated analytically. For the correlation energy an approximation is made by means of Monte Carlo calculations on the uniform electron gas. The resulting LDA functional has the same functional dependence on the density as is found for the uniform electron gas. The only difference is that the uniform density $n = N/V$ is replaced by the density at a given point $n(\mathbf{r})$. Generalizing this functional to two different spin channels yields the local spin density approximation.

Generally the range of effects of exchange and correlation is small and the L(S)DA functional is a good approximation. However, one should notice that the approximations made are not based on a formal expansion around some small parameter. This means that the accuracy of the local approximation can not be formally proven and one has to test the validity of the approximation for each case separately. The latter can be done by comparing theory and experiment or calculated and exact solutions, if available. Nonetheless, the DFT community has developed some intuition on the applicability of different functionals. For example, one expects the LDA functionals to perform well for systems where the electrons behave as nearly-free, and one expects them to work bad for systems where the electron density is distributed very inho-

mogeneously in space. The latter is for example the case of the $4f$ -electron density in the rare earths, where DFT fails all together.

An intuitive first step to improve the LDA functionals is to use not only the density at a certain point in space, but also its gradient. The first attempts to include the gradients did not work very well. Especially for large gradients the expansions performed poorly. After a few attempts, more elaborate ways to take the gradient into account were developed which worked very well. This class of functionals was named generalized gradient approximation (GGA). Generally, the GGA functionals perform better than the LDA functionals. The usual underestimation of the equilibrium volume calculated with an LDA function is exemplary for this. The GGA functionals often predict equilibrium volumes that are closer to the experimental values.

2.2.4 LMTO and LAPW bases

To solve the Kohn-Sham equations, a basis is chosen and the wave functions are expressed as linear combinations of the basis functions. In the works included in this thesis, we mainly used two electronic structure codes. For the calculations in Papers I and II we used the *Relativistic Spin-Polarized test* (RSPt) code, which is an all-electron full-potential linear muffin-tin orbital (FP-LMTO) method [97]. The dielectric tensor in Papers III and IV was calculated using ELK [1], which is an all-electron full-potential linearised augmented-plane wave (FP-LAPW) code. In this section we briefly describe the similarities and differences of these two sets of basis functions.

In the construction of the LMTOs and the LAPWs, the geometry of the problems at hand, that is a certain arrangement of atoms, is taken into account. The space is divided into two qualitatively different regions. In a sphere around the atom, the potential is dominated by the spherically symmetric Coulomb potential of the nucleus. In the region between these atomic spheres, the Coulomb potential is screened and the remaining potential is nearly constant. The space is therefore divided into spheres around the atom (muffin-tin spheres), and an interstitial region between the spheres. The name muffin-tin spheres arises from how a spherical potential inside the atomic spheres and a constant potential in between the atomic spheres would look like. This reminds us of the, although only two dimensional, muffin-tin mold (Fig. 2.2), which is used to bake muffins or cupcakes. The strength of this approach is that one can use different basis functions in the two regions, optimized to describe the special properties of these regions. The functions inside the MT are chosen such that they can very accurately describe the strongly varying Coulomb potential of the nucleus. In contrast to the functions in the interstitial, that are tailored to describe the nearly flat interstitial potential. Note that the division into muffin-tin spheres and interstitial is merely a geometrical separation that is used to construct the basis functions and that in both FP-LMTO



Figure 2.2. Muffin-tin mold. The division of the space for the construction of LMTOs and LAPWs resembles a muffin-tin mold, i.e. a spherical potential around the atoms (the cake mold) and a constant potential in between the atoms (in between the cakes the mold is flat). In LMTO-ASA this is actually the form of the potential. In FP-LMTO and FP-LAPW it is merely a geometrical separation that is used to construct the basis functions. Thanks to my friend Laura there is even something tasty inside the mold.

and FP-LAPW no geometric approximations are made on the actual shape of the potential.

Both the LMTO and LAPW bases originate from the same paper by Andersen [2]. They are constructed with free electron solutions in the interstitial region that are augmented with solutions of the Schrödinger equation with a spherical potential close to the nuclei. Also both methods rely on the concept of linearization, which greatly reduces the computational effort, while staying sufficiently accurate. Inside the muffin-tin region, both bases consist of solutions $\phi_l(r, \epsilon_v)$ of the radial Schrödinger equation with the spherical average of the Kohn-Sham potential. Here the concept of linearization enters and the Schrödinger equation is evaluated at a certain energy ϵ_v instead of treating the full energy dependence of ϕ_l . The radial wave function is expanded around a given energy ϵ_v , using $\phi(\epsilon_v, r)$ and its energy derivative $\dot{\phi}(\epsilon_v, r)$ evaluated at ϵ_v . The expansion reads: $\phi(\epsilon, r) = \phi(\epsilon_v, r) + (\epsilon - \epsilon_v)\dot{\phi}(\epsilon_v, r)$. The difference between LMTO and LAPW originates in the interstitial region. Where the LMTO method uses free electron solutions in radial coordinates, i.e. spherical Bessel and Neumann functions at different energies, the LAPW method uses plane waves at different wave vectors \mathbf{k} instead. In both bases, the free electron solutions in the interstitial are matched to the atomic-like functions in the muffin tin at the muffin-tin boundary. See Fig. 2.3 for an impression of the two bases.

Key features of both the RSPt code with the LMTO basis and the ELK code with the LAPW basis is that they are both all-electron, full-potential codes. “All-electron” refers to the fact that both the core and the valence states are relaxed and that no pseudo-potentials are used. Both codes are full-potential codes, since no approximation to the geometry of the potential is made. More-

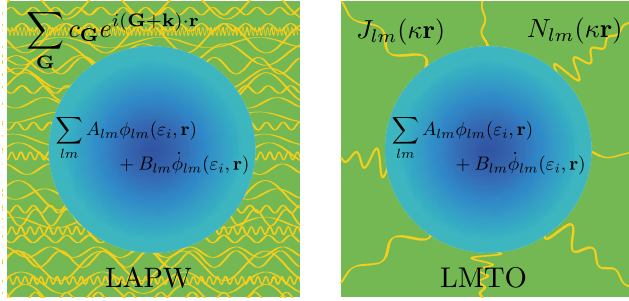


Figure 2.3. Sketch of the LAPW (left) and the LMTO basis (right). The basis in the interstitial consists of plane waves (LAPW), with reciprocal lattice vectors \mathbf{k} and \mathbf{G} (with \mathbf{k} in the first Brillouin zone) or Bessel J_{lm} and Neumann N_{lm} functions (LMTO) that are augmented with solutions to the Schrödinger equation with a spherical potential inside the muffin-tin sphere. The coefficients A_{lm} and B_{lm} are determined by the matching conditions at the muffin-tin boundary.

over, both methods reasonably balance completeness of the basis with computational effort. However, the different description of the interstitial region implies some advantages and disadvantages for both methods:

	Advantage	Disadvantage
LAPW	The number of augmented plane waves can easily be saturated until the quantity under investigation is converged with respect to the basis.	Increasing systematically the number plane waves requires more computational effort, see also Fig. 2.3.
LMTO	The basis functions resemble atomic-like wave functions which makes the basis very compact and efficient.	Reaching sufficient completeness of the basis is not straightforward, see also Chapter 5 of Ref. [62].

Hence, despite of the difference between plane waves and site centered basis functions, both bases are actually more similar than different and the physical results they give are very similar. In Ref. [61] we contributed with the RSPt code to a benchmark test that investigated the reproducibility of DFT results among different codes. Both the ELK and the RSPt code are present in this study and they give essentially identical results. A more elaborate explanation of both basis sets can be found in Ref. [64]. More details on the FP-LMTO basis used specifically in RSPt can be found in Refs. [97, 96, 27, 14].

2.3 Hubbard I approximation

In Paper I and II, discussed in Chapter 3 we focus on the lanthanides. In the lanthanides, the $4f$ electrons are very localized, whereas the $[spd]$ bonding

electrons are very delocalized. The latter can be described with the common LDA or GGA parametrizations of the exchange-correlation functional. The localized $4f$ electrons, however, are very poorly described by LDA or GGA. This is intuitively understandable, since these functionals are based on the uniform electron gas and one tries to describe very localized and thus non-uniform electrons. There are different methods to include the effects of (strong) localization in different situations. The two standard computational methods nowadays are LDA+U or LDA+Dynamical Mean-Field Theory (LDA+DMFT). The latter is more sophisticated than the former, but they have the same historical origin. Although the usual LDA (GGA) approach can not describe the localized nature of correlated electrons, it had been shown that the Hubbard model [46, 47, 48], with material-dependent parameters obtained from LDA describes various correlated materials very well [24, 77, 42, 41, 66]. These observations led to the idea of embedding this model Hamiltonian into DFT. As a result, the properties arising from the Hubbard model merged with DFT become now material-dependent quantities. The main idea is to add an explicit Hubbard interaction term, *i.e.* an on-site Coulomb repulsion tensor U , to the Kohn-Sham Hamiltonian for the strongly localized electrons only. This corrected Hamiltonian can now be written in the form of a Hubbard model Hamiltonian. In both LDA+U and LDA+DMFT this lattice Hamiltonian is mapped onto a Single Impurity Anderson Model (SIAM). In the mapping procedure the local Green's function is conserved. In LDA+U, the impurity Green's function of the SIAM is found in the Hartree Fock approximation. In LDA+DMFT, the impurity Green's function is calculated with one of the possible "solvers". In this thesis the Hubbard I Approximation (HIA) is used as an approximated solver of the SIAM. The approximation in the HIA is that the hybridization effects are neglected. The HIA provides therefore a good method to describe the lanthanides, since the $4f$ electrons are very localized and the hybridization of the f electrons is very small as discussed in Paper I and Chapter 3. Roughly speaking the main idea of the Hubbard I approximation is to combine the many-body structure of the $4f$ states, given by the atomic multiplets, with the broad bands of the delocalized valence electrons, see Fig. 2.4.

In the following sections we will aim at illustrating the main idea of DMFT following the scheme below

Lattice problem		Impurity problem
$\hat{H}^{\text{LDA}} + \hat{U} = \dots = \hat{H}^{\text{Hubbard Model}}$	\longrightarrow	$\hat{H}^{\text{Anderson Model}} \xrightarrow{\text{approximations}} \text{Solution}$

The approach is also illustrated in Fig. 2.5 and in the following we will frequently refer to the scheme and the figure. Note that the scheme and the figure do not involve the cycle where the dynamical mean field is updated. This choice is made, since in the Hubbard I approximation this field does not change. In Sec. 2.3.1 we explain how to merge DFT with the Hubbard

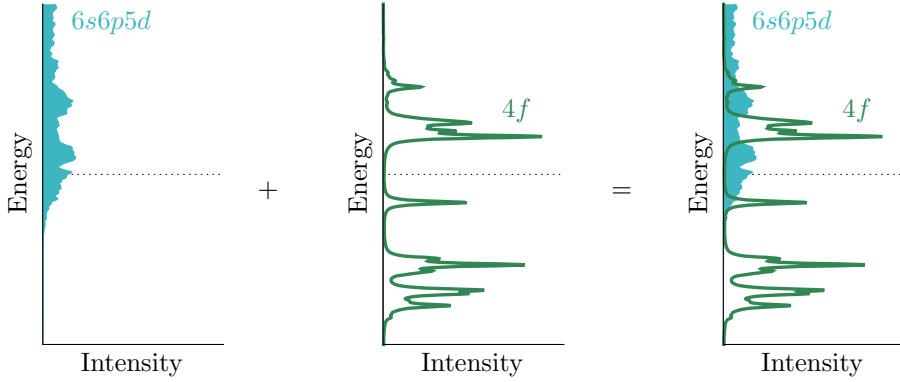


Figure 2.4. The idea of the Hubbard I approximation is to combine the LDA (GGA) description of the delocalized conduction electrons (light blue density of states) with the atomic multiplets of the localized $4f$ electrons (green solid multiplets).

model. In Sec. 2.3.2 the mapping procedure to the SIAM is explained. Finally we explain how the Hubbard I approximation is implemented in RSPt [97] in Sec. 2.3.3. The following sections are based mainly on the introductory lectures of Antoine Georges [33] and the PhD thesis of Igor Di Marco [27].

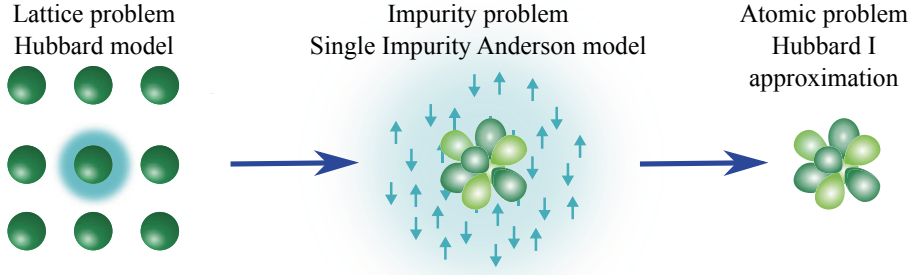


Figure 2.5. In the Hubbard I approximation the lattice problem is mapped to an impurity problem which is simplified into an atomic problem.

2.3.1 Effective Hubbard model

In this section we show how the Hubbard model is merged with DFT. This is the blue part (left) of the illustrating scheme introduced previously

$$\begin{array}{ccc}
 \text{Lattice problem} & & \text{Impurity problem} \\
 \hat{H}^{\text{LDA}} + \hat{U} = \dots = \hat{H}^{\text{Hubbard Model}} & \longrightarrow & \hat{H}^{\text{Anderson Model}} \xrightarrow{\text{approximations}} \text{Solution}
 \end{array}$$

The LDA+DMFT approach is based on the idea of merging LDA and the Hubbard model. In a heuristic way, one adds a Hubbard interaction term to the DFT-LDA Hamiltonian for those orbitals where the description in LDA

is not good enough due to strong on-site Coulomb repulsion. The adjusted Hamiltonian reads

$$\hat{H}^{\text{HUB}} = \sum_{\substack{\mathbf{R}_i, \mathbf{R}_j \\ \chi_i, \chi_j}} H_{\mathbf{R}_i, \mathbf{R}_j}^{\text{LDA}} \hat{c}_{\mathbf{R}_i \chi_i}^\dagger \hat{c}_{\mathbf{R}_j \chi_j} + \frac{1}{2} \sum_{\mathbf{R}} \sum_{\substack{\xi_1, \xi_2, \\ \xi_3, \xi_4}} U_{\xi_1 \xi_2 \xi_3 \xi_4} \hat{c}_{\mathbf{R} \xi_1}^\dagger \hat{c}_{\mathbf{R} \xi_2}^\dagger \hat{c}_{\mathbf{R} \xi_4} \hat{c}_{\mathbf{R} \xi_3} - \sum_{\mathbf{R}} \hat{H}_{\mathbf{R}}^{\text{DC}}, \quad (2.7)$$

where the LDA Hamiltonian is projected onto one-particle site-centered orbitals labeled by the Bravais lattice site vector \mathbf{R} and the set of quantum numbers χ . The orbitals for which the local correction tensor U is added, are usually called the “correlated orbitals”. This set of orbitals is labeled by a general orbital index ξ . Later on we will split ξ in more well-known quantum numbers, but in principle other classifications can be used. In an atomic-like basis this would correspond to the spin-orbitals $\{l, m, \sigma\}$. The operators $\hat{c}_{\mathbf{R}}^\dagger$ and $\hat{c}_{\mathbf{R}}$ are the creation and annihilation operators for electrons in the site-centered or the correlated orbitals. Some of the correlation effects explicitly added by the interaction term U are already (wrongly) taken into account in the LDA Hamiltonian. The double counting term $\hat{H}_{\mathbf{R}}^{\text{DC}}$ corrects for this by subtracting these contributions from \hat{H}^{HUB} . This term has the form $\hat{H}_{\mathbf{R}}^{\text{DC}} \sim \sum_{\xi_1} \hat{c}_{\mathbf{R} \xi_1}^\dagger \hat{c}_{\mathbf{R} \xi_1}$ and is sometimes merged with the chemical potential. We will elaborate more on this term in Fig. 2.7 and Sec. 2.3.5, but for the moment let us ignore it.

Written in this form, the corrected LDA Hamiltonian \hat{H}^{HUB} can be viewed as a Hubbard model Hamiltonian. The hopping term

$$t_{\mathbf{R}_1 \chi_1, \mathbf{R}_2 \chi_2} = H_{\mathbf{R}_1, \mathbf{R}_2}^{\text{LDA}} = \int d\mathbf{r} \langle \mathbf{R}_1 \chi_1 | \mathbf{r} \rangle \hat{H}^{\text{LDA}}(\mathbf{r}) \langle \mathbf{r} | \mathbf{R}_2 \chi_2 \rangle \quad (2.8)$$

comes from the LDA problem and the on-site repulsive interaction U is added on top of that. Note, however, that U is not the bare Coulomb repulsion, but an effective interaction. This effective interaction is based on the Coulomb repulsion, but is screened by the other electrons. We will discuss the heuristically added U -tensor in Sec. 2.3.4.

2.3.2 Effective Single impurity Anderson model

Now that we have a material-dependent Hubbard model Hamiltonian time has come to solve it. An efficient way to obtain physical quantities from this Hamiltonian is provided by the dynamical mean-field theory. In DMFT the effective Hubbard model, introduced in Sec. 2.3.1, is mapped onto an effective model, the single impurity Anderson model (SIAM). The SIAM considers a single impurity embedded in an effective field, as illustrated in the middle of Fig. 2.5. This way of solving the Hubbard model corresponds to solving the problem in a mean-field approach for the space degrees of freedom. The quantum degrees of freedom at a single site are, however, still accounted exactly. The mapping procedure is highlighted in the second part of the scheme

below

$$\begin{array}{ccc} \text{Lattice problem} & & \text{Impurity problem} \\ \hat{H}^{\text{LDA}} + \hat{U} = \dots = \hat{H}^{\text{Hubbard Model}} & \longrightarrow & \hat{H}^{\text{Anderson Model}} \xrightarrow{\text{approximations}} \text{Solution} \end{array}$$

Before focussing on the mapping procedure, we will briefly outline the single impurity Anderson model that provides the effective Hamiltonian for the mapping procedure. The Hamiltonian of the SIAM describes the impurity, the effective bath and the coupling between them:

$$\hat{H}^{\text{Eff}} = \hat{H}^{\text{SIAM}} = \hat{H}^{\text{At}} + \hat{H}^{\text{Bath}} + \hat{H}^{\text{Coupling}}. \quad (2.9)$$

The first term consists of two contributions $\hat{H}^{\text{At}} = \hat{H}^U + H^{\text{At},0}$. For the one-orbital case, one can merge $H^{\text{At},0}$ with the chemical potential, such that $H^{\text{At},0}$ contributes zero. Hence, for simplicity, we will assume for now a one-orbital case with the single orbital level to be located at the Fermi level, but we will mention where generalizations should be made. The interacting part of the atomic Hamiltonian is given by

$$\hat{H}^U = U \hat{c}_{\uparrow}^{\dagger} \hat{c}_{\uparrow} \hat{c}_{\downarrow}^{\dagger} \hat{c}_{\downarrow}, \quad (2.10)$$

where the \hat{c} -operators denote the creation (\hat{c}^{\dagger}) and annihilation (\hat{c}) of electrons in the impurity orbital. Note that the subscript \mathbf{R} is superfluous in the *single* impurity Anderson model.

The second term of Eq. 2.9 accounts for the energy of the bath. In the original SIAM, the bath consists of real conduction electrons. In DMFT, however, it consists of fictitious electrons that arise from the mapping procedure. The bath term reads

$$\hat{H}^{\text{Bath}} = \sum_{\mathbf{k}, \sigma} \epsilon_{\mathbf{k}, \sigma} \hat{a}_{\mathbf{k}, \sigma}^{\dagger} \hat{a}_{\mathbf{k}, \sigma}, \quad (2.11)$$

where the \hat{a} -operators denote the creation (\hat{a}^{\dagger}) and annihilation (\hat{a}) operators of electrons in the bath with spin quantum number σ and an additional generic quantum number \mathbf{k} . The energy of the bath electrons is $\epsilon_{\mathbf{k}, \sigma}$.

Finally the last term of Eq. 2.9 represents the coupling between the impurity, *i.e.* \hat{c} -operators, and the bath, *i.e.* \hat{a} -operators

$$\hat{H}^{\text{Coupling}} = \sum_{\mathbf{k}, \sigma} V_{\mathbf{k}, \sigma} \hat{a}_{\mathbf{k}, \sigma}^{\dagger} \hat{c}_{\sigma} + V_{\mathbf{k}, \sigma}^{*} \hat{c}_{\sigma}^{\dagger} \hat{a}_{\mathbf{k}, \sigma}, \quad (2.12)$$

where $V_{\mathbf{k}, \sigma}$ is the coupling parameter for electrons hopping from the bath to the impurity or back.

For a multi-orbital system, the U tensor in Eq. 2.10 and the creation and annihilation operators are labeled by the quantum numbers ξ as in Eq. 2.7 and a sum over these generic quantum numbers is required. Similarly in Eq. 2.12 the $\hat{c}^{(\dagger)}$ operators and the coupling $V_{\mathbf{k}, \sigma}$ pick up the supplementary label ξ and

the summation extends also over this generic quantum number. Additionally the term $H^{\text{At},0}$ in H^{At} in Eq. 2.9 is required to account for the energy of the impurity electrons:

$$H^{\text{At},0} = \sum_{\xi_i, \xi_j} \epsilon_{\xi_i \xi_j} \hat{c}_{\xi_i}^\dagger \hat{c}_{\xi_j}, \quad (2.13)$$

where the energy of the impurity electrons is obtained from the LDA Hamiltonian projected onto the correlated orbitals. As said, for the remainder of the explanation of the SIAM, we focus on the single impurity Anderson model with the impurity level positioned at zero.

In DMFT the mapping of the Hubbard model to the Single Impurity Anderson model is done such that the local Green's function at a single site in the lattice problem is the same as the impurity Green's function of the effective SIAM. To achieve this, the mapping parameters $\epsilon_{\mathbf{k},\sigma}$ and $V_{\mathbf{k},\sigma}$ should be set correctly. In reality these parameters are not needed explicitly. We will see in the following that only the dynamical field Δ_σ should be found. The local Green's function at a single site in the lattice problem is defined as a function of the creation and annihilation operators in the lattice problem. In DMFT the focus is on the correlated orbitals ξ and the local Green's function for these orbitals reads:

$$G_{\mathbf{R}\xi_1\xi_2\sigma}^{\text{Loc}}(\tau - \tau') \equiv -\langle \mathcal{T} \hat{c}_{\mathbf{R}\xi_1\sigma}(\tau) \hat{c}_{\mathbf{R}\xi_2\sigma}^\dagger(\tau') \rangle, \quad (2.14)$$

where \mathcal{T} denotes the time ordering operator and τ the imaginary time in the Matsubara formalism. If $\tau > \tau'$, an electron is created in orbital ξ_2 by $\hat{c}_{\mathbf{R}\xi_2\sigma}^\dagger(\tau')$ at time τ' , it propagates through the system until it is annihilated at time τ in orbital ξ_1 by $\hat{c}_{\mathbf{R}\xi_1\sigma}(\tau)$. On the other hand, if $\tau' > \tau$, a hole is created in orbital ξ_1 by $\hat{c}_{\mathbf{R}\xi_1\sigma}(\tau)$ which propagates until it is annihilated in orbital ξ_2 by $\hat{c}_{\mathbf{R}\xi_2\sigma}^\dagger(\tau')$. In the SIAM, the impurity Green's function is defined as the Green's function associated to the impurity operators \hat{c} in Eqs. 2.10, 2.12 and 2.13. The impurity Green's function reads:

$$G_{\xi_1\xi_2\sigma}^{\text{Imp}}(\tau - \tau') \equiv -\langle \mathcal{T} \hat{c}_{\xi_1\sigma}(\tau) \hat{c}_{\xi_2\sigma}^\dagger(\tau') \rangle. \quad (2.15)$$

In order to find the mapping parameters $\epsilon_{\mathbf{k},\sigma}$ and $V_{\mathbf{k},\sigma}$, it is convenient to split this impurity Green's function into a non-interacting impurity Green's function and a self-energy that contains the interactions. To obtain the non-interacting part, the term in Eq. 2.10 is equated to zero. The following expression for the non-interacting part of the impurity Green's function can be found either by using the effective action functional integral formalism and integrating out the bath degrees of freedom [33], or by using the equations of motion for the c and a operators [84]. The non-interacting impurity Green's function then reads:

$$\mathcal{G}_\sigma^{\text{Imp},0} = [(i\omega_n + \mu)\mathbb{1} - \hat{H}^{\text{At},0} - \Delta_\sigma(i\omega_n)]^{-1}, \quad (2.16)$$

where Δ_σ is the hybridization function that contains the parameters $\epsilon_{\mathbf{k},\sigma}$ and $V_{\mathbf{k},\sigma}$ of the effective system

$$\Delta_\sigma(i\omega_n) = \sum_{\mathbf{k}} \frac{|V_{\mathbf{k},\sigma}|^2}{i\omega_n - \epsilon_{\mathbf{k},\sigma}}. \quad (2.17)$$

With this, we can formally rewrite the effect of the two-particle term contained in \hat{H}^U in the form of a self-energy function $\Sigma_\sigma^{\text{Imp}}(i\omega_n)$. This function can be determined by several techniques, named “solvers”. The Dyson equation relates the interacting Green’s function to the non-interacting Green’s function and the self-energy:

$$G_\sigma^{\text{Imp}}(i\omega_n) = \left[\left(\mathcal{G}_\sigma^{\text{Imp},0}(i\omega_n) \right)^{-1} - \Sigma_\sigma^{\text{Imp}}(i\omega_n) \right]^{-1}. \quad (2.18)$$

In DMFT, the approximation is made that the lattice self-energy is local or in other words k -independent. With this approximation, the lattice self-energy can be directly related to the impurity self-energy

$$\Sigma_{\mathbf{R}\mathbf{R}',\sigma}(i\omega_n) = \delta_{\mathbf{R}\mathbf{R}'} \Sigma_\sigma^{\text{Imp}}(i\omega_n). \quad (2.19)$$

There are three limiting cases where the DMFT approximation is exact. The first case is trivial and is the non-interacting limit. If $U = 0$, the self-energy is zero and thus trivially local. The second exact limit was proven by Metzner and Vollhardt [69] who showed that the DMFT approximation is exact in the limit of infinite nearest neighbors or infinite dimensions. The third limit is the atomic limit, where the hopping between nearest neighbors in Eq. 2.8 of the Hubbard model becomes zero $t_{R_1,\chi_1,R_2,\chi_2} \sim \delta_{R_1,R_2}$. This results in $\Delta_\sigma(i\omega_n) = 0$ which implies a self-energy that has only on-site components. The Hubbard I approximation, which is an approximate solver to the SIAM in DMFT, is build upon this limit. It involves an additional approximation on top of the DMFT approximation that can be viewed in different ways. In the Hamiltonian of the effective system, *i.e.* Eq. 2.9, the coupling between the bath and the impurity, is neglected. For the self-energy this boils down to approximating the self-energy in the impurity problem by the atomic self-energy. Using this approximate solver for DMFT results in a lattice self-energy that is approximated by the atomic self-energy

$$\Sigma_{\mathbf{R}\mathbf{R}',\sigma}(i\omega_n) = \delta_{\mathbf{R}\mathbf{R}'} \Sigma_\sigma^{\text{At}}(i\omega_n). \quad (2.20)$$

The above described procedure, where the Hubbard model (Eq. 2.7) is mapped onto the single impurity Anderson model (Eq. 2.9) and then approximated by an atomic problem is schematically depicted in Fig. 2.6, which is an extended version of Fig. 2.5. The mapping procedure is no longer exact. In full DMFT, one has to find $\epsilon_{\mathbf{k},\sigma}$ and $V_{\mathbf{k},\sigma}$ and the resulting hybridization function

Δ and self-energy Σ that reproduce the correct G_{σ}^{Imp} , such that $G_{\sigma}^{\text{Imp}}(i\omega_n) = G_{\sigma}^{\text{Loc}}(i\omega_n)$. This is the core ingredient of the mapping procedure in full DMFT. In the HIA, however, the hybridization function is neglected and the atomic self-energy is taken instead of the true self-energy. Hence, the hybridization function needs not to be found self-consistently. The crucial approximation ($V_{\mathbf{k},\sigma} = 0$) is made and this method can only give sensible results if the correlated orbitals are close to atomic-like. Or, in other words, if the hybridization is very small. In this thesis we only mention the Hubbard I Approximation as an approximate solver for the SIAM in DMFT, since it is a good approximation for the rare earths. However, there are several other possible solver that are appropriate for other particular cases. In the scheme that was leading in this section, the solvers are the last part:

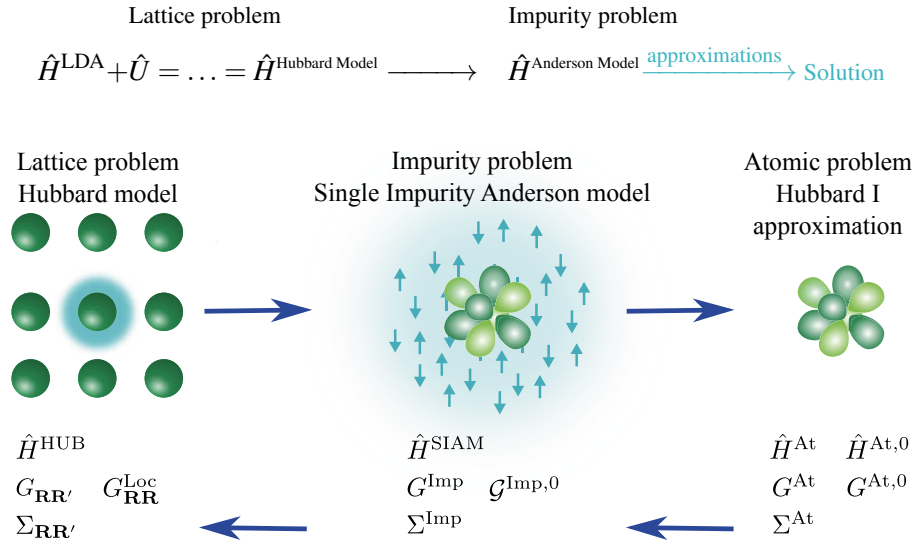


Figure 2.6. In the Hubbard I approximation the lattice problem is mapped to an impurity problem which is simplified into an atomic problem. The self-energy is calculated in the simplified case and the real self-energy is approximated by the atomic self-energy.

2.3.3 Computational scheme

In Paper I we thoroughly investigated the Hubbard I approximation for the elemental rare-earth metals and in Paper II we used this HIA to support the calculations done with the 4*f*-in-the-core method. In this section we briefly outline the computational scheme of HIA that we used in these works, *i.e.* the HIA implementation in the RSPt code [97].

As a guidance to the reader, we sketched the computational scheme for the Hubbard I approximation in Fig. 2.7. First the Kohn-Sham Hamiltonian H^{LDA}

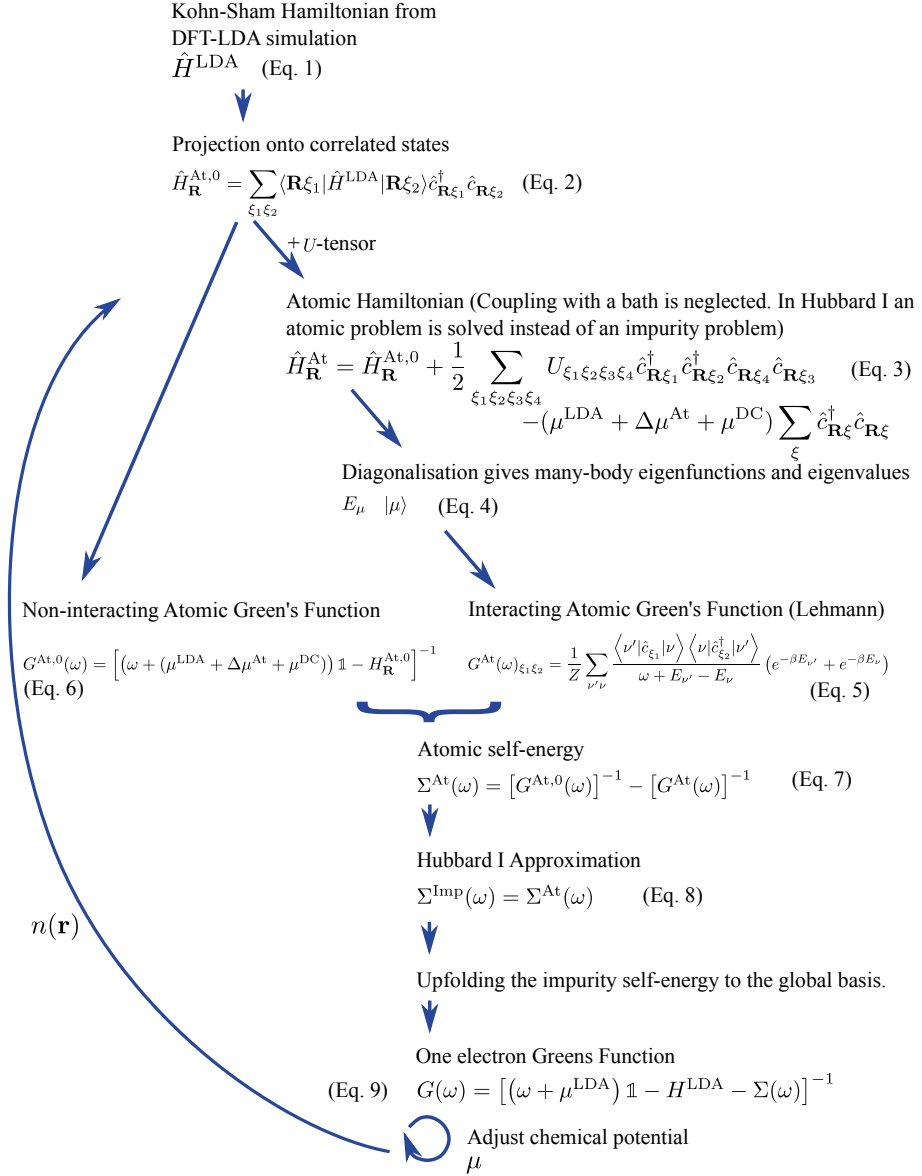


Figure 2.7. Outline of the HIA cycle. The symbols are explained in the text.

coming from the DFT-LDA part in a global basis χ is projected onto the correlated states denoted with a generic set of quantum numbers ξ on site \mathbf{R} . In case of the lanthanides, H^{LDA} is projected onto the atomic-like $4f$ states. This is Eq. 2 in Fig. 2.7 or Eq. 2.13 in the previous section. The resulting Hamiltonian $\hat{H}_{\mathbf{R}}^{\text{At},0}$ is written on a many-body basis of Fock states and the on-site Coulomb repulsion tensor U (Eq. 2.10 in the previous section) is added. The resulting $\hat{H}_{\mathbf{R}}^{\text{At}}$ in Eq. 3 in Fig. 2.7 also contains the terms $(\mu + \Delta\mu^{\text{At}} + \mu^{\text{DC}})$ that take into account the chemical potential of the Green's function coming in the first iteration from the LDA calculation, the correction due to the fact that the hybridization is ignored in the HIA and the double counting correction. In Sec. 2.3.5 we will elaborate a bit more on these terms. This Hamiltonian is diagonalized and the eigenvalues E_v and the eigenstates $|v\rangle$ are obtained. With the Lehman representation, the interacting atomic Green's function G^{At} (Eq. 5 in Fig. 2.7) is constructed. Meanwhile the non-interacting atomic Green's function is constructed from $\hat{H}_{\mathbf{R}}^{\text{At},0}$. The non-interacting Green's function $G^{\text{At},0}$ and the interacting Green's function G^{At} combined with the Dyson equation provide the atomic self-energy Σ^{At} in Eq. 7 of Fig. 2.7. The self-energy includes, as usual, the interactions of the system. The Hubbard I approximation consists in approximating the impurity self-energy with the atomic self-energy, as is done in Eq. 8 in Fig. 2.7. To return back to the lattice problem, the self-energy has to be up-folded to the global basis as in Eq. 2.19 or 2.20 in the previous section. This self-energy in the global basis is used to construct the one-electron Green's function in the global basis, as is shown in Eq. 9 in Fig. 2.7. Here the atomic features and the delocalized electrons are combined. The chemical potential μ is adjusted to get the right amount of particles. To allow the itinerant electrons to adjust to the changed potential of the correlated electrons, charge self-consistency is required. The density of the delocalized electrons has to be recalculated taking the new density of the localized electrons into account. This results in a slightly different H^{LDA} in Eq. 1 in Fig. 2.7. The loop has to be repeated until the density and the self-energy do not change significantly anymore between consecutive iterations.

The most important physical properties can be obtained through the lattice Green's function. A fundamental quantity to calculate is the spectral function, which is given by

$$\rho(\omega) = -\frac{1}{\pi} \text{Im}[G(\omega + i\delta)] \quad \delta \rightarrow 0, \quad (2.21)$$

where δ approaches 0 from the positive side. In computations δ will never be exactly zero and causes therefore a broadening in the spectrum.

2.3.4 Hubbard U and Hund's J

In this section we will elaborate on the U tensor and its relation to the Hubbard U and Hund's J . In our code we work directly with the full U -tensor. Because

of the atomic-like orbitals, the U -tensor can be expanded with help of spherical harmonics. The expansion [20, 27] is given by

$$U_{m_1\sigma_1,m_2\sigma_2,m_3\sigma_3,m_4\sigma_4} = \delta_{\sigma_1,\sigma_3}\delta_{\sigma_2,\sigma_4} \sum_{n=0}^{2l} a_n(m_1,m_3,m_2,m_4)F^n, \quad (2.22)$$

where the δ s ensure that the interaction does not change the spin of the electrons. The parameters a_n are integrals over products of three spherical harmonics. Their form is such that they are only non-zero if n is even and $n \leq 2l$. The Slater integrals F^n are given by

$$F^n = \int_0^\infty \int_0^\infty dr dr' r^2 r'^2 |\phi(r)|^2 |\phi(r')|^2 \frac{r_{<}^n}{r_{>}^{n+1}}, \quad (2.23)$$

where ϕ are the atomic radial wave functions and $r_{<}$ and $r_{>}$ denote the lesser and the greater between r and r' . The zeroth Slater integral is heavily screened. This means that a direct evaluation of Eq. 2.23 to obtain F^0 is nonsensical. However, for F^2 , F^4 and F^6 the screening is much smaller and the atomic Slater integrals are already very good approximations. Using the atomic F^2 , F^4 and F^6 has the advantage of not introducing an additional parameter to account for the small screening of these Slater integrals.

In our code we use the full U -tensor to calculate the self-energy. However, in Paper I and Paper II we frequently refer to the Hubbard U and Hund's J . These parameters are useful for an intuitive understanding of the effects of adding the U tensor to the Hamiltonian. In the remainder of this section we briefly comment on the physical meaning of the Hubbard U and Hund's J . For this, we consider two degenerate correlated orbitals in cubic symmetry described by real valued wave functions. In this case, the Coulomb interaction tensor can be rewritten as [44]:

$$\begin{aligned} & \frac{1}{2} \sum_{\substack{\xi_1, \xi_2, \\ \xi_3, \xi_4}} U_{\xi_1, \xi_2, \xi_3, \xi_4} \hat{c}_{\xi_1}^\dagger \hat{c}_{\xi_2}^\dagger \hat{c}_{\xi_4} \hat{c}_{\xi_3} \\ & \longrightarrow \frac{1}{2} \sum_{m, \sigma} U \hat{n}_{m\sigma} \hat{n}_{m\bar{\sigma}} + \frac{1}{2} \sum_{\substack{m, m', \sigma, \sigma' \\ m \neq m'}} ((U - 2J) \hat{n}_{m\sigma} \hat{n}_{m'\sigma'} - J \hat{n}_{m\sigma} \hat{n}_{m'\sigma}) \\ & \quad - \frac{1}{2} \sum_{\substack{m, m', \sigma \\ m \neq m'}} J \left(\hat{c}_{m\sigma}^\dagger \hat{c}_{m\bar{\sigma}}^\dagger \hat{c}_{m'\sigma} \hat{c}_{m'\bar{\sigma}} + \hat{c}_{m\sigma}^\dagger \hat{c}_{m\bar{\sigma}} \hat{c}_{m'\bar{\sigma}}^\dagger \hat{c}_{m'\sigma} \right). \quad (2.24) \end{aligned}$$

In this equation the general quantum number ξ of the correlated orbitals is split in a principal quantum number n , an angular quantum number l , an orbital quantum number m , and a spin quantum number σ . The principal quantum number and the angular quantum number subscripts are ignored since we consider all correlated orbitals to have the same n and l . Note that $\hat{n} = \hat{c}^\dagger \hat{c}$ is

the number operator and $\bar{\sigma}$ is a spin opposite to σ . The Hubbard U and Hund's J are parts of the Coulomb interaction tensor

$$\begin{aligned}
 U &= U_{mmmm} && \text{Intraorbital interaction} \\
 U - 2J &= U_{mm'mm'} && \text{with } m \neq m' \quad \text{Interorbital interaction} \\
 J &= U_{mm'm'm} && \text{with } m \neq m' \quad \text{Pair-hopping amplitude or exchange interaction.}
 \end{aligned} \tag{2.25}$$

The precise derivation of these relationships is not relevant here, since we only use Eq. 2.24 for an intuitive understanding of these parameters. The interested reader is referred to Refs. [44, 32, 62]. The meaning of U and J for the two-orbital system is illustrated in Fig. 2.8. This figure is a schematic view of a system consisting of two degenerate orbitals at zero energy and initially one electron in orbital 1. The question is, what is the energy cost to add 1 electron to this system? We could add this second electron in three ways and the energy cost ΔE can be found by applying the Hamiltonian in Eq. 2.24 to the initial

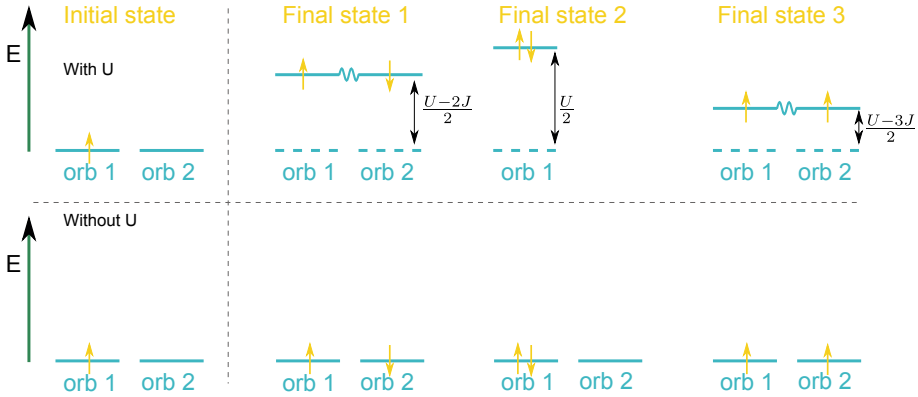


Figure 2.8. Schematic view of how the Hubbard U and Hund's J shift the “energy levels”. Energy levels are an intuitive way of understanding these numbers, but are a bit difficult to grasp in case of a many-body state. For simplicity we take two degenerate orbitals at zero energy. In the initial case we have one electron and two orbitals. In the final case, we have two electrons and a many-body state, which might be a sort of combination between the original two orbitals. This combination is denoted with a wiggly line between the orbitals. The position of the many-body orbital is such that, in order to obtain the energy of the system, you have to take the energy of the energy level times the occupancy of the level. The most left plots correspond to the initial situation with one electron in orbital 1. In the second column an electron with opposite spin is added to the second orbital. In the third column an electron with opposite spin is added to the same orbital and in the last column an electron with same spin is added to (of course) the other orbital. The top panels show the shift of the energy levels in the situation where the Coulomb repulsion is taken into account. The bottom panels show the situation where it is not taken into account, so the independent electron theory.

state and the final state. We neglected the terms in the last line of Eq. 2.24 which are considered to be small. This results in the following three possible energy costs for adding an electron

1. With opposite spin in the 2nd orbital: $\Delta E = \frac{U_{12}}{2} + \frac{U_{21}}{2} = U - 2J$
2. With opposite spin in the same orbital: $\Delta E = \frac{U_{11}}{2} + \frac{U_{11}}{2} = U$
3. With the same spin in the 2nd orbital: $\Delta E = \frac{U_{12}-J_{12}}{2} + \frac{U_{21}-J_{21}}{2} = U - 3J$

These energy costs are illustrated in Fig. 2.8.

The preceding discussion offers an idea of the different contributions to the U -matrix, but several approximations have been performed. These approximations were only made to simplify the understanding of the physics. In our code we use the full U -tensor to calculate the self-energy. The different Slater integrals are related by sum rules [20, 27] and can therefore be related to the Hubbard U and Hund's J . The former corresponds to the zeroth Slater integral $F^0 = U$ and is usually heavily screened. The Hund's J for f systems is given by $J = \frac{1}{6435}(286F^2 + 195F^4 + 250F^6)$ [20, 27].

2.3.5 Double counting

Finally we return to \hat{H}^{DC} in Eq. 2.7, which contains the last terms in Eq. 3 of Fig. 2.7, i.e. $(\mu + \Delta\mu^{\text{At}} + \mu^{\text{DC}})$. The first term μ is simply the chemical potential obtained from the DFT-LDA calculation in the first iteration. In charge self-consistent calculations it will be modified to account for the self-energy. The last term μ^{DC} is more tricky. As mentioned before the U -tensor is added to take into account the strong Coulomb interaction in the localized orbitals. However, part of this Coulomb repulsion is already accounted for in the DFT-LDA calculation, although not correctly. The double counting term μ^{DC} should correct for this. Moreover, in HIA, we neglect the coupling between impurity and bath, when mapping the electronic structure problem onto the SIAM. The term $\Delta\mu^{\text{At}}$ should in principle enforce the conservation of the particle number between the SIAM and the atomic model obtained in HIA. However in practice this is not needed. These two terms $\Delta\mu^{\text{At}}$ and μ^{DC} have in common that they are rigid shifts. Therefore they are sometimes grouped together into one term. Unfortunately it is not straightforward to know which contributions are exactly double counted and hence the choice of the double-counting correction is a somewhat arbitrary procedure. Several schemes for the double counting have been proposed and used in different situations. In Tab. 2.1 we summarize the double-counting schemes relevant for the HIA and used in the Papers I and II. We will explain them briefly below.

Fix position of the first (un)occupied peak

This scheme acknowledges the fact that we do not know the exact expression for the double counting and introduces an additional parameter to fix this lack of knowledge. This scheme is very convenient when comparing with experimental photoemission spectra. In this procedure, the position of the first occupied or the first unoccupied peak from theory is aligned to the position

Table 2.1. *Double counting corrections*

Double counting scheme	Input	Determines
Position of the first (un)occupied peak	$N^{\text{At}}, E^{\text{Peak}}$	$(\Delta\mu^{\text{At}} + \mu^{\text{DC}}) = H^{\text{DC}}(N^{\text{At}}, E^{\text{Peak}})$ μ is determined self-consistently
Fully Localized Limit (N)		$\mu^{\text{DC}} + \Delta\mu^{\text{At}} = H^{\text{DC}}(N)$ μ is determined self-consistently
Fully Localized Limit (N^{At})	N^{At}	$\mu^{\text{DC}} + \Delta\mu^{\text{At}} = H^{\text{DC}}(N^{\text{At}})$ μ is determined self-consistently

of this peak obtained in experiment, which has to be given as an external parameter. This allows for an easy comparison of the relative positions of the atomic multiplets. This double-counting correction is implemented such that once μ has been determined to obtain the correct number of electrons in the global system, $\Delta\mu^{\text{At}} + \mu^{\text{DC}}$ is adjusted to get the correct number of f electrons. Since the multiplets are well separated in energy, $\Delta\mu^{\text{At}} + \mu^{\text{DC}}$ is still undetermined within this range. Fixing the position of the first (un)occupied peak to the experimental position determines $\Delta\mu^{\text{At}} + \mu^{\text{DC}}$ univocally.

Fully localized limit

A legitimate protest against the previously described scheme is that introducing an additional parameter is not very *ab-initio*. The fully localized limit (FLL) double counting is an approximation that is without external parameters and that is frequently used together with the HIA. In the fully localized limit, the double counting energy is given by

$$E^{\text{DC}} = \frac{1}{2}UN(N-1) - J\frac{N}{2}\left(\frac{N}{2} - 1\right), \quad (2.26)$$

where N is the number of correlated electrons as calculated from the local Green's function. Alternatively one could choose the closest integer number to N instead [82]. The latter we label N^{At} and is very close to N for a true Hubbard I system.

The double counting Hamiltonian in Eq. 2.7, which is diagonal in ξ, ξ' , is obtained through:

$$\hat{H}_{\mathbf{R},\xi,\xi'}^{\text{DC}} = \begin{cases} \frac{\delta E^{\text{DC}}}{\delta \hat{n}_{\mathbf{R}\xi}} & \text{if } \xi = \xi', \\ 0 & \text{if } \xi \neq \xi'. \end{cases} \quad (2.27)$$

3. Lanthanides

The rare earths perplex us in our researches, baffle us in our speculations, and haunt us in our very dreams. They stretch like an unknown sea before us, mocking, mystifying, and murmuring strange revelations and possibilities.

— Sir William Crookes (1887)

THE lanthanides, which are the elements from Ba/La to Lu, or rare-earth (RE) elements¹ have very interesting properties, such as their large magnetic moment and anisotropy. Many of the characteristics of the REs arise from the very localized nature of the $4f$ electrons. The standard model of the lanthanides, which assumes a chemically inert $4f$ shell and $4f$ orbitals that are very close to atomic like, has been proven to work very well to describe and explain experimental findings. However, it has been difficult to connect *ab initio* electronic structure calculations to this model. Density functional theory, with the commonly used parameterizations of the exchange correlation functional (LDA/GGA), badly fails to correctly describe the localized nature of the $4f$ electrons and therefore most properties of the REs. More sophisticated theories have been tried, such as LDA+U [4], self-interaction correction (SIC) [81], orbital polarization [30], and a treatment of the $4f$ shell as core-like [88]. All these methods can describe certain properties very well, but fail to provide a unified picture of the physics of the REs. Especially a correct description of the valence band spectra is not within the possibilities of these methods. In Paper I we study density functional theory plus dynamical mean-field theory (DFT+DMFT) within the Hubbard I approximation (HIA) to describe a wide range of properties of the REs.

In this chapter we will provide a background to some of these properties. On the one hand this is a good introduction to Paper I and II, on the other hand it intuitively shows why the standard model of the lanthanides is so successful. We will focus in Sec. 3.1 on the electronic configuration of the REs, since all physical properties originate from this. In Sec. 3.2 we will describe the bonding properties of the REs. In Sec. 3.3 we mention the crystal structure of the elemental RE metals and discuss the phase diagram of cerium as a background to Paper II. We will continue in Sec. 3.4 with the ground-state magnetic moments of the lanthanides, which are very close to the atomic Hund's rule

¹The rare-earth elements also include Sc and Y, which are not part of the lanthanide series. However, I use the term rare earths synonymously to lanthanides in this thesis.

derived moments. Finally we arrive at the valence-band (inverse) photoemission spectra in Sec. 3.5. This introduction to the rare earths is largely based on Chapter 2 of my licentiate thesis [62].

At the end of this chapter we will summarize Paper I and II. In Paper I is shown how accurately DFT+DMFT within HIA can describe the different properties of the elemental rare earths. In Paper II we use this method to calculate the stacking fault energies of γ -cerium.

3.1 Outer electronic configuration

Across the lanthanides the $4f$ shell is gradually filled. The electronic configuration of an isolated atom with n electrons in the $4f$ shell is $[\text{Xe}]6s^25d^04f^n$, except for La, Gd and Lu that have a $5d$ electron more and one $4f$ electron less [7]. When the isolated atoms come together and form a solid, the discrete $6s$, $6p$ and $5d$ energy levels hybridize into an $[spd]$ band. A balance is found between the Coulomb energy to pay when adding a localized f electron and the kinetic energy to pay when adding an itinerant $[spd]$ electron. For most REs it is energetically favorable to promote one $4f$ electron to the $[spd]$ -band in the solid phase, which results in three $[spd]$ valence electrons. The exceptions to this are barium, europium and ytterbium that have an empty, half filled or filled shell in the atomic configuration. The Coulomb energy to pay when adding an f electron to obtain a half-filled or full shell is very small. These elements, with two $[spd]$ valence electrons are called divalent contrary to the other trivalent elements. In the following table the outer electronic configuration of the rare earths is given for the atomic (A) and the crystalline (C) phases.

	La	Ce	Pr	Nd	Pm
A	$5d^16s^2$	$4f^25d^06s^2$	$4f^35d^06s^2$	$4f^45d^06s^2$	$4f^55d^06s^2$
C	$[spd]^3$	$4f^1[spd]^3$	$4f^2[spd]^3$	$4f^3[spd]^3$	$4f^4[spd]^3$
	Sm	Eu	Gd	Tb	Dy
A	$4f^65d^06s^2$	$4f^75d^06s^2$	$4f^75d^16s^2$	$4f^95d^06s^2$	$4f^{10}5d^06s^2$
C	$4f^5[spd]^3$	$4f^7[spd]^2$	$4f^7[spd]^3$	$4f^8[spd]^3$	$4f^9[spd]^3$
	Ho	Er	Tm	Yb	Lu
A	$4f^{11}5d^06s^2$	$4f^{12}5d^06s^2$	$4f^{13}5d^06s^2$	$4f^{14}5d^06s^2$	$4f^{14}5d^16s^2$
C	$4f^{10}[spd]^3$	$4f^{11}[spd]^3$	$4f^{12}[spd]^3$	$4f^{14}[spd]^2$	$4f^{14}[spd]^3$

3.2 Bonding properties

The equilibrium atomic volumes of the elemental RE metals, *i.e.* crystals consisting of only one type of RE atoms, very intuitively show how the local-

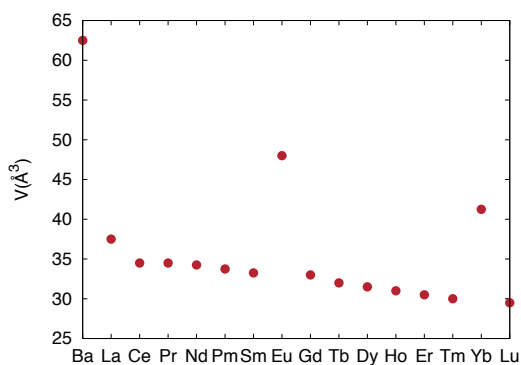


Figure 3.1. Experimental average atomic volume for the elemental rare-earth metals. The data are taken from Ref. [38].

ized nature of the $4f$ electrons determines the bonding properties. In Fig. 3.1 the experimental average atomic volume is shown for all elemental RE metals. Three characteristics are important to note. The most obvious is that the three divalent elements have a significantly larger volume than the trivalent elements. The second point is that all trivalent elements have a nearly constant volume across the series. The third important feature to notice is the slight contraction of the volume which can be seen across the elements.

From the nearly constant volume of the trivalent elements, one can deduce that the $4f$ electrons do not, or barely participate in the bonding. After all, adding or removing one f electron does not significantly change the volume. Contrary, the divalent elements that have one $[spd]$ electron less than the trivalent elements, have a noteworthy larger volume. This means that in the REs the $[spd]$ electrons are the bonding electrons. Last, but not least, the subtle lanthanide contraction: the slightly decreasing volume across the series. This is explained by incomplete screening. If one compares a rare-earth element to its neighbor to the left in the periodic table, one proton and one $4f$ electron are added. The $[spd]$ electrons experience the increasing core charge only partially, since the latter is very well, *but not completely* screened by the $4f$ electrons. The outer $[spd]$ states become contracted because this incomplete screening of the increased nuclear charge by the $4f$ states, when the series is traversed. This results in a small volume decrease.

As illustrated by the behavior of the volume across the series, the f electrons do barely contribute to the bonding. Also the behavior of the magnetic properties and the shape of the valence-band spectra of the rare earths is very close to atomic. This leads to the assumption of a chemically inert $4f$ shell. This assumption can make calculations involving lanthanides much easier. As-

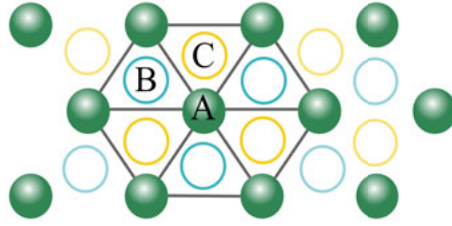


Figure 3.2. Top view of a close-packed lattice. If the first layer is formed by the green atoms, site A, the second layer can be placed at site B (blue) or site C (yellow). The order of the stacking determines the crystal structure.

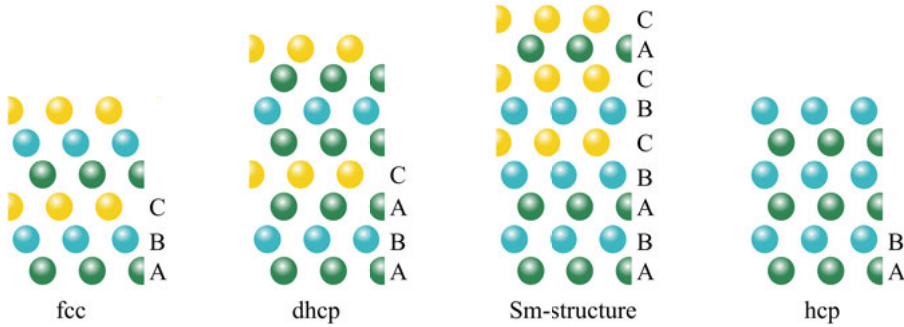


Figure 3.3. Side view of the different close-packed stacking orders. The order of the stacking determines the crystal structure.

suming a chemically inert $4f$ -shell is often denoted as the standard model of the lanthanides.

3.3 Structural stabilities

Also for the crystal structure of the RE metals, the localized nature of the $4f$ electrons is decisive. Since the $4f$ shell is very localized, the change in $4f$ filling barely modifies the outer regions of the atom. This means that all RE metals, except the divalent ones, have very similar properties, as we have already seen for the equilibrium volume in Sec. 3.2. The crystal structures of the trivalent elements are from light to heavy: fcc (Ce) \rightarrow dhcp (Pr,Nd) \rightarrow Sm-structure (Sm) \rightarrow hcp (Gd-Tm) [52], which are all close-packed structures with different stacking of a layer where the atoms are arranged in triangles, see Fig. 3.2. The order of the stacking determines the crystal structure as shown in Fig. 3.3 for the crystal structures of the RE metals. The structural phase diagrams of the RE metals are also very similar, as they all go through the following sequence with increasing pressure hcp \rightarrow Sm-structure \rightarrow dhcp \rightarrow fcc. This inspired B. Johansson and A. Rosengren [52] to compile a generalized phase diagram for all elemental RE metals. In Paper I we address the

structural stabilities of Ce, Pr and Nd. In Paper II we also look in detail at the different crystal phases of Ce, maybe the most intensively studied material amongst the elemental RE metals. Precisely this element does not entirely fit in the generalized phase diagram. Instead of the expected dhcp phase for low temperatures and pressures, an fcc structure is found. Around room temperature and only for low pressures, a small dhcp region is found and for higher temperatures Ce takes again an fcc structure [99]. However, the most interesting feature in the Ce phase diagram is the transition from the low pressure fcc (γ -) phase to the high pressure fcc (α -) phase. This is an isostructural transition with a dramatic volume collapse of about 15% around room temperature. Also the spectral weight changes from the γ - to the α -phase [44]. We will return to this phase diagram in Sec. 3.6 and Fig. 3.9.

In Paper II we study the energies of the different crystal phases. These energy differences are quite small, *i.e.* only tens of meV. From the energies of the different hexagonal stacking orders (Fig. 3.3) we calculate the stacking fault energies by using the axial interaction model [26, 21]. The stacking fault energies are quite small and errors in the stacking fault are relatively easily formed. The difference in the stacking fault energy in the γ and α phase gives insight in the hysteretic effects in the α - γ transition.

3.4 Magnetism

In this section we will briefly describe the ground-state magnetic moments of the REs. For the present we keep it simple and neglect crystal-field effects. Although, we will present a basic picture without crystal-field effects, for some of the rare earths, like Pr, they are extremely important. More specifically we will describe the coupling of spin and orbital moments as encoded in Hund's rules and the Russell-Saunders coupling scheme. In the end we will mention the paramagnetic moment and the saturation moment that are found in small and big fields respectively. For this section, and for my knowledge of magnetism in the REs, *Solid State Physics* by Ashcroft and Mermin [7], *Rare earth Magnetism* by Jensen and Mackintosh [51] and the Master's Thesis of N.E. Koch [53] were very useful.

3.4.1 Coupling of spin and orbital moments

The moments of the rare earths are well described in the Russell-Saunders (*LS*) coupling scheme, which is based on the assumption that spin-spin coupling is stronger than orbit-orbit coupling, which is stronger than spin-orbit coupling. The exchange interaction couples the spins \mathbf{s}^i of the individual electrons to a total spin angular momentum \mathbf{S} , with total spin quantum number $S = \sum_i m_s^i$ where m_s^i is the spin projection quantum number of electron i . Similarly, the Coulomb interaction couples the orbital angular momenta \mathbf{l}^i of the

individual electrons to a total orbital angular momentum \mathbf{L} . The corresponding total orbital angular momentum quantum number is $L = \sum_i m_l^i$, where the magnetic quantum number m_l^i specifies the projection of the orbital angular momentum of electron i along the quantization axis. These two couplings are summarized in Hund's first two, out of three, rules. These three Hund's rules make it possible to find the ground state:

1. Maximize S , taking into account the Pauli principle.
2. Maximize L , while satisfying the first rule.
3. Minimize J for less than half filled shells ($J = |L - S|$) or maximize J for more than half filled shells ($J = |L + S|$), while satisfying the first two rules.

The third Hund's rule describes the coupling of the spin and orbital angular momentum into the total angular momentum \mathbf{J} . The corresponding total angular momentum quantum number is given by $J = |L \pm S|$. The spin and orbital angular momenta are subtracted for less than half filled shells, since the energy is smallest for the state where $S_z = S$ and $L_z = -L$ have opposite sign. Contrary for more than half filled shells, where the energy is smallest when $S_z = S$ and $L_z = L$ have the same sign. In this case the spin and orbital angular momenta have to be added in order to obtain the total angular momentum quantum number. Here and from now on we indicate the quantization axis as the \hat{z} -axis for sake of simplicity.

3.4.2 Moments arising from the spin, orbital and total angular momenta

The moments associated to the spin and orbital angular momenta combine to a moment associated to the total angular momentum vector. The spin moment is:

$$\boldsymbol{\mu}_S = -\frac{g_s \mu_B}{\hbar} \mathbf{S}, \quad (3.1)$$

with gyromagnetic factor of the electronic spin $g_s \approx 2$ and Bohr magneton μ_B . The magnitude of this moment is $\mu_S = g_s \mu_B \sqrt{S(S+1)} \approx 2\mu_B \sqrt{S(S+1)}$, where we used that the eigenvalues of \mathbf{S}^2 are $\hbar^2 S(S+1)$. The magnitude of the orbital moment is

$$\mu_L = \mu_B \sqrt{L(L+1)}, \quad (3.2)$$

which is also directed opposite to \mathbf{L} . Note that the gyromagnetic factor for the orbital moment is $g_L = 1$, which is why it does not appear in Eq. 3.2.

The coupled moment as a function of the total angular momentum \mathbf{J} can be written in a similar form

$$\boldsymbol{\mu}_J = g_J \mu_B \sqrt{J(J+1)}, \quad (3.3)$$

where the Landé factor g_J has a more complicated form, due to the factor two in the spin moment that is not present in the orbital moment. The Landé factor

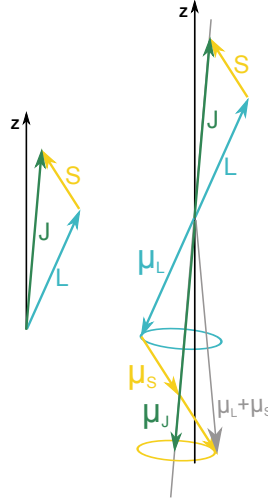


Figure 3.4. Vector representation of \mathbf{S} , \mathbf{L} and \mathbf{J} , and the corresponding moments. The vector representation is however a bit misleading, since we can not simultaneously know all components of the vector.

is:

$$g_J = 1 + \frac{J(J+1) + S(S+1) - L(L+1)}{2J(J+1)}, \quad (3.4)$$

which can be obtained as explained in the following. Fig. 3.4 illustrates in a schematic way the “vector addition” of \mathbf{S} , \mathbf{L} to \mathbf{J} and the addition of the corresponding moments. As can be seen in Fig. 3.4 the sum of $\boldsymbol{\mu}_S$ and $\boldsymbol{\mu}_L$ does not lie along $\hat{\mathbf{J}}$, which is the unit vector in the \mathbf{J} -direction. However, due to the Wigner-Eckart theorem, the expectation value $\langle \boldsymbol{\mu}_L + \boldsymbol{\mu}_S \rangle$ should. The total angular momentum \mathbf{J} precesses around $\hat{\mathbf{z}}$, and the projection of $\boldsymbol{\mu}_L + \boldsymbol{\mu}_S$ on the $\hat{\mathbf{J}}$ -axis has length

$$\mu_J = \frac{\mu_B}{\hbar} (\mathbf{L} \cdot \hat{\mathbf{J}} + 2\mathbf{S} \cdot \hat{\mathbf{J}}). \quad (3.5)$$

Using $\mathbf{L}^2 = (\mathbf{J} - \mathbf{S})^2$ to obtain an expression for $\mathbf{S} \cdot \hat{\mathbf{J}}$ and $\mathbf{S}^2 = (\mathbf{J} - \mathbf{L})^2$ to obtain an expression for $\mathbf{L} \cdot \hat{\mathbf{J}}$ leads to the g_J -factor in Eq. 3.4.

Note that we assumed that the field is not too strong so that \mathbf{S} and \mathbf{L} are coupled to \mathbf{J} . For strong fields, \mathbf{S} and \mathbf{L} would precess independently around the direction of the external field.

As a summary, the Hund’s rules ground state and the corresponding magnetic moments are listed in Tab. 3.1 for all rare earths. The \uparrow and \downarrow arrows indicate the m_s occupation of the m_l orbitals. The Hund’s rule ground state is, in zero field, $(2J+1)$ fold degenerate and all states $J_z = -J, -J+1, \dots, J-1, J$ have the same energy. In the next section we will see how a magnetic field splits this degeneracy. This leads to a magnetic moment that is different in weak or strong fields.

Table 3.1. *Hund's rules ground states and magnetic moments using Eq. 3.3 and 3.4.*

Element		-3	-2	-1	m_l 0	1	2	3	S	L	J	Moments $\mu_J (\mu_B)$
Ba	f^0								0	0	0	0
La	f^0								0	0	0	0
Ce	f^1	↑							$\frac{1}{2}$	3	$\frac{5}{2}$	2.535
Pr	f^2	↑	↑						1	5	4	3.578
Nd	f^3	↑	↑	↑					$\frac{3}{2}$	6	$\frac{9}{2}$	3.618
Pm	f^4	↑	↑	↑	↑				2	6	4	2.683
Sm	f^5	↑	↑	↑	↑	↑			$\frac{5}{2}$	5	$\frac{5}{2}$	0.845
Eu	f^7	↑	↑	↑	↑	↑	↑	↑	$\frac{7}{2}$	0	$\frac{7}{2}$	7.937
Gd	f^7	↑	↑	↑	↑	↑	↑	↑	$\frac{7}{2}$	0	$\frac{7}{2}$	7.937
Tb	f^8	↑↓	↑	↑	↑	↑	↑	↑	3	3	6	9.721
Dy	f^9	↑↓	↑↓	↑	↑	↑	↑	↑	$\frac{5}{2}$	5	$\frac{15}{2}$	10.646
Ho	f^{10}	↑↓	↑↓	↑↓	↑	↑	↑	↑	2	6	8	10.607
Er	f^{11}	↑↓	↑↓	↑↓	↑↓	↑	↑	↑	$\frac{3}{2}$	6	$\frac{15}{2}$	9.581
Tm	f^{12}	↑↓	↑↓	↑↓	↑↓	↑↓	↑	↑	1	5	6	7.561
Yb	f^{14}	↑↓	↑↓	↑↓	↑↓	↑↓	↑↓	↑↓	0	0	0	0
Lu	f^{14}	↑↓	↑↓	↑↓	↑↓	↑↓	↑↓	↑↓	0	0	0	0

3.4.3 Magnetic moments in a magnetic field

In experiments [51], the magnetic moments can be measured in two different ways. The paramagnetic moment can be extracted from the magnetic susceptibility above the ordering temperature. The saturation moment can be measured in magnetic fields that align the atomic magnetic moments. In this section we briefly mention the difference between these two moments.

In the presence of a magnetic field the Hamiltonian has two extra contributions. First, the momentum operator of each electron is modified with the vector potential \mathbf{A} , *i.e.* $\mathbf{p}_i \rightarrow \mathbf{p}_i + \frac{e}{c}\mathbf{A}(\mathbf{r}_i)$, where $-e$ the charge of an electron and c the speed of light. Second, the interaction between the spin and the magnetic field is taken into account: $g_s\mu_B\mathbf{H} \cdot \mathbf{S}$, where \mathbf{H} is the magnetic field in the $\hat{\mathbf{z}}$ -direction that the individual moments experience. The field dependent terms in the Hamiltonian are

$$\Delta\hat{H} = \mu_B(\mathbf{L} + g_s\mathbf{S}) \cdot \mathbf{H} + \frac{e^2}{8m_e c^2} H^2 \sum_i (x_i^2 + y_i^2), \quad (3.6)$$

where the terms $\mu_B\mathbf{L} \cdot \mathbf{H}$ and $\frac{e^2}{8m_e c^2} H^2 \sum_i (x_i^2 + y_i^2)$ originate from the modification of the momentum operator due to the vector potential. The terms in

Eq. 3.6 induce energy shifts that are generally quite small and can be treated with perturbation theory. For a state defined by the quantum numbers $n = \{J, L, S, J_z\}$, the energy shift is

$$\Delta E_n = \mu_B \mathbf{H} \cdot \langle n | \mathbf{L} + g_s \mathbf{S} | n \rangle + \sum_{n' \neq n} \frac{|\langle n | \mu_B \mathbf{H} \cdot (\mathbf{L} + g_s \mathbf{S}) | n' \rangle|^2}{E_n - E_{n'}} + \frac{e^2}{8mc^2} H^2 \langle n | \sum_i x_i^2 + y_i^2 | n \rangle + \dots \quad (3.7)$$

We now focus on the case where $J \neq 0$ in a small field in the $\hat{\mathbf{z}}$ -direction. In this case the first term in the above equation is usually dominant over the other two which can be neglected. We assume that the separation between the zero field ground-state multiplet, given by the Hund's rules, and the first excited multiplet with a different J is much bigger than $k_B T$ and that only the $(2J+1)$ states within this ground-state multiplet will contribute to the moment. The energy splitting, given in the above equation, then splits the $(2J+1)$ fold degenerate Hund's rule ground state in states with $J_z = -J, -J+1, \dots, J-1, +J$. The $(2J+1)$ -dimensional matrix $\langle JLSJ_z | \mathbf{L}_z + g_s \mathbf{S}_z | JLSJ'_z \rangle$ can be simplified using the Wigner-Eckart theorem

$$\langle JLSJ_z | \mathbf{L}_z + g_s \mathbf{S}_z | JLSJ'_z \rangle = g(JLS) J_z \delta_{J_z J'_z}, \quad (3.8)$$

where $g(JLS) = g_J$ the same Landé g_J -factor as in Eq. 3.4. For clarity we will skip the arguments (JLS) of the g_J -factor. Since J_z runs from $-J$ to J in integer steps, it follows from Eqs. 3.7 and 3.8 that the dominant energy separation between the J_z levels in the ground-state J multiplet is $g_J \mu_B H$. The paramagnetic and the saturation moment can be obtained in the case were $k_B T \gg g_J \mu_B H$ and $k_B T \ll g_J \mu_B H$ respectively, as illustrated in the middle of Fig. 3.5. In the following paragraphs we will calculate the paramagnetic and the saturated moment.

Curie's law $k_B T \gg g_J \mu_B H$

To obtain the paramagnetic moment of a collection of identical atoms of angular momentum J , one calculates the magnetic Helmholtz free energy $F = -\frac{1}{\beta} \ln(\mathcal{Z})$ for the excited states at energy $E_n(H) = g_J \mu_B H J_z$, where \mathcal{Z} is the partition function. The exponentiated magnetic Helmholtz free energy is

$$\begin{aligned} e^{-\beta F} &= \sum_n e^{-\beta E_n(H)} = \sum_{J_z=-J}^J e^{-\beta g_J \mu_B H J_z} \\ &= \frac{e^{\beta g_J \mu_B H (J+1/2)} - e^{-\beta g_J \mu_B H (J+1/2)}}{e^{\beta g_J \mu_B H / 2} - e^{-\beta g_J \mu_B H / 2}}. \end{aligned} \quad (3.9)$$

In the last line the geometric series was summed to simplify the expression. The magnetization M per volume V for N ions is given by

$$M = -\frac{N}{V} \frac{\delta F}{\delta H} = \frac{N}{V} g_J \mu_B J B_J(\beta g_J \mu_B J H), \quad (3.10)$$

where we have introduced the Brillouin function $B_J(x)$. This function saturates to 1 for large $x = \beta g_J \mu_B J H$, which implies that at large fields all moments align and contribute to the magnetization. We will come back to this in the next paragraph. However first we consider the case, when the splitting between the different energy levels in the zero-field ground-state multiplet is much smaller than $k_B T$. In this situation many levels contribute to the magnetization. The Brillouin function can be expanded around small x , which leads to the magnetic susceptibility

$$\chi = \frac{\delta M}{\delta H} = \frac{N}{V} \frac{(g_J \mu_B)^2}{3} \beta J(J+1). \quad (3.11)$$

This susceptibility can be rewritten as a function of the paramagnetic moment in Curie's law:

$$\chi = \frac{\delta M}{\delta H} = \frac{1}{3} \frac{N}{V} \frac{\mu_B^2 p^2}{k_B T} \quad (3.12)$$

where p is the effective Bohr magneton number and is given by

$$p = g_J \sqrt{J(J+1)} = \frac{1}{\mu_B} \mu_J \quad (3.13)$$

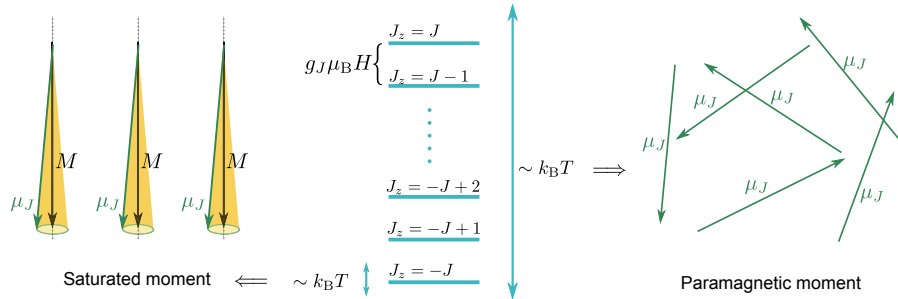


Figure 3.5. Schematic representation of the saturated moment and the paramagnetic moment. In the middle a schematic energy-level diagram (blue energy levels) of the ground-state J -multiplet is shown with the two temperature regimes. Note that, equivalently to decreasing the temperature, the field can be increased. For the saturated moment the direction of the moments is fixed along the \hat{z} -axis, therefore the maximum value it can take is the maximal projection of the vector μ_J (black arrow in left plot). For the paramagnetic moment the direction of the individual moments is not specified, therefore it can take the full moment μ_J associated to the vector \mathbf{J} as in Eq. 3.3 (green arrow in right plot). However in particular in this case the vector representation is misleading, since we can not simultaneously know all components of the vector.

A schematic representation of the paramagnetic moment, *i.e.* μ_J in Eqs. 3.13 and 3.3 that is deduced from Curie's law is illustrated in Fig. 3.5 (right).

Saturation moment $k_B T \ll g_J \mu_B H$

When the energy splitting due to the field is much bigger than temperature, only the lowest J_z of the zero field ground-state multiplet contributes. Each atomic magnetic moment saturates at the maximum value $J_z = J$, which gives a saturation value of

$$M = \frac{N}{V} g_J \mu_B J. \quad (3.14)$$

A schematic representation of the saturated moment is given in Fig. 3.5 (left). Since we can not know all three components of μ_J simultaneously, the saturation moment is the projection (black arrow) of μ_J (green arrow) on the \hat{z} -axis.

3.5 Spectral properties

The last property crucial for the understanding of the physics of the REs is the valence band spectrum. The spectral function as obtained in dynamical mean-field theory (DMFT) can be related more or less directly to X-ray Photoelectron Spectroscopy (XPS) and Bremsstrahlung Isochromat Spectroscopy (BIS) experiments. In this section we briefly explain these spectroscopies that probe the occupied and unoccupied part of the valence band respectively. A very good explanation and more details focussed on the lanthanides can be found in chapter 62 of *Handbook on the physics and chemistry of the rare earths* by Gschneidner and Eyring [40].

3.5.1 Spectroscopy

In photoemission experiments, *e.g.* XPS, a monochromatic photon beam of known energy irradiates the sample. The energy transferred to the sample excites electrons that are emitted from the sample and their energy and intensity distribution is measured. The original energy position of the emitted electrons can be deduced from the measured energy of the electrons and the known energy of the photon beam. In this way the occupied part of the spectrum is probed, since the probability of the transitions is mainly determined by the electrons just below the Fermi level. The process is illustrated in Fig. 3.6(a).

Contrary, in inverse photoemission experiments, *e.g.* BIS, the sample is irradiated with a mono-energetic electron beam and emits photons. In Fig. 3.6(b) a sketch is made of this experiment. In energy space it is easiest to understand the process: the impinging electrons couple to high lying unoccupied states and decay to lower unoccupied states by emitting photons. The energy and intensity distribution of these photons is measured. The energy of the available

(unoccupied) states just above the Fermi level can be deduced from the photon energies and the energy of the incoming electron beam.

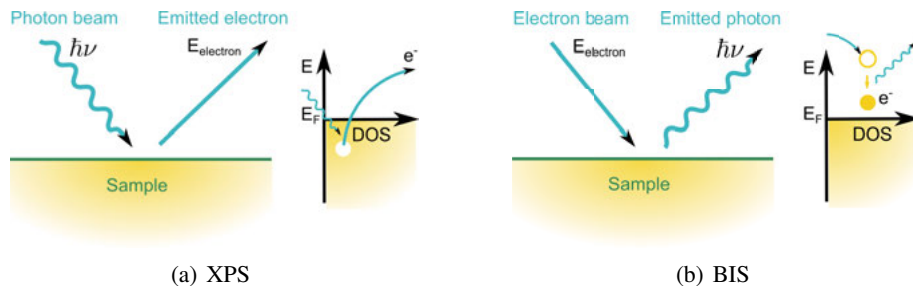


Figure 3.6. Schematic view of a photoemission experiment (left) and of an inverse photoemission experiment (right).

In the lanthanides, the spectra are mainly defined by the atomic $4f$ multiplet structure. However, also the other angular momenta contribute and the total spectrum is a superposition of the density of states for the different angular momenta l weighted by their cross sections. The cross sections give the probability for transitions from states with a certain angular momentum and depend on the photon energy of the impinging beam. This difference in transition probability enhances or suppresses states of a given angular momentum compared to states of a different angular momentum. This could change the relative heights of the different peaks in the spectrum compared to the peaks in the spectral function.

3.5.2 Experiment and theory

The photoemission spectroscopy data can be related more or less directly to the spectral function calculated in DMFT. However, some differences are worth noting. In a true atomic $4f$ multiplet structure, one expects atomic sharp lines. However, both in experiment and theory one finds broad peaks instead. In the measurements there are two main reasons for this. The first reason is the finite lifetime of the final state, that can be modeled theoretically with a Lorentzian broadening. The second reason is the finite resolution of the measurement apparatus, which can be theoretically simulated with a Gaussian broadening, where the full width at half maximum (FWHM) is given by the resolution of the measuring equipment. There might also be physical effects that are not taken into account by the theoretical description, such as the possible presence of hybridization or the formation of electron-hole pairs over the Fermi surface in metals. Also from the theoretical side broadening is present. A technical source of broadening arises from the fact that we evaluate the imaginary part of the Green's function just above the real axis, as has been explained in Eq. 2.21. Both in theory and experiment, crystal field

splitting of the S , L and J multiplet causes broadening within the resolution of the experiment. The relatively small crystal field splits the multiplets into different J_z components or linear combinations thereof. In this thesis we use density functional theory with dynamical mean field theory within the Hubbard I approximation (DFT+DMFT(HIA)). In principle, this can capture the crystal field effects. However, in practice for technical reasons (no proper formulation of the double counting for crystal field), no one has yet managed to include it properly. In the outlook in Sec. 3.7 this issue is described more detailed.

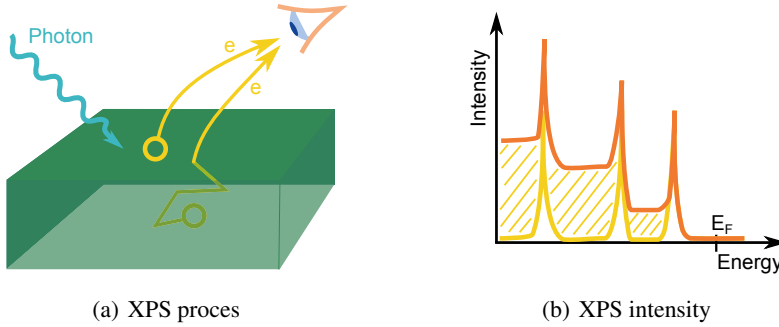


Figure 3.7. (a) Schematic view of an electron going directly to the detector and another one scattering before reaching the detector. (b) Schematic view of how the experiment (orange line) measures the true peaks (yellow). The shaded areas are due to electrons undergoing extra scatterings before the electron leaves the sample.

In the experimental spectra there is a significant increase of the spectrum when going further away from the Fermi level. At first sight, this seems strange, since one expects relatively sharp peaks belonging to the $4f$ multiplet and no spectral weight in between these peaks. The increment in spectral weight originates from scatterings of the emitted particle before leaving the sample. In this scattering process the particle (electron or photon) loses energy. The detector detects a lower energy (compared to the energy of a particle that leaves the sample without additional scatterings) and deduces from this that the particle originates from a lower lying state than is actually the case. With this effect, these scattered particles cause spectral weight at energies further away from the Fermi level than where they originate from. The finite intensity between the first and second peak is therefore due to electrons from the first multiplet that have scattered around in the sample before reaching the detector. The even more increased intensities observed in between the other multiplets arise from electrons originating from any multiplet up to the Fermi level, with various scatterings before reaching the detector. The scattering process and its influence on the spectral weight is schematically drawn in Fig. 3.7.

3.5.3 Multiplet structure

With the photoemission experiments one measures transitions from the Hund's rule ground state with f^n electrons and quantum numbers L , S and J to the excited state with f^{n-1} electrons and quantum numbers L' , S' and J' . The inverse photoemission experiments probe $f^n \rightarrow f^{n+1}$ transitions. Which of the final states are accessible from the Hund's rule ground state depends on the selection rules [5]. For XPS, where one electron is removed, $S - S' = \frac{1}{2}$. The maximal amount of angular momentum which can leave the system is $\pm l$, where l is the angular momentum quantum number of the shell where the electron is removed from. Therefore $|L - L'| \leq l$.

As an illustrative example, we consider the XPS spectrum of Nd that probes $f^3 \rightarrow f^2$ transitions. The Hund's rule ground state is denoted with the term symbol $^4I_{9/2}$. The possible final states can be found by determining all possible ways to arrange 2 electrons over the $-3 \leq m_l \leq 3$ and $m_s = \pm \frac{1}{2}$ orbitals. This is done in App. A and leads to the following multiplets: 1I_6 , $^3H_{4,5,6}$, 1G_4 , 1S_0 , $^3F_{2,3,4}$, 1D_2 and $^3P_{0,1,2}$. From these multiplets only $^3H_{4,5,6}$ and $^3F_{2,3,4}$ are compatible with the selection rules and can be found in the XPS spectrum. These states will be slightly split by crystal field effects, but the separation of the multiplet states is dominant [57].

A similar approach can be done for the BIS spectra, considering that adding one electron is the same as removing one hole. The relative intensity of these different multiplets can be calculated from the coefficients of fractional parentage, which is explained in Ref. [5] for XPS and Ref. [22] for BIS. The coefficients of fractional parentage are tabulated in Ref. [5] for XPS and Chapter 62, Table I of Ref. [40] for BIS. In our work the spectra are directly calculated from the imaginary part of the Green's function in the DFT+DMFT(HIA) approach.

3.6 Summary of Papers I and II

Paper I: Standard model of the rare earths, analyzed from the Hubbard I approximation

In the previous sections on the physical background of the various properties, I tried to give an intuitive view why the standard model of the lanthanides, that assumes a chemically inert $4f$ shell, works so well. Several attempts to apply *ab-initio* electronic structure calculations for real material-dependent properties of the REs, had variable success. The typical parameterizations of the exchange-correlation potential of DFT are inadequate to describe the localized $4f$ electrons. Theories like LDA+U [4], self-interaction correction (SIC) [81], orbital polarization [30] and the $4f$ -in-the-core approach [88] have been tested on selected properties, and sometimes with great success. However, these methods are not able to describe a wide range of properties within

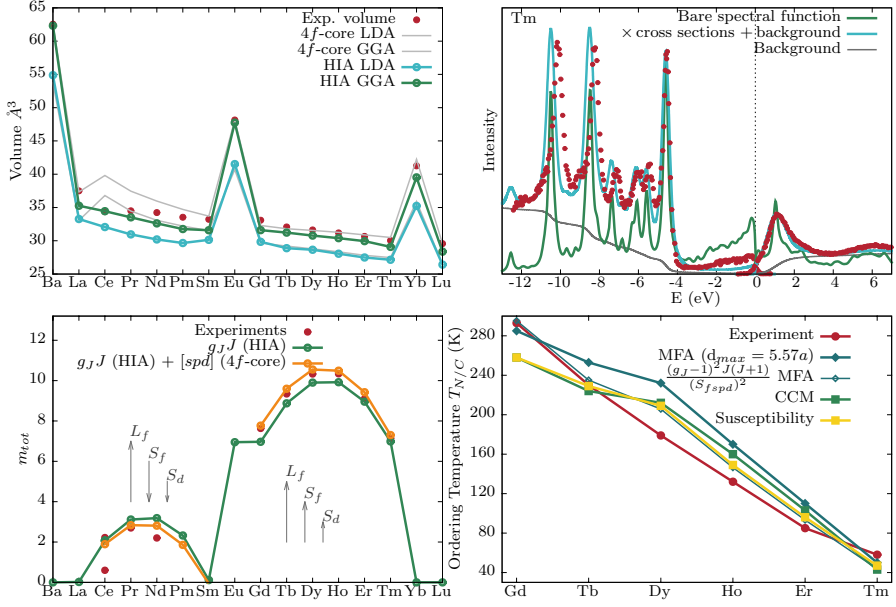


Figure 3.8. Summary of some results from Paper I. Top left: equilibrium volumes. Top right: valence band spectra of Tm. Bottom left: moments, with an illustration of the coupling between the spin and orbital moments of the f and d electrons as inset. Bottom right: ordering temperatures. All experimental values [38, 51, 39, 28, 57] are shown in red. More details can be found in Paper I.

one approach. The HIA is compatible with the standard model of the lanthanides. Therefore it is a very promising method to describe the electronic structure of the REs. This is exactly what we show in Paper I, with the elemental RE metals as testing ground. We find that the theoretical equilibrium volumes and bulk moduli are in good agreement with experiment. In the top left panel of Fig. 3.8 our results on the equilibrium volume are shown. The HIA captures the difference in volume between the divalent and trivalent elements and the lanthanide contraction. For the early REs we find a slight overestimation of the lanthanide contraction, but in general the trend is captured very well. Clearly the GGA functional gives the best quantitative agreement, since it performs best to describe the itinerant $[spd]$ electrons. Moreover HIA predicts magnetic ground states that are very similar to the Russell-Saunders coupled ground state that is expected for the REs, as can be seen in the bottom left panel of Fig. 3.8. This may seem as expected, since both Hund's rules and HIA are atomic-like theories. However, it is rewarding that HIA predicts the correct magnetic ground state, without making any assumption on the mechanism of coupling angular momentum states. The top right panel of Fig. 3.8 shows the (inverse) photoemission spectrum of Tm. This is only one example, but the photoemission spectra of all elemental RE metals agree

very well with measured data. All multiplet features are captured and only a small discrepancy is found in their energy positions. Additionally we use the $4f$ -in-the-core approach to calculate the interatomic exchange parameters of an effective spin Hamiltonian. We use these exchange parameters to calculate the ordering temperatures for the heavy REs, as displayed in the bottom right panel of Fig. 3.8. The calculated ordering temperatures agree within 20% with measured data and capture the trend of decreasing ordering temperature across the series. Additionally, the magnon dispersion of Gd can be used to show the accuracy of the calculated exchange parameters. We think that the HIA is, among the available state-of-the-art methods, the most promising one to investigate the elemental REs or RE containing materials.

Paper II: Stacking fault energetics of α - and γ -cerium investigated with ab initio calculations

Cerium has a very interesting phase diagram, see Fig. 3.9. At zero pressure and low temperature, Ce forms a low-volume fcc structure (α -phase). With increasing temperature a transition to the β -phase which has a dhcp structure, occurs. This dhcp region is rather small, and around room temperature Ce undergoes a new transition to the high-volume fcc structure (γ -phase). With moderately increased pressure the dhcp phase disappears, and the low-volume α -phase changes directly to the high volume γ -phase with increasing temperature [99]. Cycling

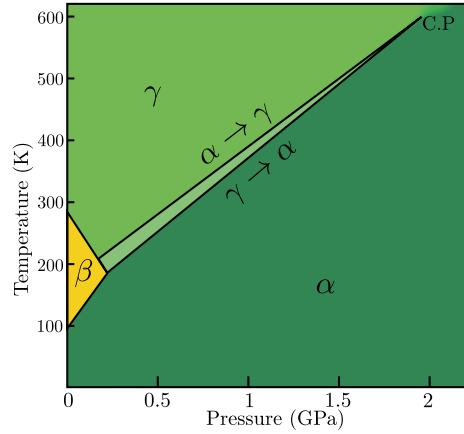


Figure 3.9. Phase diagram of Ce, data taken from Paper II.

between the α and γ phase shows a hysteresis effect, where the $\gamma \rightarrow \alpha$ transition occurs at a slightly lower temperature or slightly higher pressure than the $\alpha \rightarrow \gamma$ transition [100]. In Ref. [73] the authors argue that repeated cycling would lead to dislocations. Several mechanical properties, such as hardening, plasticity and deformations have been related to stacking fault energies, *i.e.* the energy needed to introduce a wrong stacking in the order of the layers. This, together with the fact that fcc and dhcp structures are actually very similar except for a stacking fault (see Fig. 3.3), motivates a thorough study of stacking fault energies in Ce.

In Paper II we study the energy required for an intrinsic stacking fault, *i.e.* a missing layer in the perfect fcc stacking, using both the supercell approach and the axial interaction model. In the axial interaction model, the stacking fault energy is related to the energies of the different possible stacking orders. We find that the stacking fault energy for the γ -phase is much smaller than for the

α phase, which largely explains the hysteresis effect when cycling between the two phases. Due to the low stacking fault energy for the γ phase, it is very easy to introduce dislocations when going from $\gamma \rightarrow \alpha$. However, when returning from $\alpha \rightarrow \gamma$, it is hard to introduce dislocations and therefore the transition is delayed.

In this work the core of the calculations were done with plain DFT, since it is computationally less demanding than the DFT+DMFT approaches that are usually employed for Ce. The α phase was simulated with $4f$ electrons as part of the valence, which results in itinerant $4f$ electrons and a small equilibrium volume. The γ phase was simulated with the $4f$ electrons as part of the non-hybridizing core, which prevents the $4f$ electrons from contributing to the bonding and results in a bigger volume. The success of the Hubbard I approximation for describing the γ phase of Ce, as tested in Paper I, was used to confirm selected $4f$ -in-the-core results. Both methods show very similar stacking fault energies across the different volumes. DFT+DMFT with the spin-polarized T-matrix fluctuation exchange (SPTF) solver was used to validate the DFT calculations for the α phase. Here as well, the stacking fault energies with both approaches were very similar.

In Paper II we model the two phases separately with two different methods. Note that in this way one can not model the phase transition itself. The two separate stacking fault energy curves as a function of volume for the two phases do not represent the reality in the region where the two phases coexists. However, to model the stacking fault energies for the two phases separately gives theoretical insight, since this allows to describe the hysteresis effects. DFT+DMFT with a quantum Monte-Carlo (QMC) solver could be used to model the phase transition itself and would give a unified curve for both phases.

3.7 Outlook

For both projects mentioned above, it would be interesting to address the cohesive properties in the magnetically ordered phases. The elemental REs have an interesting magnetic phase diagram and the magnetic properties might influence the bonding properties. As mentioned in Paper I and above, both the bonding properties and the stacking fault energies are rather sensitive quantities and mainly determined by the $[spd]$ electrons. In DFT+DMFT a correct description of the $[spd]$ electrons requires a charge self-consistent calculation. However, for charge self-consistent magnetic DFT+DMFT calculations, the issue of the double counting, which was briefly mentioned in Sec. 2.3.5, becomes a problem. When combining spin-polarized DFT with DMFT the double counting term should correct for the f - f exchange that is taken into account in both the DFT part and in U . However, it should not correct for the f - d exchange, since this is not accounted for by U . The problem is that one

cannot disentangle the two, and therefore any choice becomes an unjustified guess. This issue of the spin-polarized double counting needs to be addressed and methodological advances for magnetic calculations are needed. This also holds for other quantities related to magnetism such as the magnetic anisotropy energy and related quantities. These quantities depend on a subtle balance between the crystal field effects and the spin-orbit coupling. A thorough study is needed to investigate to what extent crystal field effects in the REs are correctly described with the HIA.

For the phase transition in Ce, related to Paper II it would be interesting to use methods that can describe both the α and the γ phase. For this the approximate HIA solver in the DFT+DMFT cycle is not sufficient and more sophisticated (and costly) solvers such as the quantum Monte Carlo solver are needed. However, a very accurate calculation of the total energy is required for a proper assessment of the small energy differences between the different structures.

4. Microscopic configuration after ultrafast magnetization dynamics

One of the principal objects of theoretical research is to find the point of view from which the subject appears in the greatest simplicity.

— Josiah Willard Gibbs (1994)

THIS chapter of my thesis is related to the field of ultrafast magnetization dynamics. The kickoff of this field was given by Beaurepaire *et al.* [12] in 1996 by probing for the first time the magnetization dynamics in Ni on the femtosecond time scale. The pump-probe experiments revealed a new type of dynamics: an ultrafast decrease of magnetization following a laser pulse. The experimental results were described by modeling the material through three interacting reservoirs, belonging to the electron system, the spin system and the lattice system. This phenomenological model is referred to as the three temperature model. Since this first discovery of ultrafast demagnetization, several other experiments have followed and supported the findings of Beaurepaire *et al.* [12]. The field of ultrafast magnetization dynamics was further investigated in various systems and new insights were obtained. Some examples are the experimental observation of spin transport during ultrafast magnetization dynamics in $[\text{Co-Pt}]_n$ multilayers [63], the spin injection from Fe to Au on the femtosecond timescale [68] and the discovery of ultrafast magnetization *increase* in Fe in a Ni/Ru/Fe trilayer [86].

During all these years of research, a leading question has been: what is the underlying mechanism behind the ultrafast magnetization dynamics? In particular, where does the angular momentum related to the electron spins go? In Fe, Ni and Co, the most commonly used materials in magnetization dynamics experiments, the orbital moment is quenched and the magnetization is mainly attributed to the electron spins. Several possible mechanisms for ultrafast demagnetization have been proposed over the last years and they are nicely summarized in Ref. [49]. All mechanisms consider in one way or the other an angular-momentum transfer from the electron spins to somewhere else. A direct contribution of the photon angular momentum in the polarized laser beam on the demagnetization was found to be very small by experiments in 2007 [23]. On the other hand it is of significant importance in, for example, the inverse Faraday effect. Another possibility to carry away angular momentum is given by the photons that are emitted during the ultrafast demagnetization. However it is generally believed that this effect is very small.

Koopmans *et al.* [55] suggested a model of demagnetization driven by spin-phonon coupling, where the energy of the demagnetization comes from the electrons, but the dissipative channel for the angular momentum is given by the lattice. Spin-flips occur due to electron-phonon scattering. Note that this mechanism relies on spin-orbit coupling. Another option to decrease the total magnetization is given by transferring spin angular momentum to orbital angular momentum through electron-electron scattering. The decrease of magnetization is then achieved, since the moment associated to the spin angular momentum contains the gyromagnetic ratio $g \approx 2$. The transfer of spin to orbital angular momentum could also happen via electron-magnon scattering. Battiato *et al.* [9] suggested that the ultrafast demagnetization and also the ultrafast increase of magnetization [86] are driven by superdiffusive transport of spin. In this model the change of magnetization arises from the difference in the mobility (velocity and lifetime) of the majority and minority spin electrons that are excited by the laser pulse. This difference causes a net spin transport. The model of superdiffusive spin transport was developed for metals, such as Ni and Fe, but later extended to semiconductors [10]. Many of the above mentioned mechanisms are theoretically possible, but the question is to what extent they contribute to the demagnetization process. This depends on the specific case, the material and the geometry of the sample. It is becoming more common to think of a coexistence of effects [95, 93].

The above mentioned experiments were done on transition metals, where the magnetism arises from the d electrons. However, ultrafast magnetization decrease has also been measured in Gd [19]. As mentioned in Chapter 3, the magnetism in the REs arises from the localized $4f$ electrons. This moment exchange-couples to itinerant $[6s6p5d]$ valence electrons inducing a moment of about $0.6\mu_B$. The fact that the magnetism arises from two very different types of electrons that only weakly interact adds complexity to how to describe the magnetization dynamics.

However, even without this extra complexity, it is already very difficult to find a good correspondence between theory and experiment. The field of ultrafast magnetization dynamics deals with strongly out-of-equilibrium situations. Theoretically we can not treat this very complex out-of-equilibrium physics directly and assumptions and simplifications have to be made. In order not to over simplify the physics, but still be able to establish a connection between fundamental microscopic quantities and experimentally observed quantities, we move to the picosecond time scale in Paper III. This is the timescale when the ultrafast magnetization dynamics process has ended¹. We show that in this time scale a partial thermal equilibrium is reached in which we can connect theory and experiment. In the following I will present shortly the idea

¹The exact times scales depend on several factors such as the material under investigation. For simplicity we stick to the nomenclature of Paper III and name the sub picosecond time scale the time during which the ultrafast magnetization dynamics take place. With the picosecond time scale we intend the time after the ultrafast process.

of the work we have done in Paper III. This paper involves many different fields of physics, arguments, and inferences, which makes it quite complicated to follow the main idea. I therefore have chosen to give an overview of this paper to illustrate the fundamental line of thoughts. As a result this chapter is structured in a slightly different way than the previous chapter and starts with a summary of Paper III. After that I will give some more details on the magneto-optical effects that are used as experimental evidence for ultrafast magnetization dynamics. In the end I will present some preliminary results related to the commonly used assumption that the magnetic asymmetry measured in experiments is proportional to the magnetization.

4.1 Summary of Paper III: Microscopic configuration after ultrafast magnetization dynamics

Although the underlying mechanism of the ultrafast magnetization dynamics is an extremely interesting topic, it has been difficult to make a connection between measured quantities and microscopic properties. Therefore in Paper III, we try to fill this gap by focussing on the microscopic electronic state directly after the ultrafast process. As mentioned above, this is needed to avoid the strong out-of-equilibrium situation during the process itself. After the ultrafast dynamics, the system attains a partial thermal equilibrium, which we can address with known theoretical tools. This enables us to make a connection between theory and experiment. The work in Paper III was inspired by various experiments on ultrafast magnetization dynamics and in particular by the experiments in Refs. [86, 93] on Fe and Ni. In these works the authors show that ferromagnetic Fe can undergo both an ultrafast decrease and increase of magnetization (Fig. 4.1(a)). These processes result in two qualitatively different experimentally observed transverse magneto-optical Kerr effect (T-MOKE) spectra at the $3p$ absorption edge of Fe (Fig. 4.1(d)). We were wondering whether this difference in the T-MOKE spectra, could be explained from the magnetic state just after the ultrafast process. In Paper III we propose a model to predict the microscopic electronic and magnetic configuration after ultrafast magnetization dynamics and we indeed support the difference in the T-MOKE spectra.

The main question of this work is: What is the magnetic configuration after ultrafast increased magnetization or after an ultrafast demagnetization on a microscopic level? To address this question, we identify and classify all possible microscopic states. The first step is to consider that in the picosecond time scale one can already describe the system with well defined atomic magnetic moments [6]. Examples of microstates classified with respect to their magnetic moments are reported in Fig. 4.1(b), for both the magnetized and demagnetized cases. Note that we only show here the magnetic part of the configuration, as illustrated by the atomic magnetic moments, and not the elec-

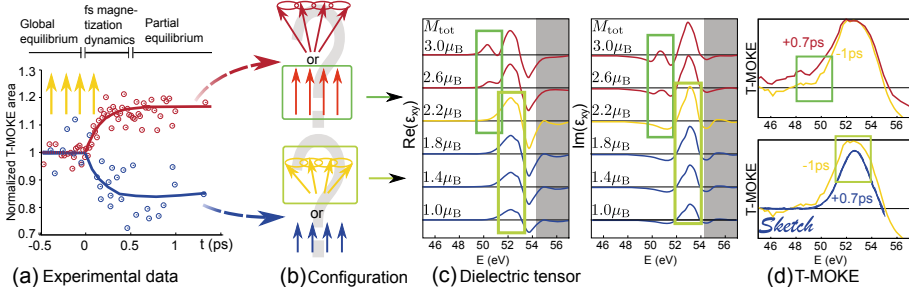


Figure 4.1. Illustration of the main idea of the work in Paper III. (a). The experiments showing the ultrafast increase (red) and decrease (blue) of the T-MOKE area in Fe as reported in Ref. [93]. This T-MOKE area is related to the magnetization. (b). Our identification of the microscopic states after the ultrafast dynamics. (c). The off-diagonal components of the dielectric tensor for the proposed configurations for several magnetizations M_{tot} . (d). The T-MOKE spectrum after an ultrafast increase of magnetization as reported in Ref. [93] (top, red) and a sketch of the T-MOKE after an ultrafast decrease of magnetization (bottom, blue), compared to the T-MOKE before the laser excitation (yellow).

tronic part. For the demagnetized case (blue line in panel (a)), one can imagine that the magnitude of the atomic spins would decrease, as illustrated by the blue arrows in panel (b). Another option would be that the atomic moments retain their length, but tilt in various directions, which effectively decreases the total magnetization (illustrated by the yellow tilted arrows). Obviously, intermediate states are also possible. Similarly for increased magnetization, one could imagine that the magnitude of the individual atomic magnetic moments increases (illustrated by the straight red arrows in panel (b)). In case of tilted moments, this increase must be even larger (illustrated by the tilted dark red arrows in panel (b)).

In our model we integrate out the electronic degrees of freedom, which allows us to identify the configurations in the green boxes (Fig. 4.1(b)) as the most probable ones. For the demagnetized case, we predict that the atomic magnetic moments retain their lengths, but magnon excitations cause a decrease of the total magnetic moment. In the case of increased magnetization instead, we predict an increase of the magnitude of the individual atomic magnetic moments. These predictions are obtained through statistical arguments, which are presented in Paper III and are summarized at the end of this paragraph.

Starting from the magnetic configurations, we can calculate the dielectric tensor. The T-MOKE spectrum measured in the experiments is proportional to the off-diagonal element of the dielectric tensor, if this element is small. Both these quantities are illustrated in Fig. 4.1(c) and (d). For the increased magnetization case, denoted by the red lines compared to yellow (equilibrium)

lines in Fig. 4.1(c) and (d), we see that a shoulder develops just below the main peak. The main peak itself retains its height. We recognize the same behavior both in the off-diagonal element of the dielectric tensor, as well as in the T-MOKE spectrum. A quite different behavior is seen for the demagnetized case, where the main peak in the off-diagonal component of the dielectric tensor decreases proportionally to the magnetic moment. Also the height of main peak in the experimentally measured asymmetry decreases with decreasing moment.

In Paper III one can find all details on the foundation of our model leading to the predicted configurations. Since many different arguments and corollaries come together in a complex way, I tried to outline them in the scheme in Fig. 4.2. We describe how we characterize different time scales (illustrated in panel (a) of Fig. 4.1), and how this allows us to consider a partial thermal equilibrium just after the ultrafast magnetization dynamics. The “partial” attribute refers to the system having a magnetization that is either bigger or

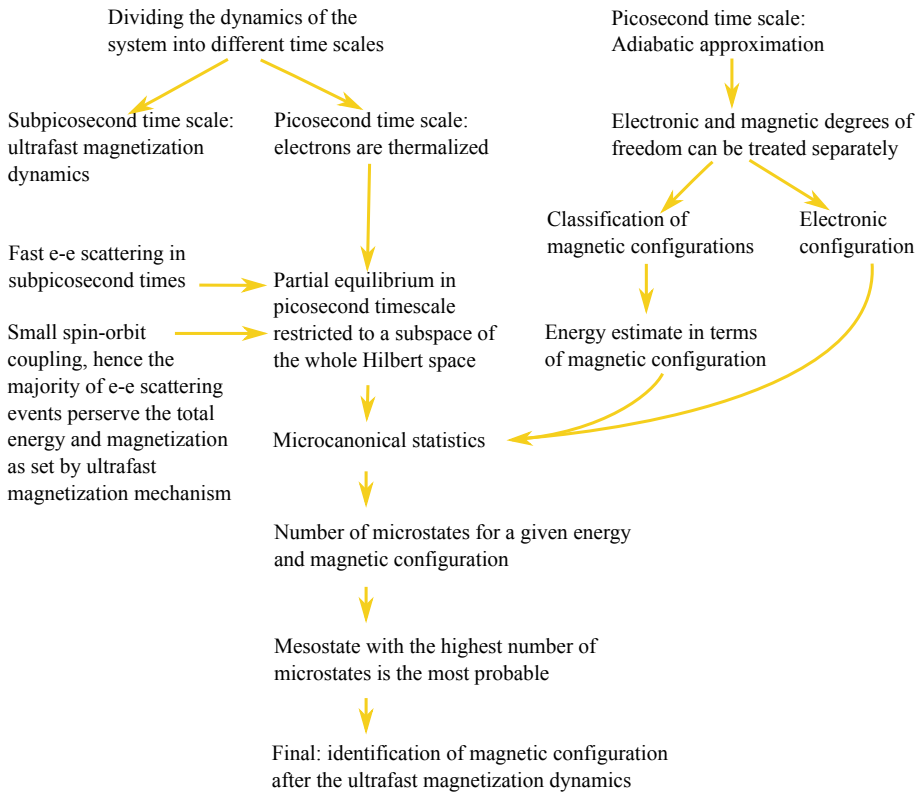


Figure 4.2. Outline of arguments, corollaries, assumptions and intermediate results of Paper III. These apply to $3d$ electrons in Fe and Ni, but are likely to be generalized to other systems as well.

smaller than the equilibrium magnetization. This partial equilibrium allows us to use statistical arguments to predict the microscopic configuration. The adiabatic approximation [6] allows us to separate the magnetic and electronic degrees of freedom and to define the microstates by their magnetic and electronic configuration. For each total energy and total magnetic moment, we group the microstates according to the magnetic configuration, *i.e.*, the length and orientation of the atomic magnetic moments. These groups of microstates with the same magnetic configuration, but different electronic configurations, we call mesostates. Then we compute the number of microstates within one mesostate to identify the most probable mesostate. It turns out that the number of microstates depends on the energy of the given magnetic configuration of the mesostate for the lowest possible electronic configuration. Hence, we calculate the energy of the magnetic configuration of the mesostates and identify the most probable mesostate for each scenario. As mentioned above, this results in collinear atomic magnetic moments with increased magnitude for the case with increased magnetization, and in gradually tilted atomic magnetic moments with equilibrium magnitude after ultrafast demagnetization. The model that we propose determines the magnetic configuration just after the ultrafast magnetization dynamics, and makes it possible to compare the measured data to results that are calculated from microscopic properties. Hence we can calculate the dielectric response around the $3p$ absorption edge of Fe for the predicted configurations and compare this to the experimentally measured asymmetry in the T-MOKE spectra. As is shown in panel (d) of Fig. 4.1, the T-MOKE spectrum of the increased magnetization case is qualitatively different from the decreased magnetization case. The dielectric tensor, calculated from the states predicted in our model, shows exactly the same qualitative difference, as is shown in panel (c) of Fig. 4.1. Hence our model can explain the qualitatively different behavior in the two cases.

In the next section we will briefly discuss the different MOKE experiments and the experimental setup as used in for example Refs. [86, 93, 56]. Thereafter, we will discuss the dielectric tensor and its relation to the MOKE properties briefly, because it is here where theory and experiment meet each other.

4.2 Magneto-optics

Magneto-optical effects were first discovered in the 19th century when Faraday found that the polarization vector of linearly polarized light rotates when the light travels through a sample with a magnetization parallel to the propagation direction of the light [31]. Since this discovery also other magneto optical effects were discovered, such as the Kerr effect. In this thesis we discuss the magneto-optical Kerr effect (MOKE), which describes how light changes upon reflecting from a magnetic surface. The review of H. Ebert [29] has been very helpful for this section.

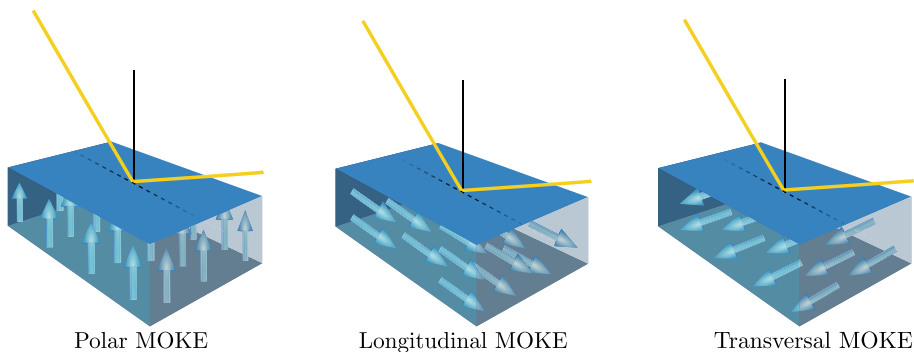


Figure 4.3. Different MOKE setups

MOKE can be measured in different setups. The setups are categorized according to the relative orientation of the light beam and the magnetization in the sample, as shown in Fig. 4.3. In addition to the choice of setup, also the angle of incidence and the polarization of the light beam matters. In our work in Paper III we compare the dielectric tensor to the magnetic asymmetry as measured in the transversal MOKE (T-MOKE) setup. This corresponds, for example, to the experimental setup in Refs. [86, 93]. In Sec. 4.2.1 we briefly describe these experiments. In Sec. 4.2.2 we move to the theoretical side and we briefly discuss the dielectric tensor and its properties. The former can be related to the magnetic asymmetry, as is shown in Sec. 4.2.3.

4.2.1 Experiments

The above mentioned magnetic asymmetry is the quantity that is frequently measured in experiments to probe the ultrafast magnetization dynamics. Typical experiments, like *e.g.* those carried out in Refs. [86, 93, 56] on Fe and Ni are so-called pump-probe experiments. In these experiments a femtosecond pulsed laser beam is split into two parts. A small part is directed at the sample to excite (pump) it and induce the magnetization dynamics. The bigger part is led through a capillary filled with gas. Due to high harmonic generation (HHG) the gas emits high harmonics of the laser beam, which results in short laser pulses with energies around the $3p$ absorption edges of Fe and Ni. The duration of the pulses is less than 10 fs. With different time delays the pump and the probe pulses hit the sample. This time delay is regulated by changing the length of the path of either the pump or the probe pulses. The probe pulse is split by either the grating sample or by a separate diffraction grating, to measure the intensity of the reflected light at the different energies resulting from the HHG process. Magnets around the sample change the magnetization direction and the reflectivity of the probe beam is measured for both directions. This process is repeated several times to obtain a large amount of data and then reduce the experimental noise.

4.2.2 Dielectric tensor

The interaction between light (electromagnetic radiation) and a crystal can be described by the dielectric tensor (or the related electric susceptibility) that relates the electric field and the polarization field in Maxwell's equations. The magneto-optical properties can therefore be derived from the energy dependent dielectric tensor $\epsilon(E)$. The form of this tensor is dictated by the symmetry of the system, which depends, amongst others, on the magnetization direction. For a cubic system, with a finite magnetization in the \hat{z} -direction, only five components of the dielectric tensor have a finite value. The xx and yy -component are the same, for symmetry reasons. The zz -component is slightly different, since the magnetic moment is in the \hat{z} -direction. Only two of the off-diagonal components are non-zero. This results in a dielectric tensor of the following form

$$\epsilon(E) = \begin{pmatrix} \epsilon_{xx}(E) & \epsilon_{xy}(E) & 0 \\ -\epsilon_{xy}(E) & \epsilon_{xx}(E) & 0 \\ 0 & 0 & \epsilon_{zz}(E) \end{pmatrix}, \quad (4.1)$$

where $\epsilon_{xy}(E)$ changes sign upon reversing the direction of the magnetic field. Note also that the change in symmetry due to magnetization, only happens due to the spin-orbit coupling. Therefore spin-orbit coupling is crucial for the magneto-optical effects.

The dielectric tensor can be obtained from band-structure calculations in combination with linear response theory using the Kubo formalism [83]. This formalism relates the dielectric tensor to transitions from occupied to unoccupied states. To get a feeling of how the dielectric tensor looks like, we show the density of states and some parts of the dielectric tensor for Fe in Fig. 4.4. In this thesis we are interested in the magneto optical effects around the $3p$ absorption edge of Fe and Ni. We therefore consider, as an example, Fe around this energy, *i.e.* the interval 50-60 eV. The upper row displays the density of states and several parts of the dielectric tensor in case no magnetization is present. The bottom row displays the same quantities for equilibrium magnetization in Fe along the \hat{z} -direction. For zero magnetization, the diagonal components of the dielectric tensor have a finite value and are all the same, see top middle panel of Fig. 4.4. The *spin-dependent* off-diagonal components also have a finite value, but the majority and minority spins cancel each other, see top rightmost panel of Fig. 4.4. This gives, for zero magnetization, a purely diagonal dielectric tensor. It is interesting to compare the density of states (leftmost panels in Fig. 4.4) to the dielectric tensor (rightmost panels in Fig. 4.4) for this case. For zero magnetization, the two peaks in the density of states due to the core levels are well defined and clearly separated. This means that the dielectric tensor for this case bears a strong resemblance with the density of states just above the Fermi level. One can see that the dielectric

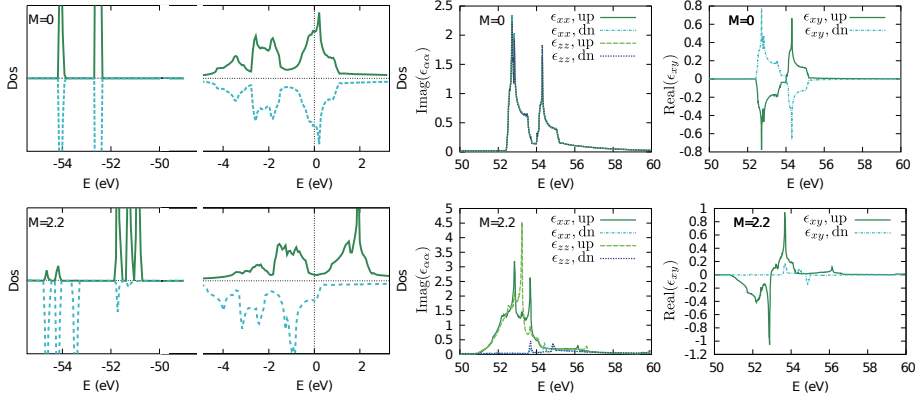


Figure 4.4. Density of states (left) and dielectric tensor (middle and right) of Fe. Top figures are for zero magnetization, bottom figures for equilibrium magnetization.

tensor probes somehow transitions from the $3p$ core level to the unoccupied states in the valence.

For a finite magnetization in the \hat{z} -direction, the zz -component is different from the xx -component. For the off-diagonal elements, majority (down) and minority (up) spins do not cancel anymore. One can see that transitions for the majority spin electrons are less probable than those for the minority spin electrons, since, just above the Fermi level, the density of states of the majority spin electrons is much smaller than that of the minority spin electrons, see bottom panels of Fig. 4.4.

The dielectric tensor can be used to calculate the magneto-optical effects. In the next section we focus on the magnetic asymmetry in the T-MOKE setup, since we compare our theoretical results of the dielectric tensor to the magnetic asymmetry measured in ultrafast magnetization dynamics experiments [86, 93].

4.2.3 Relation asymmetry and dielectric tensor

The propagation of light in a medium is described by the Maxwell equations together with some material relationships that relate the displacement field \mathbf{D} and the magnetizing field \mathbf{H} to the electric field \mathbf{E} and the magnetic field \mathbf{B} respectively, and Ohm's law [18]. In our case it is sufficient to use the material dependent dielectric tensor that relates the electric displacement to the electric field. Or equivalently the conductivity tensor that relates the current density to the electric field [18]. The Maxwell equations, the material relationships and Ohm's law can be combined into the Fresnel equations [18]. With the latter and the boundary conditions, *i.e.* the continuity requirements for the Maxwell equations, the MOKE spectra can be calculated. We are especially interested in the magnetic asymmetry in the T-MOKE setup. This is given by the dif-

ference between the reflection of the (p polarized) beam from a sample with the magnetization in the $\hat{\mathbf{z}}$ -direction (R^+) and in the $-\hat{\mathbf{z}}$ -direction (R^-), normalized by the sum. For a single element layer and for a small off-diagonal component $\epsilon_{xy}(E)$ of the dielectric tensor, the magnetic asymmetry is proportional to $\epsilon_{xy}(E)$ itself [18, 65]:

$$A(E) = \frac{R^+(E) - R^-(E)}{R^+(E) + R^-(E)} \approx \text{Re} \left(\frac{2\epsilon_0 \epsilon_{xy}(E) \sin(2\phi)}{\epsilon_{xx}(E)^2 \cos^2(\phi) - \epsilon_0 \epsilon_{xx}(E) + \epsilon_0^2 \sin^2(\phi)} \right), \quad (4.2)$$

where ϵ_0 is the vacuum dielectric permittivity and ϕ the angle of incidence of the beam. For small moments, and hence small $\epsilon_{xy}(E)$, the asymmetry is proportional to both the real and imaginary part of $\epsilon_{xy}(E)$. Various works additionally assume that $\epsilon_{xy}(E)$ is proportional to the magnetization [65] and hence that the magnetic asymmetry is proportional to the magnetization. Or at least that the magnetic asymmetry increases when the magnetic moment increases. Therefore, they use the magnetic asymmetry to probe the magnetization of the sample. Instead of using the approximate solution in Eq. 4.2, the Fresnel equations can also be solved numerically [94, 98]. With this procedure one could check the validity of the approximations made for the above equation. This issue will be analyzed in more detail in the next section.

4.3 Is the magnetic asymmetry proportional to the sample magnetization?

In Paper III we predicted the microscopic state after the ultrafast magnetization dynamics has taken place. We managed to qualitatively explain the difference between the T-MOKE spectrum after ultrafast demagnetization and the spectrum after increase of magnetization. The development of the shoulder at lower energies in the latter case is explained by our model, as well as the shape conserving decrease of the peak in the former case. In this section I would like to focus on some preliminary results on the quantitative relation between the magnetic asymmetry and the magnetization of the sample. We investigate the proportionality often assumed in experiments: $A(E) \propto M$. This ongoing work is in collaboration with the Molecular and Condensed Matter Physics group in Uppsala and a preliminary draft is given in Paper IV.

4.3.1 Before the laser pulse: equilibrium situation

Before turning our attention to the relation between the magnetic asymmetry and the magnetization, we investigate the correspondence between the theoretically calculated magnetic asymmetry and the experimentally measured

one. The dielectric tensor for the equilibrium state can be obtained using DFT calculations as mentioned in Sec. 4.2.2. From this dielectric tensor we can numerically solve the Fresnel equations [94, 98] to obtain the magnetic asymmetry for a specific geometry. Before comparing the theoretically calculated magnetic asymmetry to the experimental asymmetry, let us emphasize that the theoretical calculations are strongly simplified with respect to the range of effects affecting a complex experiment. The effect of these simplifications is not yet clear, but it would be very interesting to investigate it. Examples of discrepancies between theory and experiment are

Bulk versus finite slab: The dielectric tensor is calculated for bulk material.

This means that the finite size of the slab enters only through the Fresnel equations. Reconstruction near the surface or any surface roughness are not taken into account. Neither is the change in the electronic structure of surface states compared to bulk states taken into account.

Impurities: Impurities that might be present in the sample are not taken into account in theory.

Core hole effects: We calculate the dielectric tensor with the Kubo formula, that is based on excitations from occupied ($3p$ levels) to unoccupied (valence band) states. We neglect in this case the presence of a “core-hole” that is left around the $3p$ levels after the excitation. The main effect of taking into account a core-hole is probably a shift along the energy axis to deeper energies of the dielectric tensor. This shift is material and level dependent.

Strain in the sample: Since the samples are usually quite thin and are grown on some substrate, strain may occur and the lattice parameter may vary across the layer.

Substrate and capping layer: The optical properties of the substrate on which the sample is grown or the capping layer of the sample are not taken into account.

Born-Oppenheimer approximation: In the DFT calculations the nuclei are treated as fixed. Electron-phonon coupling is therefore not taken into account. We expect the influence of lattice vibrations in Fe or Ni to be small and mainly a tiny broadening of the spectrum.

Correlation effects: The DFT treatment of Fe and Ni is for some quantities not adequate. The $3d$ bandwidth and the spin splitting are slightly overestimated by LDA/GGA.

Despite all these simplifications, the theoretical asymmetry for a 100nm slab of Ni is found to agree qualitatively well with the experimental asymmetry, see Fig. 4.5. For low energies, the experimental asymmetry is found to be negative and becomes more negative towards the absorption edge. In the absorption edge the asymmetry is positive and after the edge it is close to zero. We find these features also in theory. We found only two quantitative differences. The first one is a shift of the features towards lower energies, which can most probably be explained by the effect of the core hole. The second disagreement

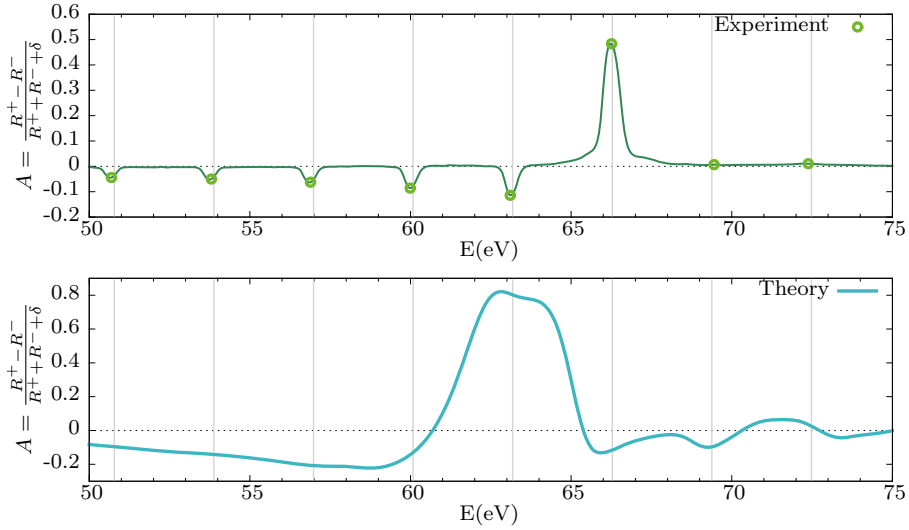


Figure 4.5. Magnetic asymmetry Ni (100 nm). Upper panel: asymmetry measured with T-MOKE on 100 nm Ni as described in Sec. 4.2.1. The grey lines denote the energy positions of the high harmonics and the green dots denote therefore the values of the asymmetry. Lower panel: asymmetry calculated by solving the Fresnel equations for a 100 nm layer of Ni with an *ab initio* calculated bulk dielectric tensor. Note that, in the upper panel only the green dots are relevant when comparing experiment to theory.

is that the theoretical asymmetry is found to be about 1.5 times larger than the experimentally measured one (the y-axes in Fig. 4.5 differ by a factor 1.5).

4.3.2 After the laser pulse: recovering the equilibrium magnetization

To investigate the relation between the asymmetry and the magnetization, we focus on the process of recovery of the magnetization after the ultrafast demagnetization. We focus on this process and not on the process of ultrafast demagnetization itself, since the latter is governed by strongly out-of-equilibrium physics and too complicated to describe for now. Moreover, in Paper III we already investigated the microscopic state of the material just after the ultrafast magnetization dynamics has taken place, and hence we can build on those results. During the process of recovering the equilibrium magnetization, the system can be treated as quasistatic with a time-dependent macroscopic magnetization $M(t)$ and energy $E(t)$. This allows us to examine the relation between the asymmetry and the magnetization.

In Paper III we identified the microscopic magnetic configuration after ultrafast demagnetization as a state with gradually tilting moments. With this we mean that all atomic magnetic moments are tilted from the \hat{z} -axis with an

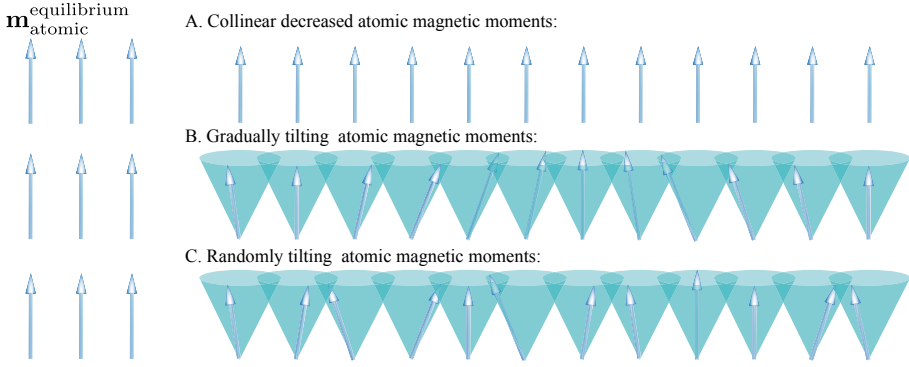


Figure 4.6. Illustration of some different ways to decrease the total magnetization. In panel A, the total magnetization is decrease by decreasing the length of all atomic magnetic moments individually. In panel B the atomic magnetic moments are gradually tilted, keeping their equilibrium length and a local ferromagnetic electronic structure. In panel C the atomic magnetic moments also retain their equilibrium length, but are tilted randomly and therefore do not have a local ferromagnetic electronic structure.

approximate angle θ , in order to decrease the total moment by $\cos \theta$. The projection of the atomic moments in the xy -plane is such that the entire collection of atomic moments has no net magnetization in the \hat{x} or \hat{y} direction. Although the atomic magnetic moments point towards different directions, neighboring moments are still nearly collinear, since very long-wavelength spin waves are formed, as illustrated in panel B of Fig. 4.6. In the picosecond timescale the atomic magnetic moments slowly align again with the \hat{z} -axis. For the moment we focus on this type of microscopic state and we verify the assumption that the magnetic asymmetry is proportional to the magnetization. To this extent we will calculate the dielectric tensor and solve the Fresnel equations numerically [94, 98] to obtain the magnetic asymmetry. We use a collinear DFT calculation as starting point to calculate the dielectric response for gradually tilted moments. First the dielectric tensor was calculated for atomic magnetic moments with equilibrium lengths pointing in the \hat{z} -direction. To obtain the dielectric response for the gradually tilting moments, the dielectric matrix was tilted over an angle θ from the \hat{z} -axis and rotated over an angle ϕ around this axis. The variable ϕ is integrated from 0 to 2π in order to have no net magnetization in a direction other than \hat{z} . This procedure is explained and supported in Paper III and in particular in Appendix F.

As we stated before, the assumption that the magnetic asymmetry is proportional to the magnetic moment, or at least that it increases with increasing moment is adopted in various works that use the magnetic asymmetry to probe the magnetic moment. To verify this assumption, we can directly calculate the asymmetry as a function of the moment for the three configurations mentioned above, but it is also interesting to first look at the relation between the real and

imaginary parts of $\epsilon_{xy}(E)$, and the magnetization. Let us start with this. For the gradually tilting moments with varying θ this assumption is true. Indeed $\text{Re}[\epsilon_{xy}(E)]/\text{Re}[\epsilon_{xy0}(E)] = M/M_0$ and $\text{Im}[\epsilon_{xy}(E)]/\text{Im}[\epsilon_{xy0}(E)] = M/M_0$ for all energies, where the subscript 0 denotes the value at equilibrium magnetization. This is actually true by construction, due to the way we calculated the dielectric tensor for this case.

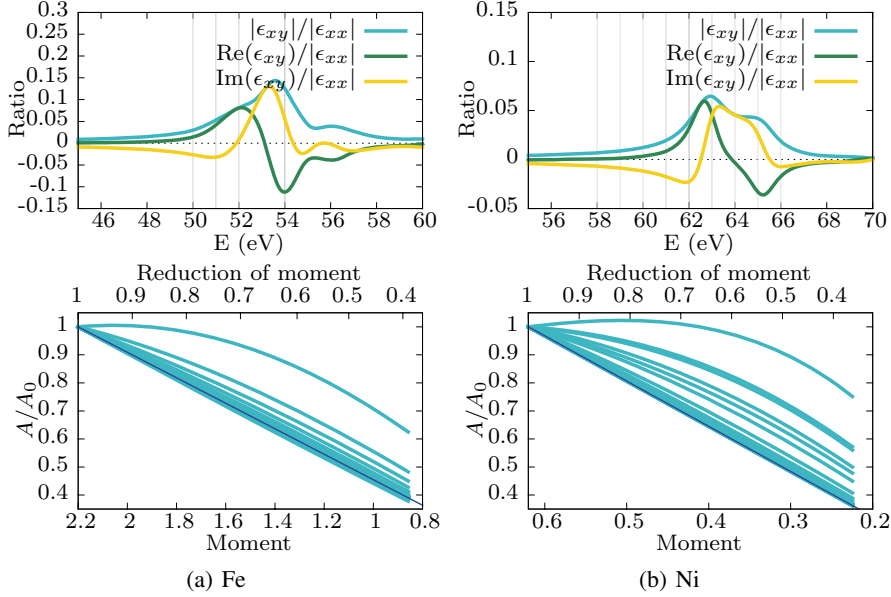


Figure 4.7. Non-linear relationship between magnetic asymmetry and magnetization for gradually tilting moments. Top row: Ratio between off-diagonal and diagonal components of the dielectric tensor. The grey lines denote the energies where the asymmetry as a function of the magnetization is most non-linear. Bottom row: Relation between the asymmetry at a specific energy and the magnetization. The different lines denote the different energies at which A/A_0 is evaluated. The behavior of the asymmetry was evaluated at all integer energies between 40-80 eV for Fe and between 50-80 eV for Ni. The dark blue line is a guide to the eye to illustrate the linear relation $A/A_0 = M/M_0$. The most non-linear lines for Fe belong to $E = 54, 52, 51$, and 50 eV. The most non-linear lines for Ni belong to $E = 62, 61, 63, 64, 65, 60, 59, 58$ and 66 eV

Secondly we can investigate the proportionality between the magnetic asymmetry and the magnetization. We check this for all energies, by calculating the asymmetry from the numerical solutions to the Fresnel equations. We find that, for gradually tilting moments, where θ decreases to recover the original magnetization, the approximate proportionality holds only for some energies, whereas for energies in the absorption edge the asymmetry is not linearly proportional to the magnetization. We show our results in Fig. 4.7. In the top row, the ratio between the off-diagonal and diagonal components of the di-

electric tensor for Fe (left) and Ni (right) is shown. To obtain the asymmetry, we solved the Fresnel equations numerically [94, 98] for a 100 nm layer of Fe and a 100 nm layer of Ni for the scenario of gradually tilting moments. In the bottom row of Fig. 4.7 we display the relation between the normalized asymmetry A/A_0 and the magnetic moment at several energies, calculated by solving the Fresnel equations [94, 98]. Especially close to the absorption edge, *i.e.* between 50-58 eV for Fe and between 58-68 eV for Ni, the off-diagonal component of the dielectric tensor is not very small as can be seen in the top row of Fig. 4.7. It is clear from our calculations that for energies in this range, the relationship between the magnetic asymmetry and the magnetization is non-linear.

In Paper III we identified microscopic states with gradually tilting moments as the state just after the ultrafast magnetization dynamics has taken place (panel B of Fig. 4.6). However, it is worth considering also a state where the atomic magnetic moments are not gradually tilted, preserving the local ferromagnetic electronic structure, but are tilted randomly instead. We illustrated this situation in panel C of Fig. 4.6. In this case the relation is expected to be non-linear as well. For randomly titled moments, the electronic structure is expected to change from the ferromagnetic case. This will influence the dielectric tensor, where we expect that $\epsilon_{xy}(E)$ is no longer proportional to the magnetization. This lead to the believe that the non-linearity in the asymmetry is probably even stronger than in the case of gradually tilted atomic magnetic moments. We are planning to investigate this scenario as well.

Finally, we would like to mention that also for the scenario with collinear decreased atomic magnetic moments (panel A in Fig. 4.6), the relation between the asymmetry and the magnetization is not linear. We calculated the dielectric response with a collinear constraint DFT calculation, where the atomic magnetic moments are constraint to a value smaller than the equilibrium value. We emphasize here that, for the collinearly decreased moments, the real and imaginary parts of the off-diagonal component of the dielectric tensor are not proportional to the magnetization. Around as well as in the absorption edge, the relation between $\text{Re}[\epsilon_{xy}(E)]$ and the magnetic moment is strongly non-linear. At some energies $\text{Re}[\epsilon_{xy}(E)]$ even increases with decreasing magnetization. Similar behavior is found for $\text{Im}[\epsilon_{xy}(E)]$. Also the magnetic asymmetry is not at all linearly proportional to the magnetization.

Although we can not establish a perfect quantitative agreement between the theoretical and experimental asymmetry, we can conclude that one should be careful with assuming a linear relationship between the magnetic asymmetry and the magnetization. In particular close to the absorption edge strong non-linearities are found in the theoretical calculations. In experiment a small difference is found in the $A(t)/A_0$ behavior for the different harmonics, as is shown in draft of Paper IV. If $A(E) \propto M$ for all energies, this would not be possible. The non-linear relationship between A and M could explain these

differences. However, the non-linearity found in theory seems to be much more pronounced than the differences found in experiment.

One could try to speculate about the relationship between the asymmetry and the magnetization during the process of ultrafast magnetization dynamics, *i.e.* in the sub picosecond timescale in the previously defined nomenclature. However, one should be extremely careful with this. During the ultrafast magnetization process, *i.e.* before the partial thermal equilibration, one can not use (quasi-) equilibrium physics to determine averages over the microscopic quantities to obtain the macroscopic quantities.

4.4 Outlook

Paper III was inspired by the experimental works in Refs. [86, 93] on Fe and Ni. In these materials the magnetism arises from the d electrons. It would be interesting to generalize the model to more complicated cases, as for instance Gd [19, 67]. In this case more care is required since the magnetism arises both from the itinerant $[spd]$ valence electrons and from the localized $4f$ electrons. The $[spd]$ and f spins interact only weakly and the question arises if to treat these moments always parallel, or only weakly coupled or as separate degrees of freedom [87]. Another question is whether the partial equilibration, on which our model is based, happens with two distinct constraints regarding the d and f magnetic moments. The most probable magnetic configurations are likely to be much more complicated than those proposed in Paper III for Fe. Also both Refs. [87] and [78] emphasize the difference in the electronic structure of the bulk and surface states in Gd. This implies that great care is required when comparing to surface sensitive experiments.

As mentioned in Sec. 4.3 it would be very helpful if we could make a quantitative comparison between the theoretical and experimental magnetic asymmetry. First of all the quantitative agreement for the equilibrium state should be improved and understood. To this extent it would be insightful to investigate the influences of the discrepancies between theory and experiment listed on page 61. After this quantitative agreement has been accomplished one could move on to the area of recovery of the equilibrium magnetization *after* the ultrafast magnetization dynamics and use the asymmetry to get a quantitative knowledge of the magnetization. The extremely brave could proceed to the even more uncertain territory of the ultrafast magnetization change itself and could speculate about the relation of the magnetic asymmetry to the magnetization during this process. A good quantitative agreement would support and quantify the use of the magnetic asymmetry to probe the magnetization of the sample.

With the numerical solution to the Fresnel equations, one can also investigate different geometries. One can study multilayer systems, and the influence of the capping and separation layers. This is however not so trivial, since the

shift in energy of the theoretical absorption edge is material dependent. When combining several materials, these should be aligned properly.

5. Analytic continuation

Nothing will work unless you do.

— Maya Angelou (1969)

IN this thesis, DFT+DMFT in the Hubbard I approximation is used and this method was implemented to calculate the spectral function directly on the real energy axis. However, for many other solvers of the impurity problem in DFT+DMFT the Green's function is only calculated as a function of imaginary time (τ) or imaginary frequencies, *i.e.* Matsubara frequencies $i\omega_n$. In order to compare to experimentally observable quantities, the Green's function (or a related quantity) is needed as a function of real frequencies ω , and this is where the problem of analytic continuation comes into play. One needs to continue the function known on the imaginary axis in the complex plane, to the real axis, as illustrated in Fig. 5.1. In Sec. 5.1 we introduce the problem of analytic continuation related to Green's functions and their corresponding spectral functions. In Sec. 5.2 we briefly describe the different methods that we use in our work in Papers V, VI and VII. We conclude with a summary of these works and some questions and challenges for the future.

5.1 Spectral functions

The quantity of interest is the spectral function $A(\omega)$ at real frequency ω . This quantity can be measured via photoemission experiments. The spectral function is related to the imaginary part of the single particle Green's function on the real axis and can be obtained from the Green's function at the Matsubara frequencies by

$$G(i\omega_n) = \int_{-\infty}^{\infty} d\omega \frac{1}{i\omega_n - \omega} A(\omega). \quad (5.1)$$

The Green's function in the above equation is a function of the fermionic Matsubara frequencies $i\omega_n = i\frac{(2n+1)\pi}{\beta}$, where β is the inverse temperature and n is an integer. The Green's function is analytic in the entire complex plane, except on the real axis. The spectral function is proportional to the discontinuity in the imaginary part of the Green's function on the real axis $A(\omega) = -\frac{1}{\pi} \text{Im}[G(\omega + i\delta^+)]$, where δ^+ indicates that we take the limit to zero

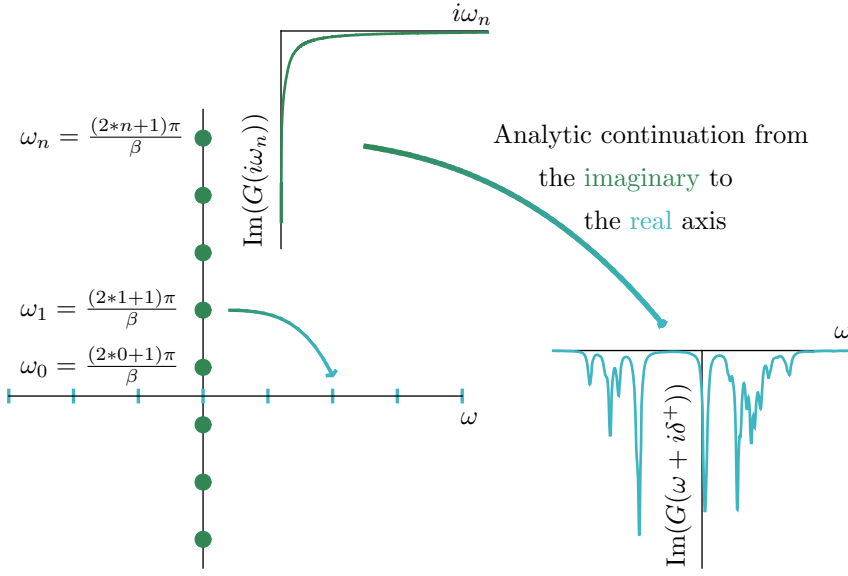


Figure 5.1. Schematic representation of the idea of analytic continuation

from above $\delta \rightarrow 0^+$. The Green's function is often decomposed in a non-interacting part and a part that contains the interactions, *i.e.* the self-energy, see Sec. 2.3. Thus instead of continuing the Green's function to the real axis, one can also continue the self-energy.

An example of a one-particle Green's function can be found in Sec. 2.3.2. In Eq. 2.15, the one-particle impurity Green's function of the single impurity Anderson model is given as a function of imaginary time. The single Anderson impurity model Hamiltonian is time independent and therefore the Green's function depends only on the time difference $\tau - \tau'$. To obtain the corresponding spectral function $A(\omega)$ one could first Fourier transform Eq. 2.15 to Matsubara frequencies and subsequently use Eq. 5.1 to obtain the spectral function. Alternatively one can also perform directly the analytic continuation from imaginary time to real frequencies:

$$G(\tau) = \int_{-\infty}^{\infty} d\omega \frac{e^{-\tau\omega}}{1 + e^{-\beta\omega}} A(\omega). \quad (5.2)$$

The previous discussion was focussed on one-particle Green's functions, as these are mainly considered in this thesis. In DMFT (and also in the Hubbard I approximation) the one-particle Green's function is a key quantity of the method and the calculations. In Paper I we calculated the one-particle spectral function of the elemental rare earth metals and compared it to the experimental valence band spectra. In Papers V and VII we tested the analytic continuation of one-particle Green's functions. However, dynamic two-particle quantities

have also received more and more attention in recent years. These two-particle Green's functions are used to calculate the linear response of a system to a small external perturbation. For example, a perturbation by a small electric field gives information about the optical conductivity and by a small magnetic field about the spin-susceptibility. In Paper VI, we therefore focussed on the analytic continuation of two-particle quantities.

As an example, the two-particle Green's function corresponding to the single impurity Anderson model in Sec. 2.3.2 is:

$$G(\tau_1, \tau_2, \tau_3, \tau_4) = -\langle \mathcal{T} \hat{c}_{\sigma_1}(\tau_1) \hat{c}_{\sigma_2}^\dagger(\tau_2) \hat{c}_{\sigma_3}(\tau_3) \hat{c}_{\sigma_4}^\dagger(\tau_4) \rangle. \quad (5.3)$$

Since the Hamiltonian is time independent, the Green's function actually depends on time differences and in the above equation one imaginary time variable can be eliminated. The four spin indices can be reduced to only two for symmetry reasons. After Fourier transforming the two-particle Green's function to imaginary frequencies, the three fermionic frequencies can be combined into one bosonic frequency $i\omega_n = i\frac{2n\pi}{\beta}$ and two fermionic frequencies. For one-frequency Green's functions (or susceptibilities), the three-frequency Green's function can be summed over the fermionic frequencies. The final one-frequency Green's function depends on a single bosonic frequency, see Ref. [84] for a thorough introduction to n -particle Green's functions.

Dynamical two-particle quantities have slightly different properties and symmetry relations, as described in Paper VI. The most important difference, compared to the one-particle spectral function, is that, along the real energy axis, the two-particle spectral function is odd, *i.e.* $A(\omega) = -A(-\omega)$. Contrary to the one-particle spectral function that is even, *i.e.* $A(\omega) = A(-\omega)$. Therefore, the asymptotic behavior for large n of the two-particle Green's function is ω_n^{-2} instead of the ω_n^{-1} behavior for one-particle Green's functions.

5.2 Methods of analytic continuation

The relation between the Green's function and the spectral function can be rewritten as a Fredholm integral of the first kind¹:

$$G(y) = \int K(y, x) A(x) dx. \quad (5.4)$$

Here $G(y)$ are the known data, $A(x)$ is the unknown model and $K(y, x)$ is the integral kernel that relates the model and the data. In relation to Eq. 5.1 the

¹The inversion of this Fredholm integral is not only relevant for the analytic continuation of Green's functions, but also in completely different areas of science. Such as in the inverse problem for electroencephalography (EEG) source localization, where the measured voltage potential on the scalp should reveal current sources inside the brain [35], or in electrocardiography (ECG) where on the body measured voltage potentials provide information about currents in the heart muscle [17].

data are given by the Green's function $G(i\omega_n)$, the model is the spectral function $A(\omega)$ and the Kernel takes the form $\frac{1}{i\omega_n - \omega}$. For the analytic continuation from imaginary time to real frequencies, the data and the Kernel are slightly different, as is also the case for the two-particle Green's functions. The model $A(x)$ can be always written in such a form that $A(x) \geq 0$. For the odd bosonic spectral function, this means for example that one obtains $\omega A(\omega) \geq 0$ and that the Kernel is adjusted accordingly.

In the complex case, the Fredholm integral is easily separated into real and imaginary parts, since the model $A(x)$ is real. This means that the integral can be split

$$\begin{aligned} \int [K_1(y, x) + iK_2(y, x)] A(x) dx &= G_1(y) + iG_2(y) \\ \Rightarrow \begin{cases} \int K_1(y, x) A(x) dx &= G_1(y) \\ \int K_2(y, x) A(x) dx &= G_2(y). \end{cases} \end{aligned} \quad (5.5)$$

where the subscript 1 denotes the real part and 2 the imaginary part. Although it looks as a simple equation, this is only apparent. Finding A given G is an inverse problem and usually very complicated. Especially in real world problems, where the data is known only on a finite number of points and only with finite precision, it is generally an ill-posed problem. If there exists an $A(x)$ that produces the data $G(y)$ there are usually infinitely many solutions, and it is not clear which one to pick. Even more worrying, generally there is no exact solution: there is no A that reproduces G . The aim of the analytic continuation methods is finding the best possible A .

There are several quite different approaches to find $A(\omega)$ given $G(i\omega_n)$. The methods that we use are illustrated in Fig. 5.2 and we will describe them in the following of this chapter. For the general idea, it is convenient to divide the methods into categories. One category of approaches consists in fitting a function to the known data $G(i\omega_n)$. In this $G(z)$ can be obtained anywhere in the complex plane and $A(\omega)$ is given by $-\frac{1}{\pi} \text{Im}[G(\omega + i\delta^+)]$ at a small distance δ from the real axis. In the Padé approximant method of analytic continuation, this approach is used with a fraction of polynomials as the fitting function. A brief explanation of this approach is given in Sec 5.2.1. We thoroughly investigate the capabilities of the Padé method for fermionic Green's functions and self-energies in Paper V. In Paper VI we test it for two-particle Green's functions. Note that in this approach one uses the fact that $A(\omega)$ is proportional to the imaginary part of the Green's function, when evaluating the fitting function close to the real axis. This proportionality is not assumed in the other methods, which are in this sense more general. That is, they are in principle applicable to each Fredholm equation of the first kind, regardless of the kernel or the relation between G and A .

A quite different category of approaches is based on random sampling methods to make guesses of $A(x)$. Eq. 5.4 is then used to obtain $G(y)$, which is compared to the known data set. According to an algorithm based on the

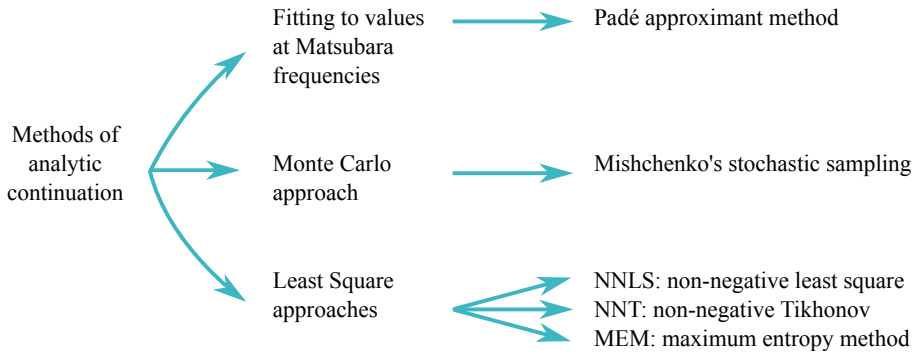


Figure 5.2. Illustration of the different categories of analytic continuation methods described in this chapter, for details see text.

difference between the calculated and known $G(y)$, the random changes in $A(x)$ are accepted or rejected in a Monte Carlo chain. The method of analytic continuation developed by Mishchenko *et al.* [70] is based on solving the Fredholm equation in such a way. We will discuss this method in Sec. 5.2.2. In Paper VII we implemented this method on a Graphics Processing Unit (GPU). In Paper VI we compared this method to other methods for the analytic continuation of bosonic Green's functions.

The last category that we will discuss includes least square minimization methods. In these methods the problem in Eq. 5.4 is discretized and written in a matrix form. This matrix equation gives rise to a least square minimization problem. Because of the ill-posed nature of the inverse problem, regularizations are needed to obtain a unique solution that is not dominated by noise. We will address regularizations used in the non-negative least square (NNLS) approach, the non-negative Tikhonov (NNT) approach and the maximum entropy method (MEM) in Sec. 5.2.3.

5.2.1 Padé approximant method

In the Padé approximant method a function $\tilde{G}(z)$ is fitted to the input data $G(i\omega_n)$. The analytic structure of the data is usually not known, but the Padé method assumes that the function can be written as a fraction of two polynomials $P(z)$ and $Q(z)$, with complex coefficients p_i and q_i respectively. To obtain the correct asymptotic behavior, $1/z$ for one-particle Green's functions and $1/z^2$ for two-particle functions, the polynomial degree of $Q(z)$ is respectively one or two higher than the polynomial degree of $P(z)$. For now we focus on the fermionic case, but everything is easily extended to the bosonic case².

²For bosonic Green's functions the asymptotic behavior for large z is $1/z^2$, the fractional polynomial can already have this form by assuming $p_r = 0$.

The fractional polynomial can be explicitly written as:

$$\tilde{G}(z) = \frac{P(z)}{Q(z)} = \frac{p_1 + p_2 z + \dots + p_r z^{r-1}}{q_1 + q_2 z + \dots + q_r z^{r-1} + z^r}. \quad (5.6)$$

There are several schemes for finding the Padé approximant, such as Thiele's reciprocal difference method [8] or Beach' algorithm [11]. We use the latter approach for finding the Padé approximant. In Beach' scheme the $2r$ unknown complex coefficients, *i.e.* p_i and q_i , are calculated by specifying $\tilde{G}(z = i\omega_n) = G(i\omega_n)$ for $2r$ Matsubara points. Using $2r$ Matsubara frequencies to calculate $2r$ unknown coefficients results in a set of $2r$ linear equations. Beach *et al.* [11] conveniently casted these equations in a matrix form, by defining the column vectors

$$\begin{pmatrix} \mathbf{p} \\ \mathbf{q} \end{pmatrix} = \begin{pmatrix} p_1 \\ \vdots \\ p_r \\ q_1 \\ \vdots \\ q_r \end{pmatrix} \in \mathbb{C}^{2r} \quad \text{and} \quad \mathcal{G} = \begin{pmatrix} G_{i\omega_1}(i\omega_1)^r \\ G_{i\omega_2}(i\omega_2)^r \\ \vdots \\ G_{i\omega_{2r}}(i\omega_{2r})^r \end{pmatrix} \in \mathbb{C}^{2r}. \quad (5.7)$$

In the above definition we denote the datapoint at $i\omega_n$ with $G_{i\omega_n}$ to avoid confusion with multiplication by $(i\omega_n)^r$. With these definitions and the row vector $(1 \ z \ z^2 \ \dots \ z^{r-1})$, the approximant \tilde{G} can be rewritten as:

$$\tilde{G} = \frac{(1 \ z \ z^2 \ \dots \ z^{r-1}) \cdot \mathbf{p}}{(1 \ z \ z^2 \ \dots \ z^{r-1}) \cdot \mathbf{q} + z^r}. \quad (5.8)$$

This casts the set of $2r$ linear equations ($\tilde{G}_{i\omega_n} = G_{i\omega_n}$) into the following form:

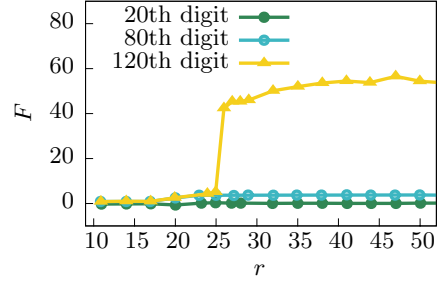
$$\begin{pmatrix} 1 & i\omega_1 & \dots & (i\omega_1)^{r-1} & -G_{i\omega_1} & \dots & -G_{i\omega_1}(i\omega_1)^{r-1} \\ 1 & i\omega_2 & \dots & (i\omega_2)^{r-1} & -G_{i\omega_2} & \dots & -G_{i\omega_2}(i\omega_2)^{r-1} \\ \vdots & \vdots & & \vdots & \vdots & & \vdots \\ 1 & i\omega_{2r} & \dots & (i\omega_{2r})^{r-1} & -G_{i\omega_{2r}} & \dots & -G_{i\omega_{2r}}(i\omega_{2r})^{r-1} \end{pmatrix} \begin{pmatrix} \mathbf{p} \\ \mathbf{q} \end{pmatrix} = \mathcal{G}. \quad (5.9)$$

If we now denote the matrix in the above equation as $\mathcal{K} \in \mathbb{C}^{2r \times 2r}$, the problem of finding the coefficients $\{p_i\}$ and $\{q_i\}$ boils down to an inverse matrix problem:

$$\begin{pmatrix} \mathbf{p} \\ \mathbf{q} \end{pmatrix} = \mathcal{K}^{-1} \mathcal{G}. \quad (5.10)$$

Typically the condition number of this matrix is very high and it is very hard to take a good numerical inverse. For an inverse of \mathcal{K} that is not dominated by numerical errors, a fairly high numerical precision is needed. An estimate for

Figure 5.3. The accuracy of the Padé approximant. The integrated square of the difference between the approximant and the exact function has order 10^{-F} for approximants obtained with input points that have noise at the 20th, 80th or 120th decimal digit. This accuracy is given as a function of the number of poles r . The data are taken from Ref. [11].



the numerical precision is given by the ratio between the largest and the smallest entry of \mathcal{K} . For $G(z) \sim \frac{1}{i\omega_n}$, this ratio is $\sim (\omega_{2r})^r = [(4r-1)\pi T]^{\pm r}$, where \pm is used for a base bigger or smaller than 1. The required numerical precision is estimated to $2r \log_{10}((4r-1)\pi T)$ decimal digits [11]. As is shown in for example Ref. [11] and partially reproduced in Fig. 5.3, the Padé approximant method, formulated as a matrix problem, works very well for extremely high precision data $G(i\omega_n)$. However, in real world problems one rarely has such precise input data.

Another issue of the Padé approximant method is the choice of r . Since there is usually no *a priori* knowledge on the analytic form of the Green's function, it is not evident which order the polynomials $P(z)$ and $Q(z)$ in Eq. 5.6 should have. For more insight in this issue, it is useful to rewrite the approximant \tilde{G} in Eq. 5.6 as:

$$\tilde{G}(z) = C \frac{\prod_{i=1}^{r-1} (z - a_i)}{\prod_{i=1}^r (z - b_i)} = \sum_{i=1}^r \frac{w_i}{z - b_i}. \quad (5.11)$$

The first equality in Eq. 5.11, is obtained by factorizing the polynomials and expresses \tilde{G} as a product of poles and zeros. The second equality takes the form of weighted poles. The weights (residues) w_i of the i th pole can be found with some algebra [80].

Let us now return to the issue of choosing the polynomial order r . Suppose that the true function has r_{true} poles. It is quite evident that a Padé approximant with $r \ll r_{\text{true}}$ will not be able to produce a good fit. On the other hand, in a Padé approximant with $r \gg r_{\text{true}}$, a lot of poles in the denominator of the approximant, should be canceled out by zeros in the numerator. Since we are dealing with a numerical problem, with finite precision, this cancelation will not be exact. The bigger the difference between r and r_{true} , the more problems this might give. However r_{true} is generally not known, and one needs to make an estimated guess of r_{true} . In Ref. [11] the authors propose a method to estimate r_{true} and then use this for the procedure. However they advise to improve the accuracy of the data, which is in real calculations, not always feasible. In Ref. [80], the authors propose to make sure that $r \gg r_{\text{true}}$ and remove superflu-

ous poles from the approximant. They propose several methods to select this spurious pole-zero pairs.

The problem of taking $r \gg r_{\text{true}}$ is that one fits the approximant partially to numerical noise. This results in not exactly canceling pole-zero pairs which gives rise to spurious features in the spectrum. In Paper V we try to tackle this problem in two ways. First the over-fitting is reduced by considering more input points than Padé coefficients. Second, an average is taken over several continuations. Since one expects noise to be random, one also expects the spurious features, *i.e.* the not exactly canceling zero-pole pairs to be distributed randomly for different r . The average over several continuations with different r should average out the spurious features. As to the first point, in order to have more input points than Padé coefficients, the matrix problem should be reformulated in a least-square minimization, as was already suggested in Ref. [79]. So instead of $2r$ Matsubara frequencies, we now consider $M \geq 2r$ data points and the vector \mathcal{G} in Eq. 5.7 becomes $\mathcal{G} \in \mathbb{C}^M$. The matrix \mathcal{K} in Eq. 5.9 will have M rows, but still $2r$ columns, *i.e.* $\mathcal{K} \in \mathbb{C}^{M \times 2r}$. The coefficients are found by least square minimization:

$$\min \left\| \mathcal{K} \begin{pmatrix} \mathbf{p} \\ \mathbf{q} \end{pmatrix} - \mathcal{G} \right\|. \quad (5.12)$$

Since there are “not enough” coefficient to precisely fit all M data points, the data points are fitted as good as possible, and the risk of over-fitting to numerical noise decreases. As to the second point, having the least square approach also allows us to have more continuations and to devise special averaging schemes to improve the quality. These schemes are extensively covered in Paper V, but a simple example is that all spectra with spurious features that are clearly unphysical can be left out of the average. An example of a clearly unphysical spectrum is a spectrum that is (partially) negative.

Finally we give a sneak-preview of our results. In Paper V and VI we use this least square Padé approach together with a scheme where several continuations with varying M and $N = 2r$, with $N \leq M$, are averaged. In Fig. 5.4 we give an example from Paper VI of continuations for different (N, M) pairs. For each pair it is denoted whether the continuation was physical *i.e.* $A(\omega) \geq 0 \forall \omega$ or unphysical *i.e.* $\exists \omega | A(\omega) \leq 0$. Moreover the amount of physical continuations for each averaging area is plotted. The averaging area was defined as M and N between $M_{\text{max}} - 47$ and $M_{\text{max}} + 1$ in steps of 4, under the constraint of not having more coefficients than Matsubara points. If $M_{\text{max}} - 47 < 4$, then 4 is used as the lower boundary instead. This figure illustrates that both much too few and much too many poles in the approximant result with high probability in unphysical continuations. Therefore a big area with (N, M) pairs has to be chosen to make optimal use of the averaging procedure.

In Paper V we compare this average least square Padé approach, to the original Padé method and several other methods of analytic continuation for fermionic functions.

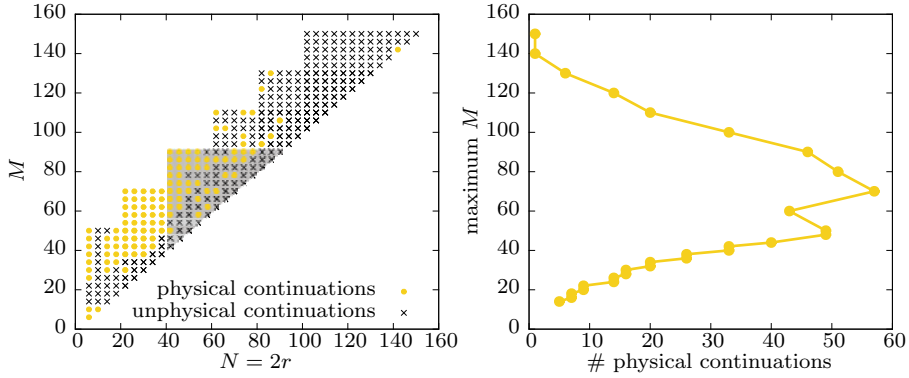


Figure 5.4. The least square Padé approach for $M \geq N = 2r$. In the left panel we sketched for the two-pole function of Paper VI the physical (yellow dots) and unphysical (black crosses) continuations for different (N, M) pairs. The grey area denotes an example of the averaging area for $M_{\max} = 90$. In the right panel, one sees how the amount of physical continuations in the averaging area is varying with respect to M_{\max} . Note, not all (N, M) pairs are displayed in the left plot

5.2.2 Stochastic Sampling

A very different approach is offered by the method introduced by Mishchenko *et al.* [70]. This method is based on Monte-Carlo sampling. The main idea is to build a random spectrum on the real axis and use this to calculate $G(i\omega_n)$ through Eq. 5.1 or the more general Eq. 5.4. This integral is easily done numerically and is much easier than the inverse problem. The random spectrum is accepted or rejected in the Monte-Carlo chain using an algorithm depending on the difference between the calculated $G(i\omega_n)$ and the known data on the imaginary axis. This sampling method, hereafter referred to as Mishchenko's method, is good, but very time consuming. In Paper VII, we investigate the possible advantages of a GPU implementation of Mishchenko's method alternative to the original CPU version [70]. The basic structure of the method will be outlined below.

In Mishchenko's method, a random spectrum $C(\omega)$ on the real axis is generated by a sum of R rectangles

$$C(\omega) = \sum_i^R \chi_{P_i}(\omega), \quad (5.13)$$

where the set $P_i = \{h_i, w_i, c_i\}$ gives the height, width and center position of the rectangle χ_{P_i} , see also Fig. 5.5. At first iteration, these rectangles are randomly generated and thereafter, they are randomly updated. Possible updates are 1. a shift of the center position of a rectangle, 2. a change of the width and height of a rectangle while keeping the weight, 3. a change the weight of two rectangles, while keeping the total weight, 4. an addition of a new rectangle

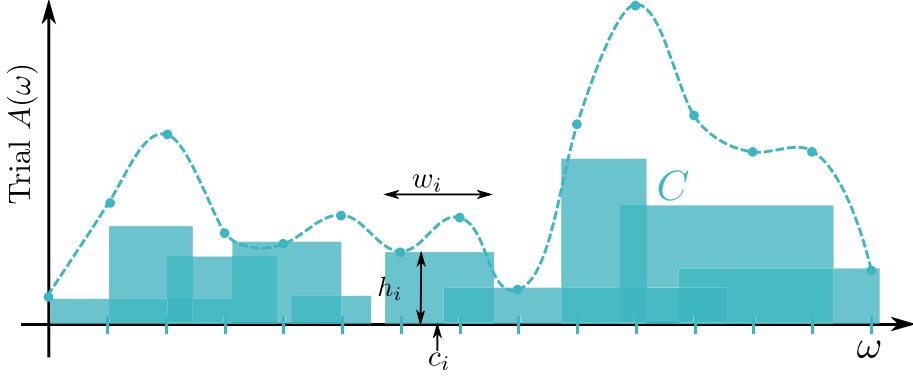


Figure 5.5. Illustration of a configuration $C(\omega)$ composed by a set of rectangles, each of which specified by h_i , w_i and c_i .

and a reduction of the weight of an old, 5. a removal of a rectangle, and a corresponding increase of the weight of an old, 6. a separation of a rectangle into two parts, 7. a union of two rectangles. The total weight of the spectrum is always kept constant. These changes are accepted or rejected according to an algorithm that depends on the distance between the known Matsubara data, and the function generated by $C(\omega)$ through Eq. 5.4. The algorithm accepts updates that reduce the distance with a high probability and updates that increase the distance with a lower probability. In this way, a series of E elementary updates is constructed. From this series, the trial spectrum $C_r(\omega)$ with the smallest distance between the known Matsubara data, and the function generated by $C_r(\omega)$ is picked to construct the next sequence of E elementary updates. This is done L times, where L is the number of local updates. In summary:

$$\begin{array}{l}
 \left. \begin{array}{l}
 C_0 \rightarrow C_1 \rightarrow \dots \rightarrow C_r \rightarrow C_{r+1} \rightarrow \dots \rightarrow C_E \\
 \quad \quad \quad \hookrightarrow C_0 \rightarrow C_1 \rightarrow \dots \rightarrow C_{r'} \rightarrow C_{r'+1} \rightarrow \dots \rightarrow C_E \\
 \quad \quad \quad \vdots \\
 \quad \quad \quad \hookrightarrow C_0 \rightarrow \dots \rightarrow C_{r''} \rightarrow \dots
 \end{array} \right\} L \\
 \quad \quad \quad \Downarrow \\
 \quad \quad \quad A_i(\omega)
 \end{array}$$

This procedure is repeated M times (number of global updates) and the resulting M global solutions A_i are averaged to obtain an $A(\omega)$. The advantage of the averaging procedure is that the saw-tooth noise, inherent to the ill-posed nature of the inversion problem, is averaged out.

More information on our GPU implementation of Mishchenko's method, can be found in the Bachelor thesis of Johan Nordström [74], and the code is available through Ref. [75, 76].

5.2.3 Least square solutions and regularizations

To obtain the least square (LS) solutions³ of the inverse problem in Eq. 5.4, the latter is discretized in one way or the other. The variable y is usually already discretized by the known data, suppose over m points. In our case the Green's function is only given at the Matsubara frequencies. The range of the model, *i.e* the range of the spectral function, can be discretized on a grid of n points and the integral is numerically discretized

$$\int K(y_j, x)A(x)dx \approx \sum_{i=1}^n w_i K(y_j, x_i)A(x_i), \quad (5.14)$$

where w_i is the integration weight and $A(x_i)$ and $K(y_j, x_i)$ are the discretized versions of the model and the Kernel. The discretized version of Eq. 5.4 can be written as a matrix equation. For this we use that the real and imaginary part of the equation can be separated (Eq. 5.5) and we introduce the vectors $\mathbf{G} \in \mathbb{R}^{2m}$, $\mathbf{A} \in \mathbb{R}^n$ and the matrix $\mathbf{K} \in \mathbb{R}^{2m \times n}$

$$\mathbf{G} = \begin{pmatrix} \text{Re } G(y_1) \\ \text{Re } G(y_2) \\ \vdots \\ \text{Re } G(y_m) \\ \text{Im } G(y_1) \\ \vdots \\ \text{Im } G(y_m) \end{pmatrix}, \quad \mathbf{A} = \sqrt{w_i} \begin{pmatrix} A(x_1) \\ A(x_2) \\ \vdots \\ A(x_n) \end{pmatrix} \quad \text{and}$$

$$\mathbf{K} = \sqrt{w_i} \begin{pmatrix} \text{Re } K(y_1, x_1) & \text{Re } K(y_1, x_2) & \cdots & \text{Re } K(y_1, x_n) \\ \text{Re } K(y_2, x_1) & \text{Re } K(y_2, x_2) & \cdots & \text{Re } K(y_2, x_n) \\ \vdots & \vdots & \ddots & \vdots \\ \text{Re } K(y_m, x_1) & \text{Re } K(y_m, x_2) & \cdots & \text{Re } K(y_m, x_n) \\ \text{Im } K(y_1, x_1) & \text{Im } K(y_1, x_2) & \cdots & \text{Im } K(y_1, x_n) \\ \vdots & \vdots & \ddots & \vdots \\ \text{Im } K(y_m, x_1) & \text{Im } K(y_m, x_2) & \cdots & \text{Im } K(y_m, x_n) \end{pmatrix}$$

to obtain

$$\Rightarrow \mathbf{G} = \mathbf{K}\mathbf{A}. \quad (5.15)$$

Simply trying to solve this set of equations will not work, because of the ill-posed nature of the inverse problem. There are generally two problems

1. \mathbf{K} is not surjective \Rightarrow not for every data set \mathbf{G} there exists a model \mathbf{A} (because \mathbf{G} including the noise falls outside the range of \mathbf{K})

³For this section on least square solutions, the master thesis of Ghanem [34] has been very helpful

2. \mathbf{K} has a non-trivial null space (kernel⁴) \Rightarrow if there is one (approximate) solution \mathbf{A} to the data \mathbf{G} , there are immediately infinitely many solutions. Instead of finding the exact solution to Eq. 5.15, we try to find a model that reproduces the data closest. This can be done by approaches that have the least square solution as starting point. In the least square approach, the solution is found by minimizing the Euclidean distance between the known data \mathbf{G} and the data produced by the model \mathbf{KA} with respect to the model \mathbf{A}

$$\min_{\mathbf{A} \in \mathbb{R}^n} \|\mathbf{KA} - \mathbf{G}\|. \quad (5.16)$$

Additionally the condition that the norm of \mathbf{A} is minimal is added to obtain a unique solution. This is needed because, the dimension of the vector space spanned by the columns or rows of \mathbf{K} is usually less than the lesser between the number of rows and columns. In other words, \mathbf{K} is rank deficient. This implies that \mathbf{K} is not surjective, but also that it has a non-trivial null space, as mentioned before. Therefore there are infinitely many solutions to the minimization problem in Eq. 5.16, since adding or removing a vector from the null space of \mathbf{K} to the model \mathbf{A} will not change \mathbf{KA} . This minimization approach often gives a spectrum that is dominated by the noise. Adding prior knowledge to the LS problem helps to solve the ill-posed problem. In the next paragraphs we will discuss several of the regularization methods, namely the Non-Negative Least Square (NNLS) approach, the Tikhonov regularization and the regularization used in the MEM.

Non-Negative Least Square

The LS solution can be improved by using the prior knowledge that the spectral function is positive $\mathbf{A} \geq 0$. This leads to the non-negative least square (NNLS) approach [58], where the additional constraint of positive \mathbf{A} is added to the minimization problem in Eq. 5.16.

Tikhonov regularization

To understand the origin of the Tikhonov regularization it is useful arrive at the least square solution in Eq. 5.16 by decomposing the matrix \mathbf{K} in singular values and constructing a pseudo inverse of \mathbf{K} . Hence, before proceeding with the Tikhonov regularization we will introduce the pseudo inverse of \mathbf{K} with help of the singular value decomposition of \mathbf{K} .

The idea of creating a pseudo inverse of \mathbf{K} is to circumvent the non-surjectivity and non-injectivity of \mathbf{K} by restricting \mathbf{K} to a linear map $\mathbf{K}' : (\ker(\mathbf{K}))^\perp \rightarrow \text{Im}(\mathbf{K})$, where $(\ker(\mathbf{K}))^\perp$ is the orthogonal complement of the null space of \mathbf{K} and $\text{Im}(\mathbf{K})$ is the image of \mathbf{K} . With these restrictions \mathbf{K}' is injective and surjective and can be inverted. The pseudo inverse \mathbf{K}^+ of \mathbf{K} is now defined as

⁴Although the word kernel is frequently used to denote the null space, I think it will be highly confusing in this context. I will therefore use the word null space, but the symbol will still be $\ker(\mathbf{K})$.

the inverse of \mathbf{K}' on $\text{Im}(\mathbf{K})$ and zero on $(\text{Im}(\mathbf{K}))^\perp$. This pseudo inverse can be simply calculated with help of singular value decomposition, where the matrix \mathbf{K} is decomposed such that

$$\mathbf{K} = \mathbf{U}\mathbf{S}\mathbf{V}^T. \quad (5.17)$$

Here $\mathbf{U} \in \mathbb{R}^{2m \times 2m}$ and $\mathbf{V} \in \mathbb{R}^{n \times n}$ are orthogonal matrices and \mathbf{S} is a matrix in $\mathbb{R}^{2m \times n}$, with the singular values s_i on the “diagonal” (entry S_{ii}) ordered from big to small. Note that some of the singular values might be zero. The pseudo inverse \mathbf{S}^+ of the “diagonal” matrix \mathbf{S} is constructed by taking the inverse of the non-zero singular values on the “diagonal”, keep the zero’s and transpose the entire matrix. The pseudo inverse of \mathbf{K} is now

$$\mathbf{K}^+ = \mathbf{V}\mathbf{S}^+\mathbf{U}^T. \quad (5.18)$$

The least square solution of Eq. 5.16 can now be obtained by $\mathbf{A} = \mathbf{K}^+\mathbf{G}$. From the definition of \mathbf{K}^+ in Eq. 5.18 that contains the inverse of the singular values, one can see that this solution is quite unstable, especially in numerical calculations. For example: how small should a singular value be, to be called “zero”? The small singular values, *i.e* the values that become huge in the pseudo inverse, result in a LS spectrum that is dominated by noise. To diminish the influence of noise, regularization methods are applied. From Eq. 5.18 one can see that a very simple regularization is to zero all singular values smaller than a parameter ε . This regularization is called truncated Singular Value Decomposition.

A slightly more elaborate regularization is the Tikhonov regularization [92]. In this regularization the small singular values are not simply ignored, but in the final solution they contribute less than the big singular values. To achieve this, the inverted singular values s_j in the pseudo inverse are multiplied by $h_\alpha(s_j)$. This damping function in terms of parameter α is given by:

$$h_\alpha(s_i) = \frac{s_i^2}{s_i^2 + \alpha^2}. \quad (5.19)$$

Eqs. 5.18 and 5.19 show that the modes, *i.e.* the columns of \mathbf{U} and \mathbf{V} , in Eq. 5.18 are damped according to the magnitude of their singular value. The Tikhonov scheme can also be written as a regularized least square minimization:

$$\min_{\mathbf{A} \in \mathbb{R}^n} \left((\|\mathbf{K}\mathbf{A} - \mathbf{G}\|)^2 + \alpha^2 (\|\mathbf{A}\|)^2 \right). \quad (5.20)$$

In this scheme a balance is found between minimizing $\|\mathbf{K}\mathbf{A} - \mathbf{G}\|$ and minimizing the norm of \mathbf{A} depending on the parameter α . This parameter can be found with the L -curve method [43]. If now also the non-negativity constraint is added, we find the non-negative Tikhonov (NNT) solution.

Maximum Entropy method (MEM)

The maximum entropy regularization [50] uses the positiveness and the integrability of the spectral function⁵ to interpret it as a probability distribution. The maximum entropy method (MEM) approaches the problem of analytic continuation with Bayesian probabilities. The main idea is to find a model or spectrum $A(x)$ that maximizes the conditional probability of finding A given the input data G , *i.e.* $P[A|G]$. Using Bayes rule

$$P[A|G] = P[G|A]P[A]/P[G] \quad (5.21)$$

the problem of finding $P[A|G]$ changes to finding the likelihood function $P[G|A]$ and the prior function $P[A]$. Since G is given, the $P[G] = \int \mathcal{D}A P[G|A]P[A]$ is mainly a normalization factor. The simplest approach is to ignore the probability $P[A]$ and use the method of maximum likelihood [50]. By maximizing the probability

$$P[A|G] \propto P[G|A] \propto e^{-L}, \text{ where } L = \frac{1}{2} \|\mathbf{G} - \mathbf{K}\mathbf{A}\|^2 \Rightarrow \quad (5.22)$$

$$\min_{A \geq 0} \frac{1}{2} \|\mathbf{K}\mathbf{A} - \mathbf{G}\|^2 \quad (5.23)$$

we can arrive at exactly the same expression as in Eq. 5.16 together with the non-negativity constraint of NNLS. In the above equation we discretized $A(x)$, $G(y)$ and $K(y,x)$ as described before. However, in MEM, the prior function $P[A]$ is not ignored, but obtained from the principle of maximum entropy. Therefore

$$P[A] \propto e^{\alpha S}, \text{ where the entropy } S = \sum_i \left[A_i - m_i - A_i \ln \left(\frac{A_i}{m_i} \right) \right], \quad (5.24)$$

with m_i as default model. This default model should be positive, integrable and normalized to 1. If there is additional knowledge on A_i the default model can be chosen such as to favor solutions in agreement with this knowledge. Maximizing the probability of finding A for a given G with this prior function gives the following regularized minimization problem:

$$P[A|G] \propto P[G|A]P[A] \propto e^{-L} e^{\alpha S} \Rightarrow \min_{A \geq 0} \left(\frac{1}{2} \|\mathbf{K}\mathbf{A} - \mathbf{G}\|^2 - \alpha S[\mathbf{A}] \right). \quad (5.25)$$

The value of α can be chosen in several ways [50]. The L-curve method is straightforward and obtains α by minimizing:

$$\min_{\alpha} \|\mathbf{K}\mathbf{A} - \mathbf{G}\| \cdot \|S[\mathbf{A}]\|, \quad (5.26)$$

where \mathbf{A} and S depend on α .

⁵For fermions $A(\omega) \geq 0$ and for bosons $A(\omega)\omega \geq 0$

5.3 Remarks on performance

In the preceding section, we highlighted some methods of analytic continuation that we studied and/or developed in Papers V, VI and VII. In assessing how “good” a method of analytic continuation is, not only the accuracy plays a role. Green’s function data on the Matsubara axis could contain a large amount of noise, especially when they are obtained using quantum Monte Carlo procedures. In these cases it is important that the method of choice performs reasonably well even for noisy input data. Moreover all methods require some method dependent parameters, such as the number of coefficients in the fractional polynomial for the Padé approximant method, the number of Monte Carlo updates in the stochastic sampling procedure or the discretization of the real axis and the regularization parameters in the least square solutions. The methods should be stable with respect to the choice of these parameters. Also the computational time required to analytically continue a function might be of significant importance. Here it is worth noting that analytic continuation is needed in quite different situations. In DMFT approaches often it is needed once at the end of the computational cycle: the entire DMFT computation takes place on the Matsubara axis and only the final results need to be continued to real energies. In this case the restrictions on the computational time are not too severe. However, in other occasions, the process of analytic continuation is part of a bigger computational cycle and needs to be repeated several times. Such is for example the case in EMTD+DMFT (exact muffin tin orbital) or KKR+DMFT (Korringa-Kohn-Rostock) methods, where the LDA routines are usually calculated on a contour in the complex plane. Then analytic continuation to either the real or the imaginary axis is needed when connecting this part to the DMFT part of the cycle. In this case, a fast procedure without arbitrariness or *ad hoc* analysis is desired.

5.4 Summary of Papers V, VI and VII

Paper V: Analytic continuation by averaging Padé approximants

The Padé approximant method for analytic continuation works very well for high precision data on the Matsubara axis [11]. In realistic cases it is however rarely possible to obtain data with such high accuracy and precision. An other problem, as was pointed out in Sec. 5.2.1, is that the true number of poles is not known a priori. An overestimation of the number of poles gives rise to pole-zero pairs that should cancel each other. Due to the presence of noise and the finite numerical precision, this cancellation is often imperfect and leads to spurious features in the spectrum. These spurious features may be even such that they lead to clearly unphysical spectra that are negative in some frequency range.

In Paper V we propose a combination of four remedies to cure these well-known problems. The first remedy is to use less coefficients than input points,

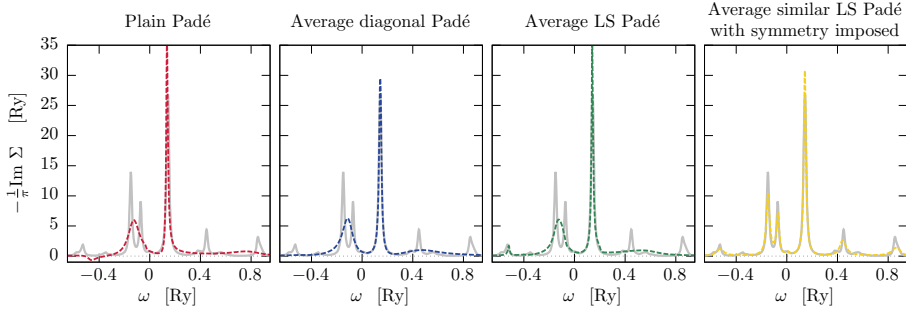


Figure 5.6. The impact on the spectral function of the different improvements on the Padé approximant method. The Plain Padé solution is a single continuation obtained with as many input points as coefficients. The average diagonal Padé solution is an average of several of these continuations. The average LS Padé solution was obtained with continuations where the number of coefficients was less than the number of input points. In the last figure, the mirror symmetry was imposed and a more elaborate averaging scheme was used.

which results in a least square minimization problem [79]. The second remedy is to average several continuations. These different continuations are obtained by varying the number of fitted input points and the Padé coefficients independently. In this way many continuations are obtained and unphysical continuations can be directly disregarded. The third improvement that we studied is to use high precision algebraic routines for the matrix inversion problem [11], even if the input data are of low accuracy. The fourth improvement to the Padé approximant method is to impose some of the mirror symmetry of the Green's function on the Matsubara axis, *i.e.* $G(i\omega_n^*) = G(i\omega_n)^*$, by taking into account some negative Matsubara frequencies in addition to the positive ones. These adjustments to Beach Padé algorithm [11] reduce the problem of spurious features arising from the bad pole-zero cancelation and help in resolving spectral features. Fig. 5.6 presents the improvements with an example taken from Paper V.

In Paper V we apply this improved version of the Padé approximant method to several realistic test cases and compare the results to spectral functions obtained with other methods. We find that the improved Padé approximant method performs very well even for noisy Matsubara data.

Paper VI: A comparison between methods of analytic continuation for bosonic functions

Historically most attention was devoted to the analytic continuation of one-particle Green's functions, whose corresponding one-particle spectral function can be measured more or less directly with photoemission experiments. However, also dynamical two-particle quantities, such as dynamical susceptibilities are of great importance. In principle, the methods of analytic continuation

discussed previously are also applicable to dynamical two-particle quantities. Since, to the best of our knowledge, a thorough study of several methods on several functions corresponding to different physical phenomena has not been performed yet, we try to fill this gap in Paper VI. We focus on the MEM, the NNLS method, the NNT method, the Padé approximant method, and the Stochastic sampling method by Mishchenko *et al.* [70]. The testing ground for these methods contains four different cases: a simple two-pole model, a single-orbital metallic system and a two-orbitals insulating system, as described in a tight-binding model on a square lattice, and the Hubbard dimer. The two flavors of the tight-binding model contain each about 100 different functions belonging to different reciprocal lattice vectors.

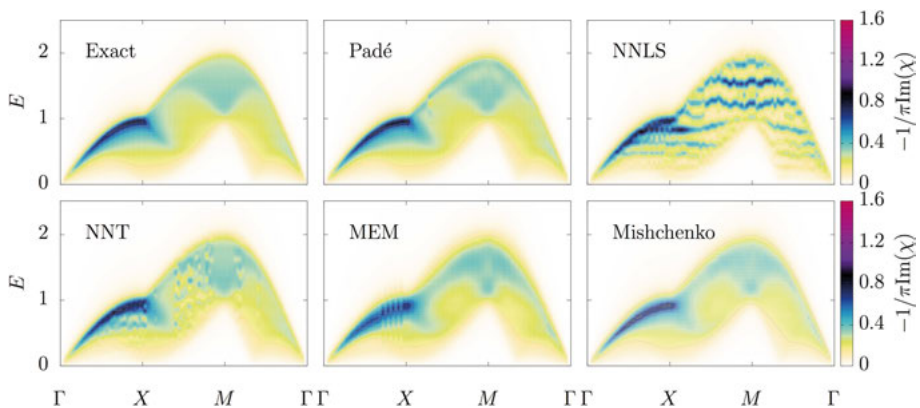


Figure 5.7. Spectrum of the Lindhard function $\frac{1}{\pi} \text{Im}(\chi(\omega + i\delta^+))$ of the two-dimensional doped tight-binding model along the Brillouin zone path $\Gamma \rightarrow X \rightarrow M \rightarrow \Gamma$. In the top left plot the exact spectral function is shown. The other plots give the continuations obtained with the various methods.

We have to conclude that for low input data precision, none of the methods is good enough to give a good continuation for all different tests. However, we think that a combination of several methods can give enough insight to reconstruct the physics. For highly accurate input data, the averaging LS Padé approximant method works quite well, but this method is more sensitive to noise than the other ones. This may become a problem since accurate two-particle Green's functions are even harder to access than their one-particle counterpart. On the other hand, Mishchenko's method seems to be most robust across various levels of input accuracy. The drawback of Mishchenko's method is, however, that it is very time consuming.

As an illustration we show the spectra for the doped tight-binding model investigated in Paper VI in Fig. 5.7. These spectra were obtained from relatively high precision input data and one can see that the averaging LS Padé method performs quite well. Also Mishchenko's method and MEM perform quite good.

Paper VII: A GPU code for analytic continuation through a sampling method

The study in Paper VI shows that the stochastic sampling method by Mishchenko *et al.* [70] works quite well, especially since it is very robust against noise in the input data. However one has to face that this method is very time consuming. Luckily, it is also an embarrassingly parallel problem, for all A_i in the scheme on page 77 can be obtained independently. After we worked on an MPI implementation of the original FORTRAN code of Mishchenko [90], we decided to develop an implementation on a Graphics processing unit (GPU) to investigate whether or not it was feasible to exploit the advantages of this powerful computational device.

The GPU was initially developed to accelerate many parallel geometric calculations, used for example in the graphics of video games. After all, in video games all pixels on the screen should be updated every time step and many parallel matrix and vector operations are required. The ability to perform many matrix and vector manipulations in parallel makes GPU valuable for embarrassingly parallel problems in science. A perfect example of this are the global updates in Mishchenko's scheme. With Johan Nordström we implemented Mishchenko's method on GPU and examined the acceleration.

Both the MPI and GPU parallelizations reduce the time one has to wait for a continuation, by performing the global updates at the same time, *i.e.* in parallel. It is not so straight forward to compare CPU and GPU times, but the following example can give an indication of the computational effort. A continuation with 128 global updates and 60000 local updates, is done by one GPU in less than one hour or by 128 CPU's in nearly 3 hours. Apart from the absolute speed-up of the GPU relative to the CPU's, one GPU is more energy efficient than 128 CPU's. In general the trend is that GPU programs are more energy efficient than their CPU equivalent [71]. Moreover, contrary to hundreds of CPUs that are only available in supercomputer facilities, a GPU is directly accessible on a common laptop. In Fig. 5.8 we show the good scalability of the program for two GPUs that were part of a laptop.

The code developed for Paper VII can be found in Ref. [75] and more details on the implementation are written in Ref. [74]. We find that with the GPU implementation of Mishchenko's method one can obtain reasonable analytic continuations in a short time without the need of supercomputing facilities.

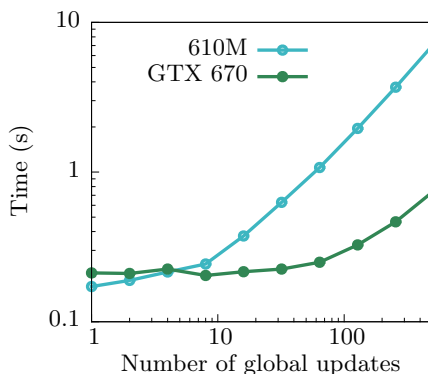


Figure 5.8. Scalability of the GPU implementation of Mishchenko's method for two different GPUs. Data were taken from Paper VII.

5.5 Outlook

In Paper V we showed that the Padé approximant method works very well for one-particle Green's functions and self-energies. We put a lot of effort into improving the quality of the continuations even for low precision input data. We would like to implement our Padé routine into our RSPt code [97] for two purposes. Firstly, to continue the Green's function resulting from the DMFT cycle in order to obtain the spectral function. This feature is needed for the quantum Monte Carlo and the spin polarized T-matrix fluctuation solver, since these solvers obtain the Green's function on the Matsubara axis. The second application is of a more technical nature. For the exact diagonalization solver, the hybridization function (see Eq. 2.17 in Sec. 2.3) is fitted with only a few hybridization parameters. On the Matsubara axis, this function has relatively little structure. It may therefore be worth to analytically continue the hybridization function to the real axis, fit the few parameters to this function and use it in the exact diagonalization solver.

Regarding technical improvements of the Padé approximant method, it may be useful to investigate further the use of some negative Matsubara frequencies to impose the mirror symmetry of the Green's function. For the moment we can say that taking into account some negative frequencies improves the continuation of one-particle Green's functions that go to zero for small Matsubara frequencies, such as the atomic self-energies of Sm and Pr in Paper V. For metallic Green's functions, such as the Green's function of the Bethe lattice, taking negative $i\omega_n$ into account does not improve the continuation. We believe that this originates from the discontinuity of the Green's function when going from positive to negative Matsubara frequencies for metallic systems contrary to the continuity for insulating Green's functions, see Fig. 5.9. Also for two-particle Green's functions, taking into account negative frequencies did not improve the continuation. Relatively broad features are even described

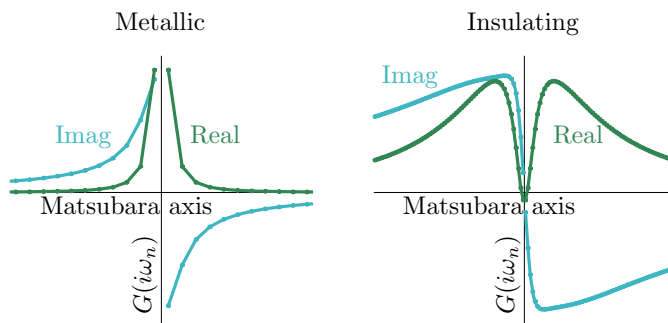


Figure 5.9. Sketch of the behavior of metallic and insulating one-particle Green's function around $i\omega_n = 0$. The metallic Green's function has a discontinuity in the imaginary part when going from negative to positive Matsubara frequencies.

less accurately. We speculate that broad features are usually associated to branch cuts, which are very difficult to describe with single poles close to the real axis. We think it would be worth to investigate this issue further to really pinpoint in which cases negative Matsubara frequencies improve the quality of the continuations, or if there are other ways to impose mirror symmetry or favor mirror symmetric solutions.

Although at the moment I do not have any idea on how, it would be important to find a more reliable method of analytic continuation for two-particle Green's functions. This can be very relevant if one wants to address two-particle Green's functions with the three original frequencies (see Eq. 5.3). In this case, errors associated to the continuation are going to be summed up when passing to the next frequency.

From a computational point of view, we would like to improve our implementation [75] of the stochastic sampling method by Mishchenko *et al.* [70]. We think that using a GPU for this purpose can be highly beneficial, and that further development of the code would be a good investment. We could also consider to implement and test different kernels, related to Fredholm equations in other areas of research.

Popular scientific summary

SINCE time immemorial, materials have been important for mankind. Some prehistoric periods are named after commonly used materials and the discovery of new materials has always held the potential of changing the world. Even nowadays, the development of many applications is restricted by the properties of the materials at our disposal. For example, why do we not have a laptop that you crease in your pocket like a handkerchief? Or why do we not have parasols covered with solar cells on every sunny terrace? These are only a few examples for which we need new materials with new desired properties. To find these materials, engineers as well as experimental and theoretical material scientists try to understand the physics behind these properties and try to figure out where we could find them. Examples of such properties are transparency, the ability to conduct electric current, the flexibility or the amount of magnetization. As theoretical material scientists we aim to calculate these properties and we try to understand the underlying physics from our calculations. To this aim, we need theoretical methods. In this work, we try to improve, develop, and test such methods.

However, before describing the three methods and models in this work, we turn our attention to the materials that we want to describe. All materials consist of atoms, like lego pirate ships consist of lego bricks. However, atoms are about 100 million times smaller than a lego brick⁶. In all materials in the world, we find only about 100 different types of atoms. Similarly, with many, but only 100 different types of lego bricks, one could build pirate ships as well as giraffes or palm trees. The only difference is the way you put the bricks together. An example on the atomic scale is that both diamond and the graphite stick in your pencil, consist of solely carbon atoms. They differ only by the stacking of these atoms! If we focus on the atoms again, they, in turn, consist of a nucleus surrounded by electrons. The electrons are attracted by the nucleus, but repelled by one another. In this thesis we try to understand and predict the properties of materials from this atomic scale, by describing the behavior of the electrons.

This thesis consists of three parts, where we consider three different methods or models:

1. A method to describe the electronic structure of the rare earths

When we put atoms together, to build a material, these electrons can stay close

⁶The lego brick of course consists of atoms itself.

to the nucleus, or they can wander around in the material, hopping from nucleus to nucleus. The behavior of the electrons depends on the type of atom they belong to. In the rare-earth elements, which are a specific class of atoms, some of the electrons wander around and some stay very close to their nucleus. It turned out, that this is very hard to properly describe theoretically. The common theoretical tool to describe the electronic structure of materials is called density functional theory. This method works very well for many types of atoms, but precisely for the rare earths it does not work so well. This is due to the fact that the electrons that stay close to the nucleus feel a strong repulsion from one another. Density functional theory describes this repulsion only partially and for the rare earths this repulsion needs to be taken into account explicitly. In this thesis we examined and analyzed a way to take this into account: the Hubbard I approximation. In this work we show that this method works very well to describe the rare-earth elements. These elements are used in strong permanent magnets as can be found in, for example, wind-mills and electric cars.

2. A model to predict the microscopic state after ultrafast magnetization dynamics

Some atoms can act like a tiny magnet, with a south pole on one end, and a north pole on the other end. All these tiny little magnets constitute a total magnetization in a material. Experimentalists can flash an ultrashort laser pulse onto such a material, to probe its characteristics. By measuring the amount of light that is reflected, they can measure the magnetization of the material. It turns out that the material under some circumstances can lose part of its magnetization and, in other circumstances, can gain additional magnetization due to the ultrashort flash. The magnetization is a macroscopic quantity of the entire sample, but to understand the physics, it is interesting to look at the atomic scale. With our model, we predict what happens to the tiny atomic magnetic moments in both cases, *i.e.* the growth and decrease of magnetization. We find that the atomic magnetic moments increase in strength when the total magnetization increases. When the total magnetization decreases, the atomic magnetic moments keep their strength, but they tilt in various directions. We use our predictions on the atomic scale to calculate the macroscopic quantities that the experimentalists measure. In this way the experiments can confirm our model and our model can explain the experiments.

3. Different methods of analytic continuation

Materials are described by their electronic structure, the behavior of the electrons around the nucleus. For materials where some of the electrons wander around and some stay very close to their nucleus, it is not so easy to make good theoretical predictions of this behavior. Most methods that aim to do this, calculate the electronic structure as a function of *imaginary time*. This sounds very fancy, but it is mainly a mathematical trick to make the calcula-

tions easier. However, to obtain real physical quantities, which are a function of real energies, one needs a method of analytic continuation. In our work we extensively tested several methods of analytic continuation and improved some of them for the particular needs in this area of research.

With our work on these methods and models we hope to contribute to the improvement of the state-of-the-art methods used in material science.

Populärvetenskaplig sammanfattning

SEDAN urminnes tider, har material varit viktiga för mänskligheten. Några förhistoriska perioder är namngivna efter använda material under den eran och upptäckten av nya material har alltid haft potentialen att förändra världen. Även idag är utvecklingen av nya applikationer begränsade av egenskaperna hos de material som finns tillgängliga. Till exempel, varför har vi inte bärbara datorer som man kan vika ihop likt en näsduk? Eller varför har vi inte parasoll som är täckta av solceller på varje solig terrass? Detta är bara några få exempel där vi behöver nya material med nya materialegenskaper. För att upptäcka dessa material försöker ingenjörer och materialforskare förstå fysiken bakom dessa egenskaper. Exempel på sådana egenskaper är genomskinlighet, elektrisk ledningsförmåga, flexibilitet och magnetiseringsstyrka. Som teoretiska materialforskare försöker vi beräkna dessa egenskaper och förstå den underliggande fysiken genom våra beräkningar. För att lyckas med detta behöver vi teoretiska metoder. I denna avhandling försöker vi förbättra, utveckla och testa sådana metoder.

Innan vi beskriver de tre metoderna och modellerna i denna avhandling fokuserar vi först på materialen som vi vill beskriva. Alla material består av atomer, likt piratskepp i lego består av legobitar. Dock är atomer ungefär 100 miljoner gånger mindre än en legobit⁷. I alla material i världen finner vi bara ungefär 100 olika typer av atomer. I liknelsen med legor kan vi med enbart dessa typer bygga piratskepp, giraffer eller palmträd, den enda skillnaden är hur man sätter ihop bitarna. Ett exempel på atomskalan är att diamant och blyertspennor båda bara består av kolatomer, de skiljer sig bara i hur atomerna är strukturerade! Om vi återigen fokuserar på atomerna, består de i sin tur av en atomkärna och omgivande elektroner. Elektronerna är attraherade till atomkärnan, men repelleras av varandra. I denna avhandling försöker vi förstå och förutsäga materialegenskaperna från denna atomskala genom att beskriva elektronernas beteende.

Denna avhandling består av tre delar, innehållande tre metoder eller modeller:

1. En metod för att beskriva elektronstrukturen av de sällsynta jordartsmetallerna

När vi för samman atomer för att bygga material, kan dessa elektroner stanna nära atomkärnan eller vandra omkring i materialet, hoppandes från atomkärna till atomkärna. Beteendet av elektronerna beror på vilken sorts atom de

⁷Legobiten består såklart själv av atomer.

tillhör. I de sällsynta jordartsmetallerna, vilka är en särskild klass av atomer, kommer några elektroner att vandra omkring och några att stanna väldigt nära dess atomkärna. Detta har visat sig vara väldigt svårt att beskriva teoretiskt. En vanlig teoretisk metod för att beskriva elektronstrukturen av material kallas täthetsfunktionalteori. Denna metod fungerar väldigt bra för många typer av atomer, men inte för de sällsynta jordartsmetallerna. Detta beror på att elektronerna som är nära atomkärnan känner en stark repulsion från varandra. Täthetsfunktionalteori beskriver enbart delvis denna repulsion och för de sällsynta jordartsmetallerna behöver man explicit behandla effekten av denna repulsion. I denna avhandling studerar och analyserar vi ett tillvägagångssätt för att göra detta: Hubbard I approximationen. I detta arbete visar vi att denna metod fungerar väldigt bra för att beskriva de sällsynta jordartsmetallerna. Dessa ämnen används i starka permanent magneter, till exempel i vindkraftverk och i elektriska bilar.

2. En modell för att förutsäga det mikroskopiska tillståndet efter ultrasnabb magnetiseringsdynamik

Vissa atomer kan bete sig som små magneter, med en sydpol och en nordpol. Alla dessa små magneter utgör en total magnetisering i materialet. Experimentalister kan stråla en ultrakort laserpuls på ett sådant material, för att utröna dess egenskaper. Genom att mäta mängden ljus som reflekteras kan de uppmäta magnetiseringen i materialet. Det visar sig att materialet under vissa omständigheter kan förlora delar av sin magnetisering och under andra förhållanden få en ökad magnetisering, på grund av den korta laserpulsen. Magnetiseringen är en makroskopisk kvantitet för hela provbiten, men för att förstå fysiken är det intressant att betrakta på den atomistiska skalan. Med vår modell förutsäger vi vad som händer med de små magnetiska momenten i båda fallen, det vill säga för ökad och minskad magnetisering. Vi inser att de magnetiska momenten ökar då den totala magnetiseringen ökar. När den totala magnetiseringen minskar, behåller de atomiska magnetiska momenten sin styrka, men de vrider sig till olika riktningar. Vi använder våra förutsägelser på den atomiska skalan för att beräkna de makroskopiska kvantiteter som experimentalisterna mäter. På detta sätt kan experimenten bekräfta vår modell och vår modell kan förklara experimenten.

3. Olika metoder för analytisk fortsättning

Material beskrivs av dess elektronstruktur, det vill säga elektronernas beteende omkring atomkärnan. För material där vissa elektroner vandrar omkring och några är väldigt nära dess atomkärna är det svårt att göra bra teoretiska förutsägelser för detta beteende. De flesta metoder som försöker modellera detta beräknar elektronstrukturen som en funktion av *imaginär tid*. Detta låter väldigt komplext men det är förförallt ett matematiskt trick för att förenkla beräkningarna. Men för att erhålla verkliga kvantiteter, som beror på verkliga energier, behöver man en metod för analytisk fortsättning. I vårt arbete har vi

noggrant testat flera metoder för analytisk fortsättning och förbättrat några av dem, baserat på behoven i detta forskningsfält.

Med vårt arbete på dessa metoder och modeller hoppas vi bidra till att förbättra toppmoderna metoder i materialforskning.

Populair wetenschappelijke samenvatting

SINDS mensenheugenis zijn materialen belangrijk voor de mensheid. Enkele prehistorische perioden zijn zelfs vernoemd naar veelgebruikte materialen van die tijd. De ontdekking van nieuwe materialen kan zorgen voor grote veranderingen in de wereld. Ook de ontwikkeling van moderne technologie wordt nog steeds begrensd door de eigenschappen van de materialen die we ervoor kunnen gebruiken. Waarom hebben we bijvoorbeeld geen laptop die we als een zakdoek in onze broekzak kunnen frommelen? Of waarom hebben we geen zonnecellen op de parasols op de vele zonnige terrasjes? Dit zijn slechts enkele voorbeelden van toepassingen waar we nieuwe materialen voor nodig zouden hebben met nieuwe gewenste eigenschappen. Om deze materiaaleigenschappen te vinden, proberen technici en experimentele en theoretische materiaalwetenschappers de natuurkunde achter materialen te begrijpen. Zij proberen uit te zoeken waar we de gewenste eigenschappen kunnen vinden. Enkele voorbeelden van dit soort eigenschappen zijn transparantie, de mogelijkheid om elektrische stroom te geleiden, de flexibiliteit van het materiaal of de hoeveelheid magnetisatie in het materiaal. Het doel van theoretische materiaalwetenschappers is het berekenen van deze eigenschappen en het begrijpen van de onderliggende natuurkunde vanuit deze berekeningen. Om dit doel te bereiken hebben we theoretische modellen en methodes nodig. In dit proefschrift proberen we dit soort methodes te verbeteren en te ontwikkelen.

Voordat we verder ingaan op de drie methodes en modellen in dit proefschrift, kijken we even naar de materialen die we uiteindelijk willen beschrijven. Alle materialen bestaan uit atomen, net als legopiratschepen bestaan uit kleine legoblokjes. Atomen zijn echter ongeveer 100 miljoen keer kleiner dan legoblokjes⁸. In alle materialen op aarde komen slechts ongeveer honderd verschillende atomen voor. Zo kun je ook, met een doos legoblokjes waar slecht honderd verschillende soorten blokjes inzitten, zowel een piratenschip bouwen als ook een giraffe of een paar palmbomen. Het verschil zit 'm slechts in hoe je de blokjes op elkaar drukt. Een voorbeeld op atomaire schaal is dat zowel diamant als de grafietstaaf in je potlood, enkel uit koolstofatomen bestaat. Het enige verschil is de manier waarop de atomen op elkaar gestapeld zijn!

Wanneer we nu naar de atomen zelf kijken, zien we dat deze bestaan uit een kern, omringd door elektronen. De elektronen worden aangetrokken door

⁸Legoblokjes bestaan natuurlijk zelf ook uit atomen.

de kern, maar stoten elkaar juist af. In dit proefschrift proberen we de eigenschappen van materialen op deze atomaire schaal te begrijpen en te voorspellen, door te kijken naar het gedrag van de elektronen.

Dit proefschrift bestaat uit drie delen waarin we drie verschillende methodes of modellen bekijken:

1. Een methode om de elektronenstructuur van de zeldzame aardmetalen te beschrijven

Wanneer we de atomen stapelen om een materiaal te vormen, kunnen de elektronen dicht bij hun kern blijven, of juist vrij door het materiaal heen bewegen, al springend van kern naar kern. Het gedrag van de elektronen hangt af van het atoom waar ze toe behoren. De zeldzame aardmetalen zijn een bepaalde groep atomen. Deze atomen worden bijvoorbeeld gebruikt in sterke permanente magneten die hun toepassing vinden in, bijvoorbeeld, windmolens en elektrische auto's. Bij deze groep atomen zijn er enkele elektronen die zich vrij door het gehele materiaal bewegen en enkele die dicht bij hun eigen kern blijven. Het blijkt, dat het erg lastig is om dit theoretisch te beschrijven. De meest gebruikte theoretische methode voor het beschrijven van de elektronenstructuur van materialen heet dichtheidsfunctionaaltheorie. Deze methode werkt voor veel atoomsoorten heel goed, maar juist voor de zeldzame aardmetalen niet zo goed. Dit komt omdat de elektronen die bij hun eigen kern blijven ook dicht bij elkaar zijn en daarom een sterke afstotende kracht van elkaar voelen. Dichtheidsfunctionaaltheorie beschrijft deze kracht slechts gedeeltelijk en voor de zeldzame metalen moet deze afstotende kracht expliciet meegenomen worden in de berekeningen. In dit proefschrift onderzoeken en analyseren we een manier om dit te doen: de Hubbard I benadering. We laten zien dat deze methode goed werkt om de zeldzame aardmetalen te beschrijven.

2. Een model om de microscopische toestand na ultrasnelle magnetisatiedynamica te voorspellen

Sommige atomen zijn net kleine magneetjes, met een zuidpool aan de ene kant en een noordpool aan de andere kant. Al deze kleine magneetjes vormen tezamen de totale magnetisatie van het materiaal. Om de eigenschappen van zo'n materiaal te onderzoeken, kunnen experimentelen een ultrakorte laserpuls op zo'n materiaal flitsen. Door de hoeveelheid licht te meten die wordt gereflecteerd, kunnen ze de magnetisatie van het materiaal bepalen. Het blijkt dat het materiaal, door een felle laserflits, een deel van zijn magnetisatie kan verliezen, terwijl het onder andere omstandigheden juist extra magnetisatie krijgt. De magnetisatie is een eigenschap van het hele materiaal, maar om de natuurkunde te begrijpen is het interessant om op atomaire schaal te kijken wat er gebeurt. Met ons model voorspellen we wat er gebeurt met de kleine atomaire magneetjes in beide gevallen, namelijk tijdens de groei en de krimp van de magnetisatie. We laten zien dat de atomaire magneetjes sterker worden wanneer de totale magnetisatie groter wordt. Wanneer de totale magnetisatie

kleiner wordt, zullen de atomaire magneetjes even sterk blijven, maar naar verschillende richtingen kantelen. We gebruiken onze voorspellingen op atomaire schaal om de macroscopische grootheden te berekenen die de experimentelen kunnen meten. Op deze manier kunnen experimentele metingen ons model bevestigen en kan ons model de metingen verklaren.

3. Verschillende methodes voor analytische voortzetting

Materialen worden beschreven door hun elektronenstructuur, het gedrag van de elektronen rond hun kern. Voor de materialen waar sommige elektronen zich vrij rond bewegen en andere elektronen juist dicht bij hun kern blijven, is het niet zo makkelijk om goede theoretische voorspellingen over dit gedrag te doen. De meeste methodes die dit doen, berekenen de elektronenstructuur als een functie van *imaginaire tijd*. Dit klinkt heel ingewikkeld, maar het is slechts een wiskundig trucje om de berekeningen makkelijker te maken. Het is echter wel belangrijk om aan het einde van de rit weer terug te keren naar *echte* energie in plaats van *imaginaire tijd* en daarvoor hebben we een methode voor analytische voortzetting nodig. In dit proefschrift testen we een aantal methodes voor analytische voortzetting uitgebreid. We verbeteren enkele van deze methodes voor de specifieke behoeftes in dit onderzoeksgebied.

We hopen met het werk dat we in dit proefschrift hebben gedaan, een bijdrage te leveren aan de “state-of-the-art” methodes in de materiaalwetenschap.

Acknowledgements

I am extremely grateful when I reflect upon my time in Uppsala. I got so lucky to meet so many friendly and inspiring people. Here follows only a short list of them.

First of all I would like to thank my supervisors in Uppsala, Igor and Olle. Igor, I think it was really great to work with you. Despite all obstacles, you are always positive, happy and enthusiastic. You were always willing to discuss, to give some new input and to help me. You gave me the feeling that it was safe to try and to fail and to try again. I always felt supported and appreciated by you. I think we had a good collaboration, although, our clocks, somehow, never showed the same time. And very important: we had fun. Thanks a lot!

Olle, it was great to work on a project that lies so close to your heart. Moreover, I think you are the best boss I ever had or even will have. You are always optimistic, enthusiastic and full of ideas. You have so many suggestions for projects and collaborations that it is hard to choose the nicest. As important as your scientific input, I think, is that you really care about your students, post-docs and other colleagues. You care about their well-being and about their future. You encourage social cohesion in our group. With this, I think, you create a very nice atmosphere. I also would like to thank my supervisors for encouraging me to do a joint doctorate with the Radboud University in Nijmegen.

Also I would like to thank my supervisors Misha and Annalisa in Nijmegen. Misha, with your vast amount of scientific knowledge and deep understanding you can guide people in good directions. Annalisa, we did not collaborate closely during my PhD, but you always cared about me and guided me in the world of academia.

I think that the material theory group in Uppsala is really very special. I would like to thank all people in my group, for making my work, the lunches and the *fika* so enjoyable. I'm very grateful to all of you, but some people I would like to thank personally. Iulia and Alex, thanks a lot for the nice juggling hours. I would like to thank my office mates. Samara, I learned a lot from you about Iran and also about myself. Johan, I really enjoyed working with you on our analytic continuation projects. For me it was a lot of fun, sitting together, going through your huge amount of data, structuring and ordering it in order to draw conclusions. Marco, you were also a bit an office mate, but mainly a great collaborator. Your tendency to start an explanation at the very beginning with, "*Do you know what electrons are?*", was really great

when I just started my PhD and knew close to nothing. I really like your intuitive way of thinking and explaining. Your enthusiastic and passionate debates together with Igor were funny and inspiring at the same time. In this list, I finally would like to thank Yaroslav, you are among the kindest people I know. You were always in for discussions and it was very nice to figure out things together with you as we did, for example, with the multiplet structure of the REs.

In Uppsala I, furthermore, would like to thank the DMFT subgroup. It is very inspiring and useful when more people work on related problems with similar methods. The same holds for my direct collaborators, many thanks to all of you. A special thanks to Marco, Erik, Johan Nordström, Johan Schött, Elin, Debora, Manuel, Anna, Somnath, Ronny and Yaroslav.

In Nijmegen I would like to thank the TCM department for hosting me. Lars, Jaap en Alessandro thanks for the help, the discussions and the nice coffee. Guus, Merel, Remko, Lennert, Erik, Koen, Linde and all group members, thanks for the nice time we had.

Doing a PhD in Uppsala, is not only about science, but also about living alone in Sweden for more than four years. This has not always been easy. If it were not for the wonderful job I had, the great group I worked in, and not the least all friends that supported me, I am not sure I would have done it. I would like to thank all friends that visited me, sometimes even in winter or in the dark November month. Dank je wel Margot, Dirk, Linde, Laura, Lizzy, Jan, Heike, Rebekka, Nora, Maartje, Joost, Roos, Wim, Nadia, Maurits, Merel, Jins, Lennert en Erik. Liebe Oma, Silke und Fritz, vielen Dank für euer Besuch. I have many good memories of cups of warm tea, of great walks in stadsskogen and Hågadalens-Nåstens nature, of swimming, of Stockholm, of baking cookies and of hours of peaceful knitting. Linde, thanks a lot for all the phone calls, I could always count on your advise and encouragement. Pappa, mamma and Margot thanks a lot for jumping on the plane when I needed you the most.

I would also like to thank the best roommates ever: Delphine, Kim, Maciej, Wojciech and Sara. I have had so many good evenings, nice barbecues, good backing experiences and cat-chat with you! Sasha and Yaroslav, here is a special thanks to you, it is really great to have some friends that are there when you need them. Everything is good in the end, but sometimes you need friends to remind you.

Jord, thank you very much for all your support, for all the times you came to visit me and for this four and a half years of waiting for me. From now on, we will finally live together again.

Appendices

A. Finding the multiplets in Nd

Here we present a recipe to construct the multiplets in the valence band spectrum, with the XPS spectrum of Nd as example. The $f^3 \rightarrow f^2$ transitions are complicated enough to be able to extend it to more electrons, but simple enough to keep the bookkeeping doable. I have probably learned the recipe in my undergraduate studies, but unfortunately I have also forgotten it... For me learning it again made a lot of things clearer. Therefore I wrote down the example of Nd.

Step 1: Write down all the ways in which one can divide two electrons over 7 orbitals or 14 spin orbitals. This can be done in $\frac{14 \cdot 13}{2} = 91$ ways, which are listed compactly in Tab. A.1 by dividing them into 5 groups. The first group is special, it contains a pair of spin up and spin down in one orbital, which can be $m_l = -3, -2, -1, 0, 1, 2$ or 3. The second group considers two spin up in different orbitals. The first spin up can be in $m_l = -3, -2, -1, 0, 1, 2, 3$ and the second can be in all possible orbitals with m_l bigger than that of the first. The other three groups have the same form, but with one up and one down, with one down and one up, and finally with two spin down electrons.

Step 2: Construct a table denoting how many states we have for each S_z and L_z . The Nd example is given in Tab. A.2.

Step 3: Obtain the possible S, L multiplets from the previous table. Start with the highest possible S_z and L_z , subtract this from the table and continue till all multiplets are specified and only zero's are left in the table. In the Nd example (Tab. A.3 till A.9) we take: $L = 6$ (highest possible $L_z = 6$) for which we only have $S_z = 0 \Rightarrow S = 0$ (Tab. A.3 \rightarrow A.4); $S = 1, L = 5$ (Tab. A.4 \rightarrow A.5); and so forth (Tab. A.5 till A.9). This procedure gave us the following multiplets, which are highlighted in blue in the tables: $^1I_6, ^3H_{4,5,6}, ^1G_4, ^1S_0, ^3F_{2,3,4}, ^1D_2$ and $^3P_{0,1,2}$.

Table A.1. All possible ways to divide two electrons in 7 orbitals denoted with $-3 \leq m_l \leq 3$. The states are grouped, such that the red arrow can be also in the position of the red dots. The total S_z and L_z are given in the subsequent columns. All possibilities for L_z are listed, depending on where the red arrow is. In the last column the number of states in this group is given. The total number of states is $21 + 21 + 21 + 21 + 7 = 91$ as expected.

-3	-2	-1	0	1	2	3	S_z	L_z	#
$\uparrow\downarrow$	0	-6,-4, -2,0,2,4,6	7
\uparrow	\uparrow	1	-5, -4,-3,-2,-1,0 -3, -2, -1,0,1 -1,0,1,2 1,2,3 3,4 5	21
Same for \uparrow \downarrow							0	-5,-4,-3,-2,-1,0, -3,-2,-1,0,1,-1,0,1,2, 1,2,3,3,4,5	21
Same for \downarrow \uparrow							0	-5,-4,-3,-2,-1,0, -3,-2,-1,0,1,-1,0,1,2, 1,2,3,3,4,5	21
Same for \downarrow \downarrow							-1	-5,-4,-3,-2,-1,0, -3,-2,-1,0,1,-1,0,1,2, 1,2,3,3,4,5	21

Table A.2. Number of states with all possible S_z and L_z .

$S_z \setminus L_z$	-6	-5	-4	-3	-2	-1	0	1	2	3	4	5	6
-1	0	1	1	2	2	3	3	3	2	2	1	1	0
0	1	2	3	4	5	6	7	6	5	4	3	2	1
1	0	1	1	2	2	3	3	3	2	2	1	1	0

Table A.3. $S = 0$ and $L = 6$ multiplet 1I_6 .

$S_z \setminus L_z$	-6	-5	-4	-3	-2	-1	0	1	2	3	4	5	6
-1	0	1	1	2	2	3	3	3	2	2	1	1	0
0	1	2	3	4	5	6	7	6	5	4	3	2	1
1	0	1	1	2	2	3	3	3	2	2	1	1	0

Table A.4. $S = 1$ and $L = 5$ multiplet ${}^3H_{4,5,6}$.

$S_z \setminus L_z$	-6	-5	-4	-3	-2	-1	0	1	2	3	4	5	6
-1	0	1	1	2	2	3	3	3	2	2	1	1	0
0	0	1	2	3	4	5	6	5	4	3	2	1	0
1	0	1	1	2	2	3	3	3	2	2	1	1	0

Table A.5. $S = 0$ and $L = 4$ multiplet 1G_4 .

$S_z \setminus L_z$	-6	-5	-4	-3	-2	-1	0	1	2	3	4	5	6
-1	0	0	0	1	1	2	2	2	1	1	0	0	0
0	0	0	1	2	3	4	5	4	3	2	1	0	0
1	0	0	0	1	1	2	2	2	1	1	0	0	0

Table A.6. $S = 1$ and $L = 3$ multiplet ${}^3F_{2,3,4}$.

$S_z \setminus L_z$	-6	-5	-4	-3	-2	-1	0	1	2	3	4	5	6
-1	0	0	0	1	1	2	2	2	1	1	0	0	0
0	0	0	0	1	2	3	4	3	2	1	0	0	0
1	0	0	0	1	1	2	2	2	1	1	0	0	0

Table A.7. $S = 0$ and $L = 2$ multiplet 1D_2 .

$S_z \setminus L_z$	-6	-5	-4	-3	-2	-1	0	1	2	3	4	5	6
-1	0	0	0	0	0	1	1	1	0	0	0	0	0
0	0	0	0	0	1	2	3	2	1	0	0	0	0
1	0	0	0	0	0	1	1	1	0	0	0	0	0

Table A.8. $S = 1$ and $L = 1$ multiplet ${}^3P_{0,1,2}$.

$S_z \setminus L_z$	-6	-5	-4	-3	-2	-1	0	1	2	3	4	5	6
-1	0	0	0	0	0	1	1	1	0	0	0	0	0
0	0	0	0	0	0	1	2	1	0	0	0	0	0
1	0	0	0	0	0	1	1	1	0	0	0	0	0

Table A.9. $S = 0$ and $L = 0$ multiplet 1S_0 .

$S_z \setminus L_z$	-6	-5	-4	-3	-2	-1	0	1	2	3	4	5	6
-1	0	0	0	0	0	0	0	0	0	0	0	0	0
0	0	0	0	0	0	0	1	0	0	0	0	0	0
1	0	0	0	0	0	0	0	0	0	0	0	0	0

References

- [1] <http://elk.sourceforge.net/>.
- [2] O. K. Andersen. Linear methods in band theory. *Phys. Rev. B*, 12:3060–3083, 1975.
- [3] O. K. Andersen and R. V. Kasowski. Electronic states as linear combinations of muffin-tin orbitals. *Phys. Rev. B*, 4:1064–1069, 1971.
- [4] Vladimir I. Anisimov, Jan Zaanen, and Ole K. Andersen. Band theory and Mott insulators: Hubbard U instead of Stoner I . *Phys. Rev. B*, 44:943–954, 1991.
- [5] P. Anthony Cox. Fractional parentage methods for ionisation of open shells of d and f electrons. In *Photoelectron Spectrometry*, volume 24 of *Structure and Bonding*, pages 59–81. Springer Berlin Heidelberg, 1975.
- [6] V. P. Antropov, M. I. Katsnelson, B. N. Harmon, M. van Schilfgaarde, and D. Kusnezov. Spin dynamics in magnets: Equation of motion and finite temperature effects. *Phys. Rev. B*, 54:1019–1035, 1996.
- [7] Neil W. Ashcroft and N. David Mermin. *Solid state physics*. Saunders College, Philadelphia, 1976.
- [8] G. A. Baker. *Essentials of Padé Approximants*. Academic Press, New York, 1975.
- [9] M. Battiato, K. Carva, and P. M. Oppeneer. Superdiffusive spin transport as a mechanism of ultrafast demagnetization. *Phys. Rev. Lett.*, 105:027203, 2010.
- [10] M. Battiato and K. Held. Ultrafast and gigantic spin injection in semiconductors. *Phys. Rev. Lett.*, 116:196601, 2016.
- [11] K. S. D. Beach, R. J. Gooding, and F. Marsiglio. Reliable padé analytical continuation method based on a high-accuracy symbolic computation algorithm. *Phys. Rev. B*, 61:5147–5157, 2000.
- [12] E. Beaurepaire, J.-C. Merle, A. Daunois, and J.-Y. Bigot. Ultrafast spin dynamics in ferromagnetic nickel. *Phys. Rev. Lett.*, 76:4250–4253, 1996.
- [13] Francis Birch. Finite elastic strain of cubic crystals. *Phys. Rev.*, 71:809–824, 1947.
- [14] Torbjörn Björkman. *Magnetic and Structural Properties of f-electron Systems from First Principles Theory*. PhD thesis, Uppsala University, 2009.
- [15] Felix Bloch. Über die quantenmechanik der elektronen in kristallgittern. *Zeitschrift für Physik*, 52(7-8):555–600, 1929.
- [16] M. Born and R. Oppenheimer. Zur quantentheorie der molekeln. *Ann. Phys.*, 389(20):457–484, 1927.
- [17] D. H. Brooks and R. S. MacLeod. Electrical imaging of the heart. *IEEE Signal Processing Magazine*, 14(1):24–42, 1997.
- [18] K. H. J. Buschow. *Handbook of magnetic materials*. Vol. 13. Elsevier, Amsterdam, 2001.

- [19] Robert Carley, Kristian Döbrich, Björn Frietsch, Cornelius Gahl, Martin Teichmann, Olaf Schwarzkopf, Philippe Wernet, and Martin Weinelt. Femtosecond laser excitation drives ferromagnetic gadolinium out of magnetic equilibrium. *Phys. Rev. Lett.*, 109:057401, 2012.
- [20] Stanislav Chadov. Application of many-body perturbation theory to the description of correlated metals, 2007.
- [21] C Cheng, R J Needs, and V Heine. Inter-layer interactions and the origin of SiC polytypes. *Journal of Physics C: Solid State Physics*, 21(6):1049, 1988.
- [22] P A Cox, J K Lang, and Y Baer. Study of the 4f and valence band density of states in rare-earth metals. I. theory of the 4f states. *Journal of Physics F: Metal Physics*, 11(1):113, 1981.
- [23] F. Dalla Longa, J. T. Kohlhepp, W. J. M. de Jonge, and B. Koopmans. Influence of photon angular momentum on ultrafast demagnetization in nickel. *Phys. Rev. B*, 75:224431, 2007.
- [24] P. H. Dederichs, S. Blügel, R. Zeller, and H. Akai. Ground states of constrained systems: Application to cerium impurities. *Phys. Rev. Lett.*, 53:2512–2515, 1984.
- [25] Anna Delin, Lars Fast, Börje Johansson, Olle Eriksson, and J. M. Wills. Cohesive properties of the lanthanides: Effect of generalized gradient corrections and crystal structure. *Phys. Rev. B*, 58:4345–4351, 1998.
- [26] P J H Denteneer and W van Haeringen. Stacking-fault energies in semiconductors from first-principles calculations. *Journal of Physics C: Solid State Physics*, 20(32):L883, 1987.
- [27] Igor Di Marco. *Correlation Effects in the Electronic Structure of Transition Metals and Their Compounds*. PhD thesis, Radboud University Nijmegen, Ipskamp Drukkers, Enschede, The Netherlands, 2009.
- [28] F Drymiotis, J Singleton, N Harrison, J C Lashley, A Bangura, C H Mielke, L Balicas, Z Fisk, A Miglioni, and J L Smith. Suppression of the γ - α structural phase transition in $\text{Ce}_{0.8}\text{La}_{0.1}\text{Th}_{0.1}$ by large magnetic fields. *Journal of Physics: Condensed Matter*, 17(7):L77, 2005.
- [29] H Ebert. Magneto-optical effects in transition metal systems. *Reports on Progress in Physics*, 59(12):1665, 1996.
- [30] Olle Eriksson, M. S. S. Brooks, and Börje Johansson. Orbital polarization in narrow-band systems: Application to volume collapses in light lanthanides. *Phys. Rev. B*, 41:7311–7314, 1990.
- [31] Michael Faraday. Experimental researches in electricity. nineteenth series. *Philosophical Transactions of the Royal Society of London*, 136:1–20, 1846.
- [32] Raymond Frésard and Gabriel Kotliar. Interplay of mott transition and ferromagnetism in the orbitally degenerate hubbard model. *Phys. Rev. B*, 56:12909–12915, 1997.
- [33] Antoine Georges. Strongly correlated electron materials: Dynamical mean-field theory and electronic structure. *AIP Conference Proceedings*, 715(1):3–74, 2004.
- [34] Khaldoon Ghanem. Stochastic Mode Sampling (SMS) – An Efficient Approach to the Analytic Continuation Problem. Ms, RWTH Aachen, 2013. RWTH Aachen, Masterarbeit, 2013.
- [35] Roberta Grech, Tracey Cassar, Joseph Muscat, Kenneth P Camilleri, Simon G

- Fabri, Michalis Zervakis, Petros Xanthopoulos, Vangelis Sakkalis, and Bart Vanrumste. Review on solving the inverse problem in EEG source analysis. *Journal of NeuroEngineering and Rehabilitation*, 5:25–25, 2008.
- [36] W. A. Grosshans and W. B. Holzapfel. Atomic volumes of rare-earth metals under pressures to 40 GPa and above. *Phys. Rev. B*, 45:5171–5178, 1992.
 - [37] G. Grosso and G.P. Parravicini. *Solid State Physics*. Academic Press, 2000.
 - [38] K.A. Gschneidner. Physical properties of the rare earth metals. *Bulletin of Alloy Phase Diagrams*, 11(3):216–224, 1990.
 - [39] Karl A. Gschneidner and LeRoy Eyring. *Handbook on the physics and chemistry of rare earths. Vol. 1, Metals*. Amsterdam, 1978.
 - [40] Karl A. jr. Gschneidner and LeRoy Eyring. *Handbook on the physics and chemistry of rare earths. Vol. 10, High energy spectroscopy*. Amsterdam, 1987.
 - [41] O. Gunnarsson, J. W. Allen, O. Jepsen, T. Fujiwara, O. K. Andersen, C. G. Olsen, M. B. Maple, J.-S. Kang, L. Z. Liu, J.-H. Park, R. O. Anderson, W. P. Ellis, R. Liu, J. T. Markert, Y. Dalichaouch, Z.-X. Shen, P. A. P. Lindberg, B. O. Wells, D. S. Dessau, A. Borg, I. Lindau, and W. E. Spicer. Polarized resonance photoemission for Nd₂CuO₄. *Phys. Rev. B*, 41:4811–4814, 1990.
 - [42] O. Gunnarsson, O. K. Andersen, O. Jepsen, and J. Zaanen. Density-functional calculation of the parameters in the Anderson model: Application to Mn in CdTe. *Phys. Rev. B*, 39:1708–1722, 1989.
 - [43] P. C. Hansen. The L-curve and its use in the numerical treatment of inverse problems. In *Computational Inverse Problems in Electrocardiology*, ed. P. Johnston, *Advances in Computational Bioengineering*, pages 119–142. WIT Press, 2000.
 - [44] K. Held. Electronic structure calculations using dynamical mean field theory. *Advances in Physics*, 56(6):829–926, 2007.
 - [45] P. Hohenberg and W. Kohn. Inhomogeneous electron gas. *Phys. Rev.*, 136:B864–B871, 1964.
 - [46] J. Hubbard. Electron correlations in narrow energy bands. *Proceedings of the Royal Society of London A: Mathematical, Physical and Engineering Sciences*, 276(1365):238–257, 1963.
 - [47] J. Hubbard. Electron correlations in narrow energy bands. II. the degenerate band case. *Proceedings of the Royal Society of London A: Mathematical, Physical and Engineering Sciences*, 277(1369):237–259, 1964.
 - [48] J. Hubbard. Electron correlations in narrow energy bands. III. an improved solution. *Proceedings of the Royal Society of London A: Mathematical, Physical and Engineering Sciences*, 281(1386):401–419, 1964.
 - [49] Christian Illg, Michael Haag, and Manfred Fähnle. Ultrafast demagnetization after laser irradiation in transition metals: *Ab initio* calculations of the spin-flip electron-phonon scattering with reduced exchange splitting. *Phys. Rev. B*, 88:214404, 2013.
 - [50] Mark Jarrell and J.E. Gubernatis. Bayesian inference and the analytic continuation of imaginary-time quantum Monte Carlo data. *Physics Reports*, 269(3):133 – 195, 1996.
 - [51] Jens Jensen and Allan R. Mackintosh. *Rare earth magnetism*. Clarendon Press, Oxford, 1991.
 - [52] Börje Johansson and Anders Rosengren. Generalized phase diagram for the

- rare-earth elements: Calculations and correlations of bulk properties. *Phys. Rev. B*, 11:2836–2857, 1975.
- [53] Neil Erich Koch. Crystal structures and electrical resistivities of new YRu₄Sn₆-type rare-earth based compounds. Master’s thesis, University of Johannesburg, South Africa, 2008.
- [54] W. Kohn and L. J. Sham. Self-consistent equations including exchange and correlation effects. *Phys. Rev.*, 140:A1133–A1138, 1965.
- [55] B. Koopmans, G. Malinowski, F. Dalla Longa, D. Steiauf, M. Fahnle, T. Roth, M. Cinchetti, and M. Aeschlimann. Explaining the paradoxical diversity of ultrafast laser-induced demagnetization. *Nat Mater*, 9(3):259–265, 2010.
- [56] Chan La-O-Vorakiat, Emrah Turgut, Carson A. Teale, Henry C. Kapteyn, Margaret M. Murnane, Stefan Mathias, Martin Aeschlimann, Claus M. Schneider, Justin M. Shaw, Hans T. Nembach, and T. J. Silva. Ultrafast demagnetization measurements using extreme ultraviolet light: Comparison of electronic and magnetic contributions. *Phys. Rev. X*, 2:011005, 2012.
- [57] J. K. Lang, Y. Baer, and P. A. Cox. Study of the 4f and valence band density of states in rare-earth metals. II. experiment and results. *Journal of Physics F: Metal Physics*, 11(1):121, 1981.
- [58] C. L. Lawson and R. J. Hanson. *Solving Least Squares Problems*. Society for Industrial and Applied Mathematics Philadelphia, Philadelphia, 1995.
- [59] S. Lebègue, A. Svane, M. I. Katsnelson, A. I. Lichtenstein, and O. Eriksson. Multiplet effects in the electronic structure of heavy rare-earth metals. *Journal of Physics: Condensed Matter*, 18(27):6329, 2006.
- [60] S. Lebègue, A. Svane, M. I. Katsnelson, A. I. Lichtenstein, and O. Eriksson. Multiplet effects in the electronic structure of light rare-earth metals. *Phys. Rev. B*, 74:045114, 2006.
- [61] Kurt Lejaeghere, Gustav Bihlmayer, Torbjörn Björkman, Peter Blaha, Stefan Blügel, Volker Blum, Damien Caliste, Ivano E. Castelli, Stewart J. Clark, Andrea Dal Corso, Stefano de Gironcoli, Thierry Deutsch, John Kay Dewhurst, Igor Di Marco, Claudia Draxl, Marcin Dułak, Olle Eriksson, José A. Flores-Livas, Kevin F. Garrity, Luigi Genovese, Paolo Giannozzi, Matteo Giantomassi, Stefan Goedecker, Xavier Gonze, Oscar Grånäs, E. K. U. Gross, Andris Gulans, François Gygi, D. R. Hamann, Phil J. Hasnip, N. A. W. Holzwarth, Diana Iuşan, Dominik B. Jochym, François Jollet, Daniel Jones, Georg Kresse, Klaus Koepnik, Emine Küçükbenli, Yaroslav O. Kvashnin, Inka L. M. Locht, Sven Lubeck, Martijn Marsman, Nicola Marzari, Ulrike Nitzsche, Lars Nordström, Taisuke Ozaki, Lorenzo Paulatto, Chris J. Pickard, Ward Poelmans, Matt I. J. Probert, Keith Refson, Manuel Richter, Gian-Marco Rignanese, Santanu Saha, Matthias Scheffler, Martin Schlipf, Karlheinz Schwarz, Sangeeta Sharma, Francesca Tavazza, Patrik Thunström, Alexandre Tkatchenko, Marc Torrent, David Vanderbilt, Michiel J. van Setten, Veronique Van Speybroeck, John M. Wills, Jonathan R. Yates, Guo-Xu Zhang, and Stefaan Cottenier. Reproducibility in density functional theory calculations of solids. *Science*, 351(6280), 2016.
- [62] I. L. M. Locht. Cohesive and spectroscopic properties of the lanthanides within the Hubbard I approximation. Available at <http://uu.diva-portal.org/smash/get/diva2:872619/FULLTEXT02.pdf>,

- 2015.
- [63] G. Malinowski, F. Dalla Longa, J. H. H. Rietjens, P. V. Paluskar, R. Huijink, H. J. M. Swagten, and B. Koopmans. Control of speed and efficiency of ultrafast demagnetization by direct transfer of spin angular momentum. *Nat Phys*, 4(11):855–858, 2008.
 - [64] Richard M. Martin. *Electronic structure : basic theory and practical methods*. Cambridge University Press, Cambridge, New York, 2004.
 - [65] Stefan Mathias, Chan La o vorakiat, Justin M. Shaw, Emrah Turgut, Patrik Grychtol, Roman Adam, Dennis Rudolf, Hans T. Nembach, Thomas J. Silva, Martin Aeschlimann, Claus M. Schneider, Henry C. Kapteyn, and Margaret M. Murnane. Ultrafast element-specific magnetization dynamics of complex magnetic materials on a table-top. *Journal of Electron Spectroscopy and Related Phenomena*, 189:164 – 170, 2013.
 - [66] A. K. McMahan, Richard M. Martin, and S. Satpathy. Calculated effective hamiltonian for La_2CuO_4 and solution in the impurity Anderson approximation. *Phys. Rev. B*, 38:6650–6666, 1988.
 - [67] A. Melnikov, H. Prima-Garcia, M. Lisowski, T. Gießel, R. Weber, R. Schmidt, C. Gahl, N. M. Bulgakova, U. Bovensiepen, and M. Weinelt. Nonequilibrium magnetization dynamics of gadolinium studied by magnetic linear dichroism in time-resolved 4f core-level photoemission. *Phys. Rev. Lett.*, 100:107202, 2008.
 - [68] Alexey Melnikov, Ilya Razdolski, Tim O. Wehling, Evangelos Th. Papaioannou, Vladimir Roddatis, Paul Fumagalli, Oleg Aktsipetrov, Alexander I. Lichtenstein, and Uwe Bovensiepen. Ultrafast transport of laser-excited spin-polarized carriers in $\text{Au/Fe/MgO}(001)$. *Phys. Rev. Lett.*, 107:076601, 2011.
 - [69] Walter Metzner and Dieter Vollhardt. Correlated lattice fermions in $d = \infty$ dimensions. *Phys. Rev. Lett.*, 62:324–327, 1989.
 - [70] A. S. Mishchenko, N. V. Prokof'ev, A. Sakamoto, and B. V. Svistunov. Diagrammatic quantum Monte Carlo study of the Fröhlich polaron. *Phys. Rev. B*, 62:6317–6336, 2000.
 - [71] Sparsh Mittal and Jeffrey S. Vetter. A survey of methods for analyzing and improving GPU energy efficiency. *ACM Comput. Surv.*, 47(2):19:1–19:23, 2014.
 - [72] S.K. Mohanta, S.N. Mishra, S.K. Srivastava, and M. Rots. First-principles calculation of the electric field gradient and magnetic hyperfine field in rare-earth metals (Gd to Lu) and dilute alloys with Cd. *Solid State Communications*, 150(37-38):1789 – 1793, 2010.
 - [73] K.T. Moore, L. Belhadi, F. Decremps, D.L. Farber, J.A. Bradley, F. Occelli, M. Gauthier, A. Polian, and C.M. Aracne-Ruddle. Watching a metal collapse: Examining cerium $\gamma \leftrightarrow \alpha$ transformation using x-ray diffraction of compressed single and polycrystals. *Acta Materialia*, 59(15):6007 – 6016, 2011.
 - [74] Johan Nordström. GPU parallelization of the Mishchenko method for solving Fredholm equations of the first kind, 2015.
 - [75] Johan Nordström, Johan Schött, Inka L.M. Loch, and Igor Di Marco. <https://github.com/ElsevierSoftwareX/SOFTX-D-16-00025>, 2016.
 - [76] Johan Nordström, Johan Schött, Inka L.M. Loch, and Igor Di Marco. A GPU

- code for analytic continuation through a sampling method. *SoftwareX*, pages –, 2016.
- [77] M. R. Norman and A. J. Freeman. Model supercell local-density calculations of the 3d excitation spectra in NiO. *Phys. Rev. B*, 33:8896–8898, 1986.
 - [78] L. Oroszlány, A. Deák, E. Simon, S. Khmelevskiy, and L. Szunyogh. Magnetism of gadolinium: A first-principles perspective. *Phys. Rev. Lett.*, 115:096402, 2015.
 - [79] Žiga Osolin and Rok Žitko. Padé approximant approach for obtaining finite-temperature spectral functions of quantum impurity models using the numerical renormalization group technique. *Phys. Rev. B*, 87:245135, 2013.
 - [80] A. Östlin, L. Chioncel, and L. Vitos. One-particle spectral function and analytic continuation for many-body implementation in the exact muffin-tin orbitals method. *Phys. Rev. B*, 86:235107, 2012.
 - [81] J. P. Perdew and Alex Zunger. Self-interaction correction to density-functional approximations for many-electron systems. *Phys. Rev. B*, 23:5048–5079, 1981.
 - [82] L. V. Pourovskii, B. Amadon, S. Biermann, and A. Georges. Self-consistency over the charge density in dynamical mean-field theory: A linear muffin-tin implementation and some physical implications. *Phys. Rev. B*, 76:235101, 2007.
 - [83] Helmut Rathgen and Mikhail I Katsnelson. Symmetry assumptions, Kramers-Kronig transformation and analytical continuation in *Ab Initio* calculations of optical conductivities. *Physica Scripta*, 2004(T109):170, 2004.
 - [84] G. Rohringer. New routes towards a theoretical treatment of nonlocal electronic correlations. *Available at* http://www.ifp.tuwien.ac.at/fileadmin/Arbeitsgruppen/quantum_manybody_physics/docs/thesis/rohringerPhD.pdf, 2014.
 - [85] A.N. Rubtsov, M.I. Katsnelson, and A.I. Lichtenstein. Dual boson approach to collective excitations in correlated fermionic systems. *Annals of Physics*, 327(5):1320 – 1335, 2012.
 - [86] Dennis Rudolf, Chan La-O-Vorakiat, Marco Battiato, Roman Adam, Justin M. Shaw, Emrah Turgut, Pablo Maldonado, Stefan Mathias, Patrik Grychtol, Hans T. Nembach, Thomas J. Silva, Martin Aeschlimann, Henry C. Kapteyn, Margaret M. Murnane, Claus M. Schneider, and Peter M. Oppeneer. Ultrafast magnetization enhancement in metallic multilayers driven by superdiffusive spin current. *Nat Commun*, 3:1037, 2012.
 - [87] L. M. Sandratskii. Exchange splitting of surface and bulk electronic states in excited magnetic states of Gd: First-principles study. *Phys. Rev. B*, 90:184406, 2014.
 - [88] Hans L. Skriver. Crystal structure from one-electron theory. *Phys. Rev. B*, 31:1909–1923, 1985.
 - [89] Per Söderlind, P. E. A. Turchi, A. Landa, and V. Lordi. Ground-state properties of rare-earth metals: an evaluation of density-functional theory. *Journal of Physics: Condensed Matter*, 26(41):416001, 2014.
 - [90] Vidar Stiernström, Joakim Johansson, and Viktor Edward. Thanks to these students that performed an MPI parallelization of Mishchenko’s stochastic sampling method, 2014.
 - [91] P. Strange, A. Svane, W. M. Temmerman, Z. Szotek, and H. Winter.

- Understanding the valency of rare earths from first-principles theory. *Nature*, 399:756–758, 1999.
- [92] Andrej Nikolaevic Tichonov and Vasilij Ja. Arsenin. *Solutions of ill-posed problems*. Washington, D.C., 1977.
- [93] Emrah Turgut, Chan La-o vorakiat, Justin M. Shaw, Patrik Grychtol, Hans T. Nembach, Dennis Rudolf, Roman Adam, Martin Aeschlimann, Claus M. Schneider, Thomas J. Silva, Margaret M. Murnane, Henry C. Kapteyn, and Stefan Mathias. Controlling the competition between optically induced ultrafast spin-flip scattering and spin transport in magnetic multilayers. *Phys. Rev. Lett.*, 110:197201, 2013.
- [94] S. Valencia, A. Kleibert, A. Gaupp, J. Rusz, D. Legut, J. Bansmann, W. Gudat, and P. M. Oppeneer. Quadratic x-ray magneto-optical effect upon reflection in a near-normal-incidence configuration at the m edges of 3d-transition metals. *Phys. Rev. Lett.*, 104:187401, 2010.
- [95] J. Wieczorek, A. Eschenlohr, B. Weidtmann, M. Rösner, N. Bergear, A. Tarasevitch, T. O. Wehling, and U. Bovensiepen. Separation of ultrafast spin currents and spin-flip scattering in Co/Cu(001) driven by femtosecond laser excitation employing the complex magneto-optical Kerr effect. *Phys. Rev. B*, 92:174410, 2015.
- [96] J.M. Wills, O. Eriksson, M. Alouani, and D.L. Price. Full-potential LMTO total energy and force calculations. In *Electronic Structure and Physical Properties of Solids*, volume 535 of *Lecture Notes in Physics*, pages 148–167. Springer Berlin Heidelberg, 2000.
- [97] John M. Wills, Mebarek Alouani, Per Andersson, Anna Delin, Olle Eriksson, and Oleksiy Grechnev. The full-potential electronic structure problem and RSPt. In *Full-Potential Electronic Structure Method*, volume 167 of *Springer Series in Solid-State Sciences*, pages 47–73. Springer Berlin Heidelberg, 2010.
- [98] Pochi Yeh. Optics of anisotropic layered media: A new 4×4 matrix algebra. *Surface Science*, 96(1):41 – 53, 1980.
- [99] D.A. Young. *Phase diagrams of the elements*. 1975.
- [100] E. G. Zukas, R. A. Pereyra, and J. O. Willis. The γ to α phase transformation in cerium. *Metallurgical Transactions A*, 18(1):35–42, 1987.

Acta Universitatis Upsaliensis

*Digital Comprehensive Summaries of Uppsala Dissertations
from the Faculty of Science and Technology 1461*

Editor: The Dean of the Faculty of Science and Technology

A doctoral dissertation from the Faculty of Science and Technology, Uppsala University, is usually a summary of a number of papers. A few copies of the complete dissertation are kept at major Swedish research libraries, while the summary alone is distributed internationally through the series Digital Comprehensive Summaries of Uppsala Dissertations from the Faculty of Science and Technology. (Prior to January, 2005, the series was published under the title "Comprehensive Summaries of Uppsala Dissertations from the Faculty of Science and Technology".)



ACTA
UNIVERSITATIS
UPSALIENSIS
UPPSALA
2017

Distribution: publications.uu.se
urn:nbn:se:uu:diva-308699